UNIVERSITY OF OKLAHOMA

GRADUATE COLLEGE

# HAILSTONE TRAJECTORY AND SURFACE HAILFALL ANALYSIS IN THE 29 – 30 MAY 2012 KINGFISHER, OKLAHOMA SUPERCELL

A THESIS

SUBMITTED TO THE GRADUATE FACULTY

in partial fulfillment of the requirements for the

Degree of

MASTER OF SCIENCE IN METEOROLOGY

By

LAUREN ELIZABETH POUNDS
Norman, Oklahoma
2022

HAILSTONE TRAJECTORY AND SURFACE HAILFALL ANALYSIS IN THE 29 – 30 MAY 2012 KINGFISHER, OK SUPERCELL

A THESIS APPROVED FOR THE

SCHOOL OF METEOROLOGY

BY THE COMMITTEE CONSISTING OF

Dr. Michael Biggerstaff, Chair

Dr. Conrad Ziegler

Dr. Cameron Homeyer

## Acknowledgments

First and foremost, to my family who recognized my dream to become a meteorologist before I did, I am thankful for you fostering my passion. If it wasn't for them telling me to major in meteorology, I wouldn't have. If they didn't remind me that OU was a dream I had to pursue, I wouldn't be here today.

To the friends who have been part of my graduate school experience alongside me, thank you for your support. Every single time I listen to you talk to about your research, I am inspired to become a better scientist. I am thankful for the support of my roommate and classmate, Michael Hosek, who endured this journey with me and supported me in every way throughout. I am thankful for all I learned from Melanie Schroers from the hundreds of questions I asked her (mostly about python, of course). Only a few words cannot express my gratitude to Anna Wanless and Francesca Lappin for the constant love and laughs, but they have been the greatest friends I could ever have. I would also like to thank Max Ungar for his continuous encouragement and endless support in every way. All of my classmates and friends who have encouraged me and supported me during these past three years, I can never thank you enough.

I want to thank those who provided the guidance and mentorship to make this thesis what it is, especially my advisor, Conrad Ziegler, as well as my committee members, Cameron Homeyer and Michael Biggerstaff. All of those on the PREEVENTS grant, I always look forward to our group discussions and am thankful for all I have learned from each one of you. Thank you to Becky Adams-Selin for the additional insight and time spent guiding my work. I am a better scientist because of every one of you. To that, I will be forever indebted.

This research was funded by NSF grant AGS-1855100, and computer and infrastructure support provided by the National Severe Storms Laboratory

## Table of Contents

# List of Tables

## List of Figures

## Abstract

During the Deep Convective Clouds and Chemistry Experiment (DC3), a wealth of data was collected on a hail-producing tornadic supercell near Kingfisher, OK on 29-30 May 2012. Three mobile radars collected radial velocity, reflectivity, and polarimetric data over a ~70-minute period during the storm's mature phase. Additionally, far-environmental and in-storm soundings were taken following the storm's track while hail samples were collected in the town of Kingfisher, OK by the Insurance Institute for Business and Home Safety (IBHS). The 4-D storm fields of airflow and reflectivity from multi-Doppler radar analyses are combined with 4-D Diabatic Lagrangian Analysis (DLA) retrievals of temperature and water substance and WRF-HAILCAST physics to compute densely spaced Lagrangian hail growth trajectories for the present study. Hail embryos are initialized in the hail growth module every three minutes of the radar analysis period (2251-0000 UTC) to produce over 2.7 million hail trajectories. Using a new, unique dataset we validate previous hail growth trajectory theories and introduce new hypotheses.

Hailstone positions within the storm and at the surface are analyzed for hailstones of varying sizes. It is found that severe hailstones spend a majority of their growth phase within the downshear stagnation zone where horizontal winds are have minimal impact on the hailstones. Simulated severe hail is favored over non-severe hail by significantly longer residence times in 30-50 m/s updrafts and supercooled cloud water contents exceeding 5 g/kg. As the storm strengthens, a new trajectory pathway from embryos sourced within the backsheard anvil emerges, which leads to an increase in overall hail production. Simulated hail swaths provide spatial and temporal understanding of hail diameters and concentrations at the surface. The largest hail falls to surface preferentially along the southern (storm-inflow) flank of the hail swath, though size-sorting effects differ along the hail swath.

In an effort to improve the hail growth physics, sensitivity tests are conducted on the heat transfer coefficient while hailstones are allowed to be oblate, the ice collection efficiency, and the shedding threshold. The ice collection efficiency showed no sensitives while the shedding threshold showed the greatest sensitivity for the smallest hailstones. Oblate hailstones with increased heat transfer showed the greatest sensitivity. Spherical and oblate hailstones are compared to observations and we conclude the oblate hailstones are more physically representative of what was observed and would occur in nature.

# Chapter 1: Background

On 29 – 30 May 2012, during the Deep Convective Clouds and Chemistry Experiment (DC3), a comprehensive research observational dataset was obtained on a supercell near the town of Kingfisher, OK. The kinematics, thermodynamics, and microphysics of the hailstorm and the detailed growth physics following individual hailstone trajectories within the Kingfisher supercell are analyzed in this study. The goal is to gain understanding of the environmental characteristics and storm dynamics that support large hail formation. The physical growth processes and positions of individual hailstones within the storm during growth as well as their individual and collective surface fallout positions are analyzed. Prior modeling, observational, and laboratory studies have greatly contributed to our knowledge of hail growth, providing important background to develop and test new hail growth hypotheses that are evaluated in the present thesis.

## 1.1. Historical overview of prior hail growth trajectory studies

During the 1970s and 1980s, many hail growth studies emerged from the National Hail Research Experiment (NHRE), a field campaign that took place between 1972 and 1976 with goals to further understand the cloud microphysics that led to damaging hail. Additional studies resulted from the Cooperative Convective Precipitation Experiment (CCOPE), which took place in 1981 with the goals of furthering understanding microphysical processes and air motions that influence precipitation through observations. Annual Spring observations of severe storms in Oklahoma led by the National Severe Storms Laboratory (NSSL) during the 1970s and 1980s provided the opportunity to study US Southern Plains supercell hailstorms, whose environments were distinctly different than the High Plains environments typifying hailstorms in the High Plains of northern CO (NHRE) and eastern MT (CCOPE). Several of the NHRE studies focused on hail suppression as their goal, ultimately without success. The foundational work leading to present-day understanding of hail growth was based on analysis of storms sampled during the NHRE, CCOPE, and NSSL warm season experiments (e.g., Heymsfield 1978; Paluch 1978; Heymsfield et al. 1980; Heymsfield 1982; Heymsfield and Musil 1982; Nelson 1983; Ziegler et al. 1983; Nelson and Knight 1987a,b; Rasmussen and Heymsfield 1987; Miller et al. 1988, 1990; Conway and Zrnic 1993). The earliest hail trajectory studies used ideal flow fields (Browning 1963; Musil 1970; English 1973) to simulate airflow and hailstone trajectories. These studies were 1-D and used a non-steady state model with time dependencies to calculate hail trajectories. From these studies, the first ideas of how hailstones behave as they interact with the in-storm dynamics were introduced. In the following decade, numerous multi-Doppler studies were published furthering our understanding of hail growth by employing radar-derived 3-D airflow to transport and provide parameterized cloud water and cloud ice fields to grow numerically simulated hail (Paluch 1978; Heymsfield et al. 1980; Foote 1984; Heymsfield 1983b; Nelson 1983; Miller and Fankhauser 1983; Ziegler et al. 1983; Knight and Knupp 1983; Nelson and Knight 1987a,b; Rasmussen and Heymsfield 1987; Miller et al. 1988, 1990; Conway and Zrnic 1993). In more recent years, model simulations have been used to provide internal storm characteristics and calculate simulated hail trajectories that have furthered understanding of hail growth (Adams-Selin and Ziegler 2016; Dennis and Kumjian 2017; Kumjian and Lombardo 2020).

The thermodynamics and kinematics of particular environments that support supercells also support large hail formation. An analysis of 568 giant hail (> 10 cm) reports by Blair et al. (2011) determined that 99% of those events associated with supercells, making the ability to distinguish the environmental variables and storm characteristics that control hail growth from slightly differing supercell-supporting environments difficult and an ongoing area of research. From the early idealized flow studies to radar analyses to detailed model-simulated storms, hail trajectory analyses have identified the in-storm components that contribute to hail growth including characteristics of the updraft, cloud water contents, cloud precipitation particles, and airflow patterns. All these factors have an impact on how long a hailstone will remain aloft in the primary growth zone – referred to as "residence time", a primary control in final hailstone diameter.

**1.2. Storm characteristics that favor hail growth**

Characteristics of the updraft were identified in early studies to be critical for hail production, particularly the balance between the vertical velocity of the updraft and the terminal velocity of the hailstones (Browning 1963, Morgan 1972; Heymsfield 1983b; Nelson 1983; Miller and Fankhauser 1983; Ziegler et al. 1983; Foote 1984; Musil et al. 1986; Miller et al. 1990; Conway and Zrnic 1993; Kennedy and Detwiler 2003; Knight and Knight 2005; Grant and van den Heever 2014). An updraft-fallspeed balance is difficult to maintain within the main updraft core, where vertical velocities often exceed the hailstone's terminal velocity, resulting in hailstones often processing through the edges of the updraft core where large hail fallspeeds may balance or exceed updraft speeds (List et al. 1968; Orville and Kopp 1977; Nelson 1983). Vertical velocities much greater than the hail terminal velocity tend to loft the particle away from the prime growth region resulting in minimal growth (Browning and Foote 1976; Nelson 1983; Foote 1984; Musil et al. 1986; Rasmussen and Heymsfield 1987). Strong updrafts inhibit hail growth as they do not have a sufficient region of vertical velocities where the net vertical velocity balance can be approximated (Ziegler et al. 1983). Since a larger area of moderate (20 – 40 m $s^{-1}$) updraft strength is preferred for hail growth, updraft width is an important characteristic of storms with significant hail growth potential. A wider (broader) updraft is beneficial for hail growth (Foote 1984; Nelson 1983; Ziegler et al. 1983; Nelson and Knight 1987a,b; Picca and Ryzhkov 2012; Kumjian et al. 2021).

Hailstones can spend more residence time in their prime growth layer if they move and grow within a broader storm updraft region that approximates a net vertical velocity balance (Nelson 1983), a preferred growth mode for hailstones to take advantage of favorable conditions. Ideally, the updrafts most supportive of hail growth would have a broad region of moderate vertical velocities. That leads to the question: which environments optimally support such an updraft? Dennis and Kumjian (2017) presented evidence that the environmental hodograph can control all the updraft characteristics mentioned above, such as strength, width, and size. Greater deep-layer shear elongates the updraft in the downshear direction, which leads to greater hail production as the zonal shear increases. Reports of larger hail are often associated with hodographs with greater zonal shear (Johnson and Sugden 2014; Taszarek et al. 2017). Inversely, an elongated updraft in the north-south direction associates with less hail production as the meridional shear increases (Dennis and Kumjian 2017). In addition to increased volume for updraft-fallspeed balance in the prime growth zone, wider updrafts are associated with greater liquid water content (Peters et al. 2019, 2020; Kumjian et al. 2021) likely due to reduced lateral entrainment mixing and increased numbers of surface-based updraft air trajectories.

The storm's prime growth layer where hailstones spend most of their residence time has implications for the availability of supercooled cloud water. For the greatest chance of growth, hailstones should reside in the upper-middle levels where supercooled cloud water is most abundant. Sufficiently cold ambient in-cloud temperatures where hailstones are present are importantly phased with supercooled cloud water content. The ideal temperature for hail growth has been identified between -10° C and -25° C (Knight et al. 1975; Knight et al. 1981; Foote 1984; Nelson 1983; Ziegler et al. 1983), where supercooled water is often most abundant, although near-adiabatic supercooled cloud water content can exist in strong storms (particularly supercells) anywhere between 0° C and -40° C. Above approximately -40° C, heterogeneous supercooled cloud droplet nucleation to cloud ice dominates. Collection of cloud ice is an inefficient hail growth mechanism and is also unlikely to occur during dry growth.

### 1.3. Embryo sources relative to hail growth trajectories

Likelihood of significant hail production is impacted by characteristics of available embryos, including embryo number concentration, size, and location. Sufficient amounts of supercooled cloud water can vary depending on the amount and location of embryos present. A large number of embryos can lead to competition for supercooled cloud water via accretion and freezing (Browning and Foote 1967; Foote 1984). Alternatively, additional embryos in the updraft region could locally stimulate hail growth (Paluch 1978). Embryos in the 5 mm – 7 mm range are more likely to result in hailstones due to their ubiquity via relatively large concentrations (Heymsfield 1982; Heymsfield and Musil 1982; Foote 1984). Hail growth sensitivity tests conducted by Adams-Selin and Ziegler (2016) reveal that larger embryos (5 mm, 7.5 mm, and 10 mm) in a strong updraft are preferred as they are able to take advantage of the supercooled water within the storm, while the smaller embryos (0.9 mm) are lofted above the region of supercooled water. Results showed that embryos (of varying sizes) can start from many differing positions within the storm and still result in hail growth (Rosinski et al. 1979; Foote 1984; Nelson 1983). Foote (1984) also noted that while hail can result from embryos in virtually any initial position, the region where embryos result in large hail is limited. Hail will likely not form if embryos are only grown within the updraft region (Heymsfield 1982). There are three main source regions (for larger embryos), as described by Dennis and Kumjian (2017): 1) the right or southern flank of the updraft (also known as the "embryo corridor") in low levels, 2) a narrow ribbon along the rear flank of the updraft, and 3) within the updraft below 8 km. Since an increase in zonal shear leads to a broader updraft, it also broadens the volume of the embryo source region. Inversely, an increase in meridional shear decreases the embryo source region (Dennis and Kumjian 2017).

Embryos available in preferred source regions are needed to initiate a hail trajectory that will result in significant particle growth. Many studies have emphasized the importance of internal storm airflow patterns for hail growth (Browning and Foote 1976; Nelson 1983; Ziegler et al. 1983; Foote 1984; Nelson 1987), likely equally as important as embryo source regions (Foote 1984). Nelson (1983) suggested that a storm's kinematics have a greater control on severe hail development than its microphysical parameters. Horizontal winds should be oriented to favor horizontal embryo transport across the major axis of the broad moderate updraft area (Nelson 1983). Foote (1984) suggested that the most important horizontal winds for hail growth are in the middle levels (specifically 6 km – 7 km). Weak horizontal flow within the main updraft edge, if phased with hailstone that have already developed increased mass and fallspeed, can subsequently increase the residence time by extending the balance between the vertical and terminal velocities (Rasmussen and Heymsfield 1987b; Heymsfield 1983b; Foote 1984) and thus produce larger hail.

The aforementioned environmental characteristics all play roles in modulating how, when, and where hailstones grow, all being main questions addressed in the present thesis. Despite a wealth of knowledge about the impacts of the outlined environmental characteristics on hail growth, there remains a gap in knowledge of how these environmental characteristics dictate the trajectory pathways that hailstones will take. Early hail trajectory studies concluded that there are numerous trajectories hailstones can take to grow to severe limits. Common embryo and hailstone trajectory pathways have been noted in the literature, with small distinctions between pathways. The classical Browning and Foote (1976) conceptual model, elements of which are still rather widely accepted, was among the first to identify three main embryo and hail trajectory pathways or particle growth scenarios ("stages"). The analysis by Browning and Foote (1976) describes these particle trajectory pathways as the following: 1) embryo trajectories that enter the main updraft, experience minor growth, are lofted out of the updraft into the downshear anvil and thus do not subsequently grow into hailstones; 2) a subset of favored embryo trajectories from stage (1) that recycle back to the upshear edge of the updraft and grow moderately before entering the “embryo curtain” on the upshear updraft flank; and 3) a continuation of particle trajectories described in stage (2) where the particle subsequently falls to the bottom of the embryo curtain, recycles back into the upshear updraft flank where they can grow into hailstones due to encountering significant supercooled cloud water contents. Unanswered questions remain about trajectory pathways, particularly concerning particle recycling and the degree of complexity of pathways that large hail trajectories can take through the storm.

### 1.4. Combining modeled hail trajectories with in situ surface hail measurements

Understanding hail growth is critical to furthering our ability to better forecast damaging hail, thus reducing the human and agricultural impact. Since the human impact occurs disproportionately at the surface (although it is noted that hail both surface and aloft is a considerable threat to aviation), improved understanding of surface hailfall characteristics represents a critical gap in our process understanding of hailstorms. One way to verify models and improve understanding of hail impacts is by examining hail swath characteristics and formation processes. Hail swath information is limited due to the ability to observe sub-storm-scale details at the larger spatial scales of moving storms. Hailstone melting rates at the surface increases the difficulty of accurately observing fresh hailfalls. Brook et al. (2021) produced a simulated hail swath to highlight imminent hail impacts with greater success than currently available hail swath tools such as hail differential reflectivity ($H_{DR}$; Depue et al. 2007), maximum expected size of hail (MESH; Witt et al. 1998), and the hail size discrimination algorithm (HSDA; Ortega et al. 2016), which are mostly used to detect hailstones aloft rather than at the surface.

A storm simulation by Kumjian et al. (2021) that includes Lagrangian hail growth trajectories and derived hail swaths (i.e., the aggregate surface impact locations of simulated hailstones) has shown that large surface hail tends to concentrate from the left-forward through left-rear to rear of simulated supercells. Employing a detailed analysis of polarimetric Doppler single-radar data from the intense 31 May 2013 El Reno, OK supercell combined with crowd-sourced surface hail reports, Witt et al. (2018) showed that giant hail tended to concentrate and grow preferentially within high reflectivities just outside of the bounded weak echo region (BWER) on the middle level flanks of the intense, order ~ 10-15 km wide mesocyclonic main updraft. Witt et al. (2018) also showed that giant hail fell to ground concentrated either in the right forward storm flank (i.e., "forward flank giant hailfall" or FFGH) or in the left-rear flank (i.e., "rear flank giant hailfall" or RFGH) at ranges of 5-10 km from the updraft core.

To fill the gap created by our limited observations, laboratory studies have revealed much about the processes behind hail growth. Several of the microphysical parameterizations (but not all) employed in hail trajectory models to simulate hail growth have been based on empirical data from laboratory experiments, including the hail growth model used in the present thesis. Foremost among the modeled hail growth conditions, the “wet” or “dry” growth mode (Ludlam 1958; Pruppacher and Klett (1997); Lamb and Verlinde 2011) is critically important to accurately modeling hailstone growth. The hail growth regime is dependent on the environmental characteristics at the hailstone’s in situ location. To more accurately depict the hailstone’s evolving physical characteristics, the hailstone's heat balance must consider the transfer of latent heating from freezing, melting, evaporation, and conduction via forced convection between the hailstone and its immediate environment. If ambient temperature is below 0 °C and all the collected supercooled cloud water freezes on the hailstone (i.e., dry growth), the temperature of the hailstone will likewise be below 0 °C. If ambient temperature is below 0 °C and not all of the collected supercooled water freezes (i.e., wet growth), the temperature of the hailstone is at 0 °C. Pruppacher and Klett (1997) and section 2.1.1 of Allen et al. (2019) describe further aspects of the hailstone growth process. Chapter 3 of this thesis provides a highly detailed description of the present hail growth trajectory model.

Hailstone characteristics such as shape, size, oblateness, mass, and density are dependent on growth regime. Dry growth ice appears visually as opaque, while wet growth ice appears as generally clear (perhaps including long, narrow air inclusions potentially related to ice layer fractures). The opaque appearance of dry growth ice is due to many small air bubbles being trapped as supercooled water is immediately frozen into a low-density rime formation with many droplet-scale air inclusions. In contrast, wet growth contains no air bubbles due to solid-ice density growth of the ice core from the base of the surrounding ice-bath temperature water shell. Kumjian et al. (2020), in a recent case study of gargantuan hail in Argentina, concurs that the observed gargantuan hailstones had a thick, clear layer on the outside of the hailstone, indicating significant wet growth in the final stages of the hailstone's growth. Knight and Knight (2005) hypothesized that the only growth trajectory similarities between the largest hailstones may be the time spent in the wet growth regime at the end of the life cycle in a case study of giant hail in Nebraska. Pruppacher and Klett (1997) explains how larger hailstones have higher temperatures due to increased size, increased liquid water being collected, and an increase of frequency of collisions. Hailstones with higher temperatures would be more likely to experience wet growth, explaining why wet growth for larger hailstones is a common observation.

To the author's knowledge, the study of a radar-analyzed Oklahoma multicell storm by Ziegler et al. (1983) conducted the first direct comparison of detailed numerically simulated hail growth trajectories with in-situ fresh surface hail collections. A unique aspect of the Ziegler et al. (1983) analysis was the comparison of the subsequently thin-sectioned sampled hailstone structures (e.g., Knight 1981) and a Deuterium-analyzed isotopic history of the in-situ ice growth layer temperatures (e.g., Knight et al. 1975; Knight et al. 1981) to selected, numerically modeled hailstones. Observations of the sizes and internal structures of surface hailstones have not commonly been employed to validate the degree of realism of simulated hailstones (and thus by inference the physical growth model's realism). Although Ziegler et al. (1983) demonstrated a level of realism of their numerically simulated hail growth trajectories against the detailed independent surface hail observations, the number of observed hailstones and computed co-located growth trajectories as well as the overall comprehensiveness of the employed hail growth model all presented limitations. The above literature review includes several trajectory-based studies of significant severe (> 5 cm) hail. However, to the author's knowledge, there has been a dearth of studies prior to the present thesis that have extended the methods of Ziegler et al. (1983) to comparison of simulated and observed hail that exceed giant (> 10 cm) or gargantuan

(> 15 cm) maximum dimensions (e.g., Kumjian et al. 2020). Since models are not able to simulate all unique growth aspects of hailstones, direct comparison of observed hailstones is highly desirable to validate model output in physical detail.

The present thesis creates a new, unique dataset by combining multi-Doppler radar wind and reflectivity analysis, diabatic Lagrangian analysis (DLA) retrievals of temperature and water substance, and a complex hail trajectory model to create millions of numerically simulated hail trajectories in the Kingfisher, OK supercell on 29 – 30 May 2012. The present simulated hailstone samples at the surface are compared with independent research (non-operational) ground hail observations. Since only one supercell case is presented, results are focused on the exploration of trajectory characteristics that control hailstone size rather than an examination of storm-environmental sounding impacts on the supercell's hail production. With the substantial number of trajectories generated, results of trajectory characteristics are not quantitatively limited. Details of the data used to create our trajectory dataset are presented in Chapter 2, while the numerical hail growth is presented in detail in Chapter 3. In Chapter 4, characteristics of trajectories and hailstone positions are analyzed. In Chapter 5, hailstones at the surface are analyzed and hailstone observations are compared to the simulated hailstones. We explore the sensitivities to hail growth physics in Chapter 6. Finally, the discussion and conclusions are presented in Chapters 7 and 8 respectively.

# Chapter 2: Data and Analysis Methods

## 2.1. Deep Convective Clouds and Chemistry Experiment (DC3)

The Deep Convective Clouds and Chemistry Experiment (DC3) was designed to investigate the dynamical, physical, and lightning processes of deep convection and their effects on upper troposphere composition and chemistry (Barth et al. 2015). The experiment was conducted in three different regions of the United States from 1 May 2012 to 30 June 2012 including northeastern Colorado, west Texas to central Oklahoma, and northern Alabama.

On 29 May 2012 near Kingfisher, OK a supercell was observed by DC3 in central Oklahoma as it produced large hail up to 12 cm and an EF-1 tornado in the Oklahoma City, OK metropolitan area. Multiple studies have been published about microphysical properties, electrification and lightning, and secondary convection in the Kingfisher supercell (DiGangi et al., 2016, hereafter referred to as D16; Waugh et al. 2018; Chmielewski et al., 2020; DiGangi et al., 2021), as well as a high-resolution cloud model simulation of the Kingfisher storm (Davenport et al. 2019) and additional convection-resolving regional model simulations of the Kingfisher storm and neighboring supercell deep convection (Yang et al. 2015; Bela et al. 2018). The wealth of data on the Kingfisher, OK supercell makes it an excellent subject for case study in the present thesis.

## 2.2. Storm overview

Although a prior analysis of the storm environment is presented in D16, environmental characteristics relevant to hail formation will be recapitulated here. On 29 May 2012, a positively tilted upper-level trough was present across the upper Great Lakes and the Canadian province of Ontario. There was broad northwesterly flow at 500 hPa in Oklahoma, and a subtle shortwave developed leading to weak cyclogenesis in the TX Panhandle by early morning on 29 May.

There was as stationary front along the KS/OK border and a dryline that developed in the TX Panhandle and moved eastward into western OK. Far-environmental, storm-following mobile soundings measured MLCAPE in excess of 2500 J $kg^{-1}$ in north central OK as convection initiation occurred. The Kingfisher, OK supercell initiated east of the dryline bulge in northwest OK at approximately 2134 UTC (Davenport et al. 2019).

It is important to note how the storm structure changes over time, as storm structure and airflow patterns can alter hail growth even with steady state environmental conditions (Kumjian et al. 2021) as assumed for the present DLA retrievals (section 2.6) and hail trajectories (Chapter 3). The Kingfisher supercell subsequently split at 2205 UTC (Davenport et al. 2019) and the right moving Kingfisher storm became the dominant, southernmost supercell as it tracked southeastward towards the Oklahoma City metropolitan area. The updraft of the Kingfisher supercell was crescent shaped and was oriented with a predominantly downshear major axis for much of its lifecycle. The updraft was steadily strengthening, but pulsed upward at approximately 2302, 2318, 2330, 2348, and 0000 UTC as indicated by transient increases in updraft mass flux and updraft volume relative to a linear upward trend of updraft intensity (D16, their Figure 11). After 2330 UTC, the updraft volume is consistently larger for the remainder of the analysis period (Figure 1).

Data was collected on this supercell during the period 2251 UTC 29 May to 0000 UTC 30 May. From the multi-Doppler radar volumes, both multi-Doppler analyses and diabatic Lagrangian analysis (DLA) retrievals were generated. The data and analyses are detailed in the following sub-sections.

## 2.3. Mobile radars

Three mobile radars, specifically the SMART-R1 (SR1), SMART-R2 (SR2), and the NOAA/NSSL X-Pol (NOXP) radars (Biggerstaff et al. 2005; Burgess et al., 2010), observed the Kingfisher supercell on 29 – 30 May. SR1 and SR2 are 5-cm wavelength (C-band) dual-polarimetric Doppler radars, while NOXP is a 3-cm wavelength (X-band) Doppler dual polarization radar. The three mobile radars were deployed in a triangular array (Figure 2). The mobile radar obtained volume scans at three-minute intervals between 2251 UTC 29 May and 0000 UTC 30 May 2012.

## 2.4. Soundings

Three storm-following, mobile far-environmental soundings were launched in the low-level inflow to the Kingfisher, OK supercell on 29 – 30 May. The soundings were launched 3 miles north of Geary, OK at 2029 UTC (Figure 3a), 20 miles east of Watonga, OK at 2255 UTC (Figure 3b), and 6 miles northeast of El Reno, OK at 0020 UTC (Figure 3c). Two in-storm soundings were also launched on this day at 2323 UTC (Waugh et al. 2018) and 0045 UTC (not shown). The 0020 UTC sounding (Figure 3c) is used to prescribe the storm environment for the DLA retrievals (section 2.6). The hodographs of all three far-environmental mobile soundings are shown in Figure 3d.

## 2.5. Radar analysis

The mobile radar data was manually edited by DiGangi (2014, hereafter referred to as D14) and D16, but important aspects will be summarized here. In the editing stage, errors such as velocity aliasing, ground targets, noise, second-trip echoes, and range-folding are either corrected or else removed from the data. An attenuation correction scheme was applied to the reflectivity data to improve the subsequent multi-Doppler reflectivity field analysis (D14). A time series of multi-Doppler analysis was generated following radar editing using a two-pass Barnes interpolation (Majcen et al. 2008) with smoothing parameter $\kappa$ = 2 km$^2$ to interpolate the mobile radar data to the fixed, ground-relative radar analysis grid (90 km x 60 km x 17.5 km). Analyses were dual-Doppler based on the radar pair providing optimal viewing geometry at each analysis time. Output variables include the Cartesian west-east, south-north, and vertical wind components (u, v, and w respectively, with units of m s$^{-1}$) and the radar reflectivity Z (dBZ). Further details of the radar analysis methodology for the 29 May 2012 Kingfisher supercell can be found in D14 and D16.

**2.6. Diabatic Lagrangian analysis (DLA)**

The implementation of the DLA for 29 – 30 May is described in detail by D14 and D16, but will be summarized here. The DLA is an innovative technique used to retrieve the 3-D, time dependent fields of potential temperature and mixing ratios of water vapor and hydrometeors from the input 4-D radar analysis data (Ziegler 2013a,b, hereafter referred to as Z13a,b). The additions of predicted cloud ice mixing ratio and diagnosed snow mixing ratio to the DLA are reported by D16. The DLA has been applied in studies of the 29 – 30 May 2012 Kingfisher supercell by Yang et al. (2015), Waugh et al. (2018), Bela et al. (2018), and Chmielewski et al. (2020). The DLA output variables are used to obtain a realistic, 4-D depiction of the storm's thermal and hydrometeor structure as required input to the detailed hail growth trajectory model.

The first step of the DLA employs wind fields obtained from the multi-Doppler radar analysis (section 2.5) to calculate on the order of 1 million backward, ground-relative air trajectories into the inflow environment of the Kingfisher supercell. The 30 May 0020 UTC base-state sounding (as described in section 2.4) is used to interpolate the base state potential temperature $\theta(z)$ (K), water vapor mixing ratio $q_v(z)$ (g kg$^{-1}$), and pressure $p(z)$ (mb) to the initial height (km AGL) of each Lagrangian airflow trajectory in the local inflow environment. A system of ordinary differential equations expressing conservation of heat and water substance following the parcel motion is integrated forward in time from the initial points along the air trajectories returning from the inflow environment to the originating grid points. The rain, graupel/hail, and snow particle size distributions all assume an inverse-exponential form following supporting information in Gilmore et al. (2004). A closure scheme, based on a modeled-supercell observing system simulation experiment that partitions the total returned power from reflectivity Z under the aforementioned assumption of inverse-exponenential precipitation size distributions, is used to diagnose the fields of rain mixing ratio $q_r$ (g kg$^{-1}$), graupel/hail mixing ratio $q_{gh}$ (g kg$^{-1}$), and snow mixing ratio $q_s$ (g kg$^{-1}$) under the constraint that the summed partial precipitation returned powers equals the radar-observed total power (Z13a,b; D16). The freezing and -15 C levels, which are used in the precipitation diagnosis scheme, are also prescribed from a representative moist adiabat of the base-state sounding. The resulting predicted 3-D gridpoint DLA fields of potential temperature $\theta$ (K), water vapor mixing ratio $q_v$ (g kg$^{-1}$), cloud liquid water mixing ratio $q_c$ (g kg$^{-1}$), and cloud ice mixing ratio $q_x$ (g kg$^{-1}$) are used to derive additional microphysical variables such as virtual potential temperature, equivalent potential temperature, relative humidity RH, and parcel lifted condensation level LCL.

**2.7. Observed hail dataset**

The Insurance Institute for Business and Home Safety (IBHS) sampled 45 hailstones and recorded hailstone characteristics including maximum diameter, mass, and location (Giammanco and Brown 2013). Additionally, 20 of these hailstones included photographs of the hailstones, providing context to growth characteristics such as wet growth (clear ice) or dry growth (opaque ice). The recorded variables from the observed IBHS hailstones are also output by the hail growth trajectory model for the simulated hailstones, allowing evaluation of the hail growth model by the independent IBHS observations. Additionally, local storm reports (LSRs) obtained from the National Weather Service (NWS) were also used as a qualitative validation method of the simulated hailstones.

# Chapter 3: Hail Trajectory Model

HAILCAST was developed combining a time dependent hail model with a one-dimensional steady-state cloud model (Poolman 1992). Later improvements were made to HAILCAST by Brimelow et al. (2002, 2006) and Jewell and Brimelow (2009). Limitations of using a time dependent hail model with a one-dimensional steady-state cloud model motivated the development of WRF-HAILCAST (Adams-Selin and Ziegler 2016, hereafter referred to as ASZ16). WRF-HAILCAST coupled the time dependent hail model with a convection allowing model (CAM) and included significant updates to the hail model physics. Improved model physical processes included varying initial embryo size, varying hailstone density, varying ice collection efficiency, mass growth by vapor deposition, and modifying the liquid shedding threshold to attempt to account for tumbling. A major improvement of WRF-HAILCAST relative to HAILCAST was the integration of the hail physics and simplified trajectory calculations into the Advanced Research version of the Weather Research and Forecasting Model (WRF-ARW) (ASZ16). WRF-HAILCAST was further refined as informed by its ongoing operational performance assessment during the annual National Severe Storms Laboratory (NSSL)/Storm Prediction Center (SPC) Spring Forecast Experiments. With the recent introduction of the WRF-HAILCAST hail growth physics module into several additional CAMs, including the US National Weather Service (NWS) Unified Forecast System (UFS) FV3 model (Adams-Selin et al. 2022) and the German Weather Service COSMO and Swiss mesoscale ICON models, the term "CAM-HAILCAST" will hereafter be substituted for "WRF-HAILCAST". A summary of CAM-HAILCAST modifications can be found in Adams-Selin et al. (2019, 2022).

In the present study, the latest version of the hail physics from CAM-HAILCAST (ASZ16) is used with selected modifications to compute hail trajectories in a radar-observed storm case for which a thermal-microphysical DLA retrieval dataset was also available. Since other versions of HAILCAST are presently being developed by other investigators, the term "ASZ16-HAILCAST" will hereafter be substituted for "HAILCAST". The 3-D, time-dependent temperature, moisture, and airflow fields from the DLA and radar analyses herein are input to the ASZ16-HAILCAST hail physics module in place of the CAM-HAILCAST (ASZ16) predicted variables. The DLA provides realistic in-storm thermal and microphysical fields and sounding-estimated environmental conditions. The combination of the ASZ16-HAILCAST physics with 4-D airflow and microphysical fields yields the hail trajectory model used in this study. The hail trajectory module is highly customizable, allowing the creation of a unique hail trajectory dataset. Allowable physical options will be noted throughout the chapter.

The ASZ16-HAILCAST growth physics assumes a spherical hailstone. The growth physics have been updated herein to optionally allow for the case of oblate spheroidal hailstones − a novel feature compared to previous models that conventionally assume spherical hail. Variables such as terminal velocity, horizontal cross-sectional area, and heat transfer are all affected by hailstone oblateness, and therefore must also be modified accordingly. Optional treatments of surface water retention/shedding and cloud ice collection are also included herein. In the following sub-sections, differences in the growth equations to account for optional non-sphericity, surface water retention and shedding, and cloud ice collection are noted. The various hail growth model variables and parameters described in sections 3.1-3.10 are listed in Table 1.

**3.1. Hailstone terminal velocity**

The hailstone terminal velocity or fallspeed $V_t$ (m $s^{-1}$) is calculated for the case of spherical hailstones via a dependence on the Reynolds number ($Re_X$) using methods from Rasmussen and Heymsfield (1987a, hereafter referred to as RH87a), as also applied in the

ASZ16-HAILCAST model. The terminal velocity of spherical hail is calculated from an expression of the form (RH87a)

$$V_{t\ \text{(spherical)}} = \frac{\nu_d Re_X}{\rho_a D}, \tag{1}$$

where $Re_X = \left(\frac{X}{0.6}\right)^{0.5}$ is the Reynolds Number, $X = \frac{8mg\rho_a}{\pi\nu_d}$ is the Best Number, $\nu_d$ is the dynamic viscosity of air, $\rho_a$ is the density of air, D is the spherical hail diameter (m), $m$ is the mass of the hailstone (kg), and $g$ is the gravitational acceleration (m s$^{-2}$). The dynamic viscosity is calculated via

$$\nu_d = 1.718 \times 10^{-5}\left(\frac{393.155}{T_a + 120}\right)\left(\frac{T_a}{273.155}\right)^{3/2}$$

where $T_a$ (K) is air temperature in K. RH87a computed $Re_X$ as a function of empirical fits to the Best Number X spanning four prescribed X subranges. The four Best-Reynolds number relationships provided in Eqs. (B1)-(B4) in RH87a were based on a drag coefficient $C_D$ of 0.6. To avoid undefined numbers, a slight correction was made to Eq. (B1) in the form

$$\log_{10} Re_x = -1.7095 + 1.33438 \log_{10} X - 0.11591(\log_{10} X)^2$$

at all points where $X < 500$. Further explanation of the methodology and $V_t$ equations can be found in Appendix B of RH87a and section 2b of Miller et al. (1988).

For the case of hailstones that are herein assumed to be oblate spheroids (e.g., Knight 1986), the major hailstone axis dimension $D_{max}$ (m) is substituted for spherical hail diameter D. The major axis dimension $D_{max}$ is obtained from the model-predicted equivalent spherical volume hailstone diameter $D_{eq}$ (m) employing the 3D hail data regression from Figure 9 of Shedd et al. (2021; hereafter referred to as S21), with omission of their small intercept value to approximate a regression-through-origin (RTO) data fit. Lesins and List (1986) found that hail grown in a laboratory wind tunnel via prescribed canting angle and gyration and spin rates tended to develop and maintain an approximately oblate spheroidal shape during growth. Note that the area of the major axis of an oblate spheroid (i.e., a circular cross-section) canted at angle $\theta$ is $\pi {D_{max}}^2 cos(\theta)/4$. Although the cross-sectional area of an oblate spheroidal hailstone with minor axis canted at 30 deg (Lesins and List 1986) would be roughly 87% of the horizontally-oriented oblate spheroidal (circular) cross-sectional area, the objective of the present hail model application is to estimate the largest possible growth enhancement due to oblateness. Furthermore, Heymsfield et al. (2018, hereafter referred to as H18) cited their own wind tunnel observations along with results of Roos and Carte (1973) and the data analysis of Böhm (1989) to conclude that oblate spheroidal hail tends to exhibit a stable fall mode with the major axis approximately normal to the flow. Hence, the major axis of the present modeled oblate spheroidal hailstones is assumed to be horizontally oriented.

The terminal velocity $V_t$ for oblate spheroidal graupel and hail respectively (Heymsfield et al. 2020, their Eqs. 2a-b, hereafter referred to as H20; see also H18) are combined with air density altitude scaling following Ziegler et al. (1983, hereafter referred to as Z83) and Kumjian and Lombardo (2020, hereafter referred to as KL20), and take the form

$$V_{t\ (\mathrm{oblate})} = 7.6{D_{max}}^{0.89}\left(\frac{1.225}{\rho_a}\right)^{0.5}, D_{max} < 1.5\ cm \tag{2}$$

for graupel or small hail and

$$V_{t\ (\mathrm{oblate})} = 8.4{D_{max}}^{0.67}\left(\frac{1.225}{\rho_a}\right)^{0.5}, D_{max} > 1.5\ cm \tag{3}$$

for large hail, where 1.225 is standard mean sea level air density (kg $m^{-3}$). The present model applies $V_t$ from Eqs. (2)-(3) in the oblate spheroidal hail case. Terminal fallspeeds computed from Eqs. (2)-(3) more accurately represent oblate spheroidal hailstones, including large hailstones via Eq. (3), and are also smaller than those from Eq. (1) (H20). The latter impact on fallspeed magnitude is hypothesized to introduce sensitivity in the resulting hail trajectories under the contrasting optional assumptions of either spherical or oblate spheroidal hail (H18; H20).

### 3.2. Parameterization of heat transfer coefficient $\chi$ for oblate spheroidal hail case

The heat transfer coefficient $\chi$ is parameterized based on the derived empiricism from Macklin (1963, his Figure 1, hereafter referred to as M63) and the 3-D hailstone observations of S21. M63 provides a linear regression fit of $\chi$ as a function of the minimum oblate spheroid aspect ratio $\varphi_{min} = D_{min}/D_{max}$, where the minor and major axes are respectively $D_{min}$ (m) and $D_{max}$. S21 provides a linear empirical fit of $D_{max}$ versus $D_{eq}$ based on 150 hailstones collected and 3D scanned by IBHS. To match the 3D-scanned hailstones from S21 to the M63 empiricism of $\chi$ versus $\varphi$, a representative value of $\varphi = \varphi_{min}$ is obtained from the 3D scanned hailstone data as follows.

Two approaches have been employed to specify $\varphi = \varphi_{min}$. In the first method, a value of $\varphi_{min}$ = 0.51 has been estimated from inspection of Figure 5c in S21. An independent calculation of aspect ratio statistics from the 3-D hailstone data in Figure 5c of S21 (not shown) indicates that the median aspect ratio is in fact nearly equal to the estimated value of $\varphi_{min}$ = 0.51 (Matthew Kumjian, personal communication, 2022). In the second method, the equivalent spherical and oblate spheroidal volumes respectively are equated to yield

$$\pi {D_{\mathrm{eq}}}^3/6 = \pi {D_{\max}}^2 D_{\min}/6.$$

Rearranging terms, substituting $D_{\max} = aD_{\mathrm{eq}}$ (S21) with neglect of S21's small y-intercept value, and solving for $D_{min}$, there follows

$$D_{\min} = {D_{\mathrm{eq}}}^3/{D_{\max}}^2 = D_{\mathrm{eq}}/a^2.$$

Substituting the latter expressions for $D_{max}$ and $D_{min}$ in the minimum oblate spheroidal aspect ratio definition yields

$$\varphi_{\min} = D_{\min}/D_{\max} = D_{\mathrm{eq}}/a^2 D_{\max} = 1/a^3,$$

where a = 1.3978 and $\varphi_{min}$ = 0.37. Since the latter derived value could be somewhat low-biased judging from Figure 5c of S21, the larger estimated value is employed in the present hail growth model. It should be noted that assuming oblate spheroidal geometry implies semi-major axes equal to $D_{max}$, whereas the 3D stones are actually better characterized by tri-axial ellipsoids with $D_{min} < D_{int} < D_{max}$ (where $D_{int}$ is the intermediate dimension), in which case the volume of assumed oblate spheroids with $D_{max}$ will somewhat overestimate actual 3-D stone volumes (S21). A "ramp" weighting function is used to approximate the linear regression of $\chi$ versus $\varphi$ using the lowest and highest values of $\varphi$ and $\chi$ from Figure 1 of M63. The empirical $\chi$ expression takes the form

$$\chi = [(1 - wgt)(\chi_{\mathrm{low}})] + [(wgt)(\chi_{\mathrm{high}})], \tag{5a}$$

where

$$wgt = \frac{\varphi_{\min} - \varphi_{\mathrm{low}}}{\varphi_{\mathrm{high}} - \varphi_{\mathrm{low}}} \tag{5b}$$

and $\varphi_{\mathrm{low}}$ = 0.4, $\varphi_{\mathrm{high}}$ = 1, $\chi_{\mathrm{low}}$ = 0.91, $\chi_{\mathrm{high}}$ = 0.76, and "low" and "high" refer to the lower and upper limits of the ramp function's $\varphi$ coordinate respectively (M63).

In summary, the present hail growth model assumes $\chi$ = 0.76 for the case of spherical hail (e.g., RH87a, ASZ16). For the case of oblate spheroidal hail with $\varphi_{\mathrm{low}} \leq \varphi_{\min} \leq \varphi_{\mathrm{high}}$, $\chi_{\mathrm{low}} \leq \chi \leq \chi_{\mathrm{high}}$. Although the lower value of $\varphi$ = 0.37 would imply an extrapolated value of $\chi$ = 0.91 (M63) that in turn would increase heat and vapor transfer relative to the hailstone, and although hail growth by collection of supercooled cloud water (section 3.3) is heat transfer dependent (Pruppacher and Klett 1997), the conservatively smaller value $\chi$ = 0.8825 (assuming $\varphi$ = 0.51) is instead employed here for the case of oblate spheroidal hail.

**3.3. Collection of cloud water**

Collection of supercooled liquid water provides the main mass source of growth in hailstones, although the amount of collection can vary depending on several factors including growth regime. For both dry growth (i.e., all accreted water is frozen) and wet growth (i.e., only a fraction of accreted water is frozen, with the unfrozen fraction remaining on the hailstone surface), the mass rate of change due to collection of supercooled water (i.e., accretion) takes the form

$$\left(\frac{dm}{dt}\right)_{\text{water}} = \frac{\pi}{4} D^2 V_{\text{t}}\, q_c E_{\text{cw}}, \tag{6}$$

where $m$ is the particle mass, $q_c$ is the cloud water content and $E_{\text{cw}}$ is the cloud water collection efficiency. The falling hailstone sweeps out cloud droplets within the cylindrical volume equal to the horizontal circular hailstone area multiplied by the fall distance $V_t\Delta t$. The collection efficiency of cloud water droplets $E_{cw}$ during sweepout to a good approximation is conventionally assumed to have a value of unity (e.g., Z83). For the case of oblate spheroidal hailstones, $D_{max}$ is substituted for D in Eq. (4), effectively increasing the sweepout area under the assumption that the major axis of the oblate spheroidal hailstone is horizontally oriented (see section 3.1). The density of the rimed layer in dry growth is determined via the empirically derived layer density $\rho_l$, cloud droplet diameter $D_c$, and hailstone impact velocity $V_{imp}$ and temperature $T_s$ as described in Heymsfield and Pflaum (1985) and ASZ16. Impact velocity was calculated via a linear interpolation between the four Reynolds number, Stokes number, terminal velocity, and impact velocity relationships presented in Eqs. (7) – (10) in Rasmussen and Heymsfield (1985).

Although all collected supercooled cloud water is frozen during dry growth, during wet growth only a fraction $F_w$ of the collected cloud water remains unfrozen while the remaining fraction (1 - $F_w$) freezes. The unfrozen collected cloud water can either soak into previously porous rime if the hailstone bulk density is less than that of solid ice (assumed to be 900 kg $m^{-3}$) following Z83, or else can collect in a surface water shell if the hailstone is at solid ice density. Although ASZ16-HAILCAST assumed that shedding of excess water can occur if the surface water shell mass $M_{sfc}$ (kg) exceeds a threshold value $M_{sfc} = M_{wcrit} = 1 \times 10^{-4}$ kg (see ASZ16 for discussion), a smaller default fixed value of $M_{wcrit} = 1 \times 10^{-10}$ kg is assumed in the present study. However, the present study also optionally allows excess surface water to be shed if $M_{sfc}$ exceeds $M_{\mathrm{wcrit}} = 0.268\, x\, 10^{-3} + 0.1389 M_{\mathrm{ice}}$ and $D_{eq}$ exceeds 9 mm (RH87a), where $M_{ice}$ (kg) is the mass of the hailstone's ice core. Thus, by assuming a smaller fixed $M_{wcrit}$ value, the impact of employing the much larger optional $M_{wcrit}$ value results in a magnified measure of the potential shedding sensitivity. For wet growth, the ice layer density is set to 900 kg $m^{-3}$. The bulk hail density during wet growth is updated by dividing the volume of the hailstone by the mass of the hailstone that includes any soaked water. Additional information and a sensitivity test of the optional shedding threshold is presented in Chapter 6.

Neither raindrop nor snow mass collection rates are considered by the present hailstone growth model (e.g., Z83). Although KL20 suggest that raindrop collection may be a nonnegligible source of hailstone mass under certain ideal circumstances, demonstrating a plausible hypothetical role of raindrop collection would require either laboratory or detailed numerical model data on the collection efficiency of raindrops by hailstones which presently do not exist. Due to the rather large impact momentum difference of raindrops with hailstones, and the aforementioned lack of reliable data to prescribe raindrop collection efficiency, splashing raindrop collisions could conceivably result in loss of an appreciable but unknown fraction of intercepted raindrop mass. Similarly for a dry hailstone surface, the large impact momentum difference would likely result in snow particle shattering and rebound of the small collision fragments. Furthermore, both raindrops and snow particles are also in extremely low total concentrations relative to cloud droplets, thus limiting effective raindrop-hail and snow-hail collision rates (e.g., Knight and Knight 1970; Ziegler 1985; Ziegler 1988; Knight et al. 2008).

**3.4. Collection of cloud ice**

Similar to the mass rate of change due to collection of cloud water, the mass rate of change due to collection of cloud ice takes the form

$$\left(\frac{dm}{dt}\right)_{\text{cloud ice}} = \frac{\pi}{4} D^2 V_{\text{t}}\, q_x E_{\text{cx}}, \tag{7}$$

where $q_x$ is the cloud ice content and $E_{\text{cx}}$ is the cloud ice collection efficiency. For oblate spheroidal hailstones, $D_{max}$ is substituted for D. In several previously developed hail growth models (e.g., ASZ16), $E_{cx}$ has been assumed to be dependent of the hailstone temperature $T_s$. It is conventionally assumed that $E_{cx}$ has unit value if the ambient environmental temperature $T_a$ is at or above 0 °C, whereas $E_{cx}$ is assumed to be zero at or below -40 °C (e.g., ASZ16). For hailstone temperature $T_s$ ranging between 0 °C and -40 °C, $E_{cx}$ takes the linear functional form

$$E_{\text{cx}} = 1 - \frac{273.155 - T_s}{40}, \tag{8}$$

which substitutes $T_s$ for $T_a$ in the analogous $E_{cx}$ expression of Z83. Since physical processes governing $E_{cx}$ in nature are poorly understood, an optional cloud ice collection efficiency expression has been added to the model. In this optional treatment, $E_{cx}$ has a value of unity (all colliding cloud ice particles stick) if the hailstone is in wet growth, whereas $E_{cx}$ is assumed to be zero (i.e., purely rebounding collisions) during dry growth (KL20). If cloud ice collection dominates the local hail growth (a very rare occurence), the ice layer density is set to 700 kg m$^{-3}$. A sensitivity test result using the optional $E_{cx}$ treatment of KL20 is reported in Chapter 6.

### 3.5. Vapor diffusion

Vapor growth or decay via deposition or sublimation respectively, which follows Eq. (4) of ASZ16 as adapted from RH87a and Pruppacher and Klett (1997), takes the form

$$\left(\frac{dm}{dt}\right)_{\text{vapor}} = \frac{2\pi D \overline{f_v} D_v}{R_v}\left(\frac{e_{s,a}}{T_{\mathrm{a}}} - \frac{e_{s,s}}{T_{\mathrm{s}}}\right), \tag{9}$$

where $\overline{f_v}$ is the water vapor ventilation coefficient, $D_v$ is diffusivity of water vapor in air, $R_v$ is the gas constant for water vapor, and $e_{s,a}$ and $e_{s,s}$ are the saturation vapor pressure of the ambient air and the hailstone surface layer respectively. The values of $\overline{f_v}$ and $D_v$ were obtained from Table A1 of RH87a. If vapor deposition is the main source of growth, the solid-ice layer density in the time step is set to 900 kg m$^{-3}$.

### 3.6. Heat balance condition (dry growth)

When a hailstone grows or melts, latent heat is released to or extracted from the air. To account for the physical changes occurring due to freezing and melting, a set of equations are used to determine the heat balance. The heat balance equations used were adapted by Poolman (1992), Brimelow et al. (2002), and ASZ16 from RH87a as shown in their Table 1 and Eqs. (3)-(5). It is important to note that all empirical relationships derived in RH87a were provided in cal-g-s units, with temperature expressed in Celsius and length in cm. For the remainder of the section, all relationships discussed use the latter system of units unless explicitly stated otherwise. The present model subsequently converts all quantities to J-kg-s with temperature expressed in Kelvin and length in m as required to maintain SI units of predicted quantities.

Within ASZ16-HAILCAST, the temperature of the surface of the hailstone during dry growth is determined via an expression of the form

$$T_s = T_s\left(\frac{m - \Delta m}{m}\right) + \frac{\Delta t}{mc_{p,i}}\left[\frac{\Delta q}{\Delta t}\right] + \frac{\Delta m_w L_m}{mc_{p,i}},$$

where $\Delta m$ is the change in hailstone mass since the last timestep, $\Delta q$ is the change in heat content, $L_m$ is the latent heat of melting, and $c_{p,i}$ is the specific heat capacity of ice. Within this equation, the first term represents the previous hailstone temperature per unit of mass, the second term the change in temperature due to heating transfer processes, and the third term the change in temperature resulting from the release of latent heat due to freezing. The $\Delta q/\Delta t$ term in brackets is then adapted from Eq. (3) of RH87a as described above, resulting in a modified hailstone temperature expression of the form

$$\begin{aligned} T_s &= T_s\left(\frac{m - \Delta m}{m}\right) \\ &\quad + \frac{\Delta t}{mc_{p,i}}\left[2\pi D\overline{f_H}k_a(T_a - T_s) - \overline{f_v}L_e D_v\left(\rho_{v,s} - \rho_{v,a}\right) + \frac{\Delta m_w}{\Delta t}\left(c_{p,w}T_a\right)\right. \\ &\quad \left. + \quad \frac{\Delta m_i}{\Delta t}\left(c_{p,i}T_a\right)\right] + \frac{\Delta m_w L_m}{mc_{p,i}}, \end{aligned} \tag{10}$$

where $\overline{f_H}$ is the mean ventilation coefficient for heat, $k_a$ is the thermal conductivity of air, $L_e$ is the latent heat of vaporization, $\rho_{v,s}$ is the water vapor density at the hailstone surface, $\rho_{v,a}$ is the water vapor density at $T_a$, $c_{p,w}$ is the heat capacity of water, and $\Delta m_i$ is the growth in hailstone mass due to ice accretion since the last timestep. The $\frac{\Delta m_i}{\Delta t}\left(c_{p,i}T_a\right)$ term, although not included in RH87a, is added here to account for heat transfer due to accreted ice.

The $\overline{f_H}$ and $\overline{f_v}$ terms in the $T_s$ equation are defined by Poolman (1992) and Brimelow et al. (2002) to encapsulate all additional dependencies in the heat transfer Eqs. (3), (4), and (5) in Table 1 of RH87a, including the Reynolds (Re), Prandtl (Pr), and Schmidt (Sc) numbers, as well as the heat transfer coefficient $\chi$. Just as the RH87a heat transfer equations are dependent on Reynolds number, so also are the heat ventilation coefficients of the form

$$\overline{f_H} = \begin{cases} 0.78 + 0.308 Pr^{1/3} Re^{1/3}, & Re < 6 \times 10^3 \\ \chi_1 Pr^{1/3} Re^{1/3}, & 6 \times 10^3 \leq Re \leq 2 \times 10^4 \\ \chi_2 Pr^{1/3} Re^{1/3}, & Re > 2 \times 10^4 \end{cases}$$

where the Reynolds number is defined here as $Re = DV_t/\nu$ and the kinematic air viscosity $\nu = 1.252 \times 10^{-5}$. Note that while the latter Re definition differs from the $Re_X$ expressions in the terminal velocity calculations (section 3.1), the resulting computational differences of Re are minimal for the temperature ranges encountered here. To accommodate differing $\chi$ values (section 3.2) from either the spherical hail case ($\chi$ = 0.76) or the oblate spheroidal hail case ($\chi$ = 0.8825), the modified expressions for $\chi_1$ and $\chi_2$ take the form $\chi_1 = \chi$ and $\chi_2 = (\chi - 0.19) + 9 \times 10^{-6} Re$.

It is hypothesized that the value of $\chi$ exerts an important modulating influence on the heat transfer magnitude (Pruppacher and Klett 1997), and thus could play a critical role in hail growth and ultimately the final size of the surface hail distribution. Sensitivity tests involving $\chi$ will be detailed in Chapter 6. If the hailstone is in the dry growth regime and all accreted supercooled cloud can be frozen, the hailstone remains in dry growth. Otherwise if not all the accreted supercooled cloud can be frozen, a transition to wet growth occurs.

### 3.7. Heat balance condition (wet growth)

If the hailstone is in the wet growth regime, $T_s$ remains at 0 °C while excess unfrozen surface water is assumed to remain at ice-bath temperature. The water fraction of the total hailstone mass $F_w$ is the predicted variable. The expression for water fraction $F_w$ takes the form

$$F_w = F_w\left(\frac{m - \Delta m}{m}\right) + \frac{\Delta t}{mL_m}\left[\frac{\Delta q}{\Delta t}\right] + \frac{\Delta m_w}{m}.$$

These three terms can be interpreted as the water fraction of the hailstone before adding the mass $\Delta m$, the depletion of water fraction due to water layer freezing (as regulated by the heat transfer process), and the change in water fraction due to accretion of liquid cloud water. With inclusion of the $\Delta q/\Delta t$ term in brackets from RH87a, the water fraction expression takes the final form

$$F_w = F_w\left(\frac{m-\Delta m}{m}\right)$$

$$+\frac{\Delta t}{mL_m}\left[2\pi D\overline{f_H}k_a(T_\infty) - 2\pi D\overline{f_v}L_e D_v(\rho_{v,\infty}-\rho_{v,0}) + \frac{\Delta m_w}{\Delta t}(c_{p,w}T_\infty)\right.$$

$$\left.+\frac{\Delta m_i}{\Delta t}(c_{p,i}T_\infty)\right] + \frac{\Delta m_w}{m}, \tag{11}$$

where $D_v$ is the diffusivity of water vapor in air. Note here that the temperature of the hailstone is assumed to be 0°C during wet growth. If all of the retained water has frozen, the hailstone is transitioned from wet growth to dry growth.

**3.8. Melting**

Hail melting may occur if $T_a$ is above freezing.  Although additional processes detailed in sections 3.3, 3.5, and 3.7 may impact hail mass during the melting phase, heat transfer critically forces the loss of hailstone ice mass during melting. With substitution of D = 2r (where r is the hailstone radius), the heat transfer rate *h* for a melting hailstone [Eq. (1) of Goyer et al. 1969, hereafter referred to as G69] takes the form

$$h = \frac{\chi\left(Pr^{\frac{1}{3}}k_a\Delta T + Sc^{\frac{1}{3}}L_v D_v\Delta\rho\right)Re^{\frac{1}{2}}}{D}, \tag{12}$$

where $\Delta T$ and $\Delta\rho$ are the difference of temperature and vapor density respectively between the ambient air and the equilibrium state at the hailstone surface. The heat transfer coefficient $\chi$ takes a value of 0.76 for the spherical hail case and is diagnosed in the oblate spheroidal hail case (section 3.2). With substitution of D = 2r, the mass melting rate $\left(\frac{dm}{dt}\right)_{\mathrm{melt}}$ as described by Eq. 3a of G69 takes the general form

$$\left(\frac{dm}{dt}\right)_{\mathrm{melt}} = -\frac{\pi D^2 h}{L_m} + 0.85\pi D D_v \Delta\rho Re^{0.5}. \tag{13}$$

Following Lesins and List (1986) who effectively computed average drag coefficient $\overline{C_D}$ according to $D_{eq}$ for their oblate spheroidal laboratory-grown hailstones, the present melting formulation assumes $D = D_{eq}$ for both the spherical and oblate spheroidal hail cases. It is also noted that although ASZ16 also employed a melting term based on G69, the present melting formulation has importantly been adjusted by substituting variable $\chi$ directly via Eq. (12) to account for the optional spherical or oblate spheroidal hailstone shapes (section 3.2). The $\Delta\rho$ term can make an important contribution to the net hail melting rate in dry ambient air, as evaporation from the water surface offsets forced convective heat transfer from the air to the hailstone surface (G69). It is important to note that whereas G69 made several simplifying assumptions in their hail melting expression by assuming picked values of $\chi$ , Pr, and Sc, the present hail model evaluates the general forms of Eqs. (12)-(13) to allow the latter parameters to vary according to physical principles. The $F_w$ value, which may vary with changing surface water mass during melting, is balanced between shedding loss (section 3.3) and meltwater increase during each timestep. Excess surface hailstone water mass exceeding $M_{wcrit}$ is immediately shed.

**3.9. Computational algorithm for hailstone trajectories**

The first stage of the hail trajectory integration process during each time step is the computation of $V_t$ from the predicted equivalent spherical diameter $D_{eq}$ for the spherical hail case (section 3.1), or in the optional oblate spheroidal hail case by computing $D_{max}$ from diameter $D_{eq}$

and $V_t$ from the diagnosed $D_{max}$ value (section 3.1). The u, v, and w wind components and reflectivity Z (section 2.5) are interpolated from the 4-D radar analyses to the Lagrangian point. The hail trajectory coordinates (x, y, z) are then integrated forward by one time step via the system

$$x_t = x_{t-\Delta t} + u\Delta t, \tag{14a}$$

$$y_t = y_{t-\Delta t} + v\Delta t, \tag{14b}$$

$$z_t = z_{t-\Delta t} + (w - V_t)\Delta t, \tag{14c}$$

where $(\frac{dx}{dt}, \frac{dy}{dt}, \frac{dz}{dt}) = (u\Delta t, v\Delta t, [w - V_t]\Delta t)$ is the temporal change of the ground-relative coordinates of the hailstone Lagrangian point with respect to the radar analysis grid domain, fallspeed $V_t$ is positive and directed downward (section 3.1), and $\Delta t = 1$ s (Table 1).

Following integration of Eqs. 14a-c, the second stage of the hail trajectory integration process is the interpolation of the $\theta$, $q_v$, $q_c$, $q_x$, $q_r$, $q_{gh}$, and $q_s$ fields (section 2.6) from the 4-D diabatic Lagrangian analyses to the updated Lagrangian point. Although the DLA rain, graupel/hail, and snow precipitation mixing ratios are not employed in the present hail trajectory calculations, they are available as microphysical context to help interpret the ambient hailstone trajectory environments. Additional thermal and microphysical parameters required by the subsequent hail physics calculations are then obtained from the Lagrangian-interpolated DLA variables.

The spatio-temporal interpolation of airflow and microphysical data to the hailstone trajectory follows the DLA interpolation method (Z13a,b), except for the case where the hailstone time is after the final radar analysis and DLA retrieval time (0000 UTC 30 May 2012). To accomodate the latter special case, the spatio-temporal interpolation has been modified by shifting the final 3-D data fields downstream in time-to-space assuming steadiness following the observed storm motion to extend the trajectory integration period. If the hailstone trajectory moves outside either the DLA or radar analysis domains, the ambient environmental conditions are approximated from the base-state sounding (Fig. 2c) with assumed zero hydrometeor content.

The third stage of the hail trajectory integration process is to compute the incremental hailstone mass and volume changes, heat budget, hailstone temperature, water fraction, and growth mode from the various hail physics terms. If $T_a > 0$ C, the hailstone mass rates of change from melting (section 3.8) and breakup (section 3.2) are then calculated. Alternately if $T_a < 0$ C, the hailstone mass rates of change from cloud water collection (section 3.2), cloud ice collection (section 3.3), and vapor diffusion (section 3.4) are then calculated. After updating the hailstone $T_s$ and $F_w$ based on the calculated heat budget (sections 3.5 and 3.6 respectively), which includes determination of dry or wet growth mode, the hailstone mass rate of change from water shedding (section 3.2) is then calculated. The hail trajectory model enables the diagnosis of bulk density by carrying predicted hailstone mass $m$ and volume V as independent variables, from which bulk density $\rho_h = m/V$ is updated (Nelson 1983; Z83; Mansell et al. 2010; ASZ16). The separately determined mass and volume changes of the hailstone for each growth or decay process are incrementally applied during each timestep to update the hailstone mass and volume and derive the updated hailstone bulk density.

### 3.10. Initialization of hailstone trajectories

An embryo domain has been defined, within which the hail growth model may prescribe embryo initial locations and physical characteristics within the reflectivity-containing sub-volume (Figure 4). The embryo domain is dimensioned 20 km × 20 km horizontally and from 4.2 km AGL to 11.2 km AGL vertically, and is approximately centered in the main updraft. The embryo grid spacing is set at 250 m in all directions. The optimal embryo domain location has been selected using midlevel vertical velocity and radar reflectivity to identify the updraft location, taking into account prior research that identified the main embryo source regions (see Chapter 1). The major, previously established embryo source regions are all contained within the chosen embryo domain. For each analysis time (i.e., every three minutes), the embryo domain is moved 1 km south and 1 km east to follow the updraft as the storm moves southeastward (Fig. 3). Table 2 displays the time-varying embryo domain origin (lower left corner of the domain) for the 24 analysis times in the Kingfisher storm.

Embryos are initialized at any point within the embryo domain for each analysis time provided that reflectivity exceeds a minimum threshold of 20 dBZ at that point. This reflectivity threshold is predicated on the DLA assumption that precipitation content exists only within radar reflectivities exceeding that threshold value (Z13b). Since the precipitation content through the 4.2 – 11.2 km layer of midlatitude storms is dominated by graupel and hail particles, imposing the reflectivity threshold constraint usefully limits the sub-volume with which hail embryos are most likely. Although the initial diameter and density of the embryos are customizable, an initial density of 500 kg $m^{-3}$ and initial diameter of 7 mm were chosen based on sensitivity test completed in Z83 and ASZ16. Although the latter studies employed multiple millimetric-diameter embryo sizes following conventional practice, the present study instead employs the 7 mm embryo diameter initialized at much finer spatial scales (i.e., 250 m spacing) than previous studies to focus on the growth stage to severe and very large hail. It is important to note that, due to the large and evolving 3-D airflow deformations combined with the highly nonlinear nature of modeled hail size and fallspeed, smaller embryos would likely need to be initialized at even finer spacings than the present 7 mm embryos to produce equivalent numbers of severe (including large, giant, and gargantuan) hailstones at the surface. Airborne in situ measurements by

Heymsfield and Musil (1982), microphysical retrieval analyses by Ziegler (1985, 1988) and Ziegler et al. (1991; including in situ sailplane measurements of graupel size), and videosonde observations of the Kingfisher storm by Waugh et al. (2018) collectively provide ample evidence of abundant, large graupel particles at altitude in midlatitude convective storms. The combined hail trajectory dataset thus created includes forward hail trajectories computed for each radar analysis (three-minute intervals) time between 2251 UTC and 0000 UTC (24 total analysis times). Combining all 24 analysis times to complete our dataset, the total 4-D data size exceeds 3 million trajectories. This large, NetCDF-formatted hail trajectory dataset is archived on the NSSL research RAID system, and is read on a local IMac Pro workstation to produce the various data analysis products.

## Chapter 4: Trajectory Analysis

Over 2.7 million hailstone trajectories resulted from initializing embryos at 24 analysis times. The majority of those trajectories did not result in hailstones, though they are still important to consider. Understanding why large hail does not occur could lead to clues as to why it does occur in other scenarios. Characteristics of the ambient environment along trajectories and the resultant hailstones are explored in this chapter. Prior hail trajectory studies state that horizontal winds and updraft characteristics have a strong influence on the trajectories. The extent that these factors impact where hailstones of differing sizes reside within the storm and their residence times are explored.

### 4.1. Hailstone positions (2251 UTC – 2327 UTC)

To differentiate the trajectories of large hailstones from less impactful smaller hailstones, three categories were crafted for the analysis. Trajectories are categorized by final characteristics including: embryos that melted before reaching the ground, embryos that reached the surface as hailstones or graupel but at sub-severe limits (< 2.5 cm), and embryos that reached the surface as severe hailstones (≥ 2.5 cm). Hereafter, the resultant trajectories from each of the three categories will be referred to as "melted particles", "sub-severe" hailstones, "severe" hailstones, and "significantly severe" (≥ 5 cm) hailstones. The dataset also includes "giant" (≥ 10 cm) hailstones, although these account for a small sub-set of the data and thus are included (along with the significantly severe) in the "severe" category for the following analysis. Figure 5 shows the percentage of embryos initialized at each analysis time that resulted in hailstones belonging to each of the latter four categories. At every analysis time, the significantly severe hailstones account for less than 0.2% of resultant hailstones from initialized embryos. Of embryos initialized at each analysis time, only a fraction of the embryos results in hailstones (Figure 5) while the majority of embryos melt before reaching the ground. Due to the large fraction of embryos that melt ($\geq$ 95%), it is important to consider their impacts.

For the 2251 UTC analysis, only embryos that were initialized at 2251 UTC are included in the analysis. For the 23 subsequent analysis times, the trajectory analyses include embryos which were initialized at the chosen analysis time as well as all hailstones that were initialized prior to the chosen analysis time (if the trajectory has not yet been completed) at their position at the chosen analysis time. For example, the 2257 UTC analysis will include trajectories initialized at 2257 UTC at their initial position, trajectories initialized at 2254 UTC at their position 3 minutes into their lifecycle, and trajectories initialized at 2251 at their position 6 minutes into their lifecycle. These analyses provide a snapshot of all the simulated hail present in the storm at any given analysis time. The spatial integration technique over time is used in an effort to consider the changing 3-D hailstone field as the storm evolves, rather than just a selective sample of trajectories. The following results will outline features of note using examples in chronological order from the first embryo initialization time at 2251 UTC 29 May through the last embryo initialization at 0000 UTC 30 May.

As previously noted, hailstone trajectories are initialized at any point within the set embryo domain if reflectivity values of at least 20 dBZ exist at the initialization point. The melted particles are initialized at the greatest spatial expanse within the embryo domain, followed by sub-severe hailstones, and then severe hailstones. At 2251 UTC, the first analysis time where embryos are initialized, the spatial extent of embryo initialization between the melted particles and the hailstones (both sub-severe and severe) is visually apparent (Figure 6) as only hailstones at their initialization point are included. The extent within the embryo domain where initialization occurs changes as the final diameter of the hailstone at the surface changes. This relationship is consistent across all 24 analysis times (not shown). In addition to spatial extent, the location of initialization in relation to the updraft also changes as hailstone final diameter at the surface changes. Generally, the vertical velocities present at the initial positions of the melted particles are weak. Contrasting the melted particles, severe and sub-severe hailstones initialize closer to the updraft where vertical velocities are stronger. Additional early analysis times (2254 UTC and 2257 UTC) exemplify these results (Figure 7 and Figure 8). As updraft strength increases at the embryo source, the final diameter of the embryo at the surface also increases and is consistently evident at all analysis times (not shown).

As the storm and environment evolve over time, characteristics of the updraft change including shape, strength, and volume. These changes consequently impact the formation of large hail sustainability of hail production. The updraft had two distinct maxima in vertical velocity, an important characteristic of the Kingfisher, OK supercell's updraft for the maintenance of severe hail. Within the crescent shaped updraft, the two maxima are located on either tip of the crescent. The stronger, primary updraft maximum is located on the north side of the crescent and the weaker, secondary updraft maximum is located on the southeastern most extent of the crescent. The secondary region of updraft maximum differs from the primary in that it is slightly weaker and elevated. While this feature is noted in most cross-sections for all 24 analysis times, refer to 2300 UTC – 2309 (Figures 9 – 12). Vertical velocities within either maximum region are too strong for hailstones to dwell at early stages before an increase in mass, thus terminal velocity. Although, balance of velocities can be maintained along the edges of the secondary maximum, which is where the severe hailstones are located in the early portion of their lifecycle. The position of the severe hailstones is clearly shown in the early analysis times (2251 UTC – 2309 UTC) before hailstone mass increases to where higher vertical velocities are needed to keep the them aloft (Figures 6 – 12e,f). Although an in-depth comparison of the two updraft maxima characteristics was beyond the scope of this study, it is hypothesized that greater understanding of the unique characteristics of these two maxima and how they interact could reveal important controls on severe hail growth. The sub-severe hailstones resemble the positions of the severe hailstones in early analysis times being highlighted, but with greater spatial expanse. The greatest concentration of sub-severe hailstones is co-located with the severe hailstones, but sub-severe hailstones are present further from the secondary updraft maximum edges (Figures 6 – 12c,d). The melted particles represent the inverse of the sub-severe and severe hailstones, where the lowest concentration of melted particles is co-located with the highest concentrations of sub-severe and severe hailstones along the edges of the updraft (Figures 6 – 12a,b).

Melted particle concentrations are minimal within the regions where vertical velocities above 20 m $s^{-1}$ are observed, due to embryos having much smaller terminal velocities than the vertical velocities at that location and largely being lofted out of the storm's main updraft. For this reason, melted particles initialize and persist farthest from the updraft. The ubiquitous supercell bounded weak echo region (BWER) is apparent where larger vertical velocities exist, surpassing hailstone terminal velocities resulting in a region lacking relatively larger, radar-reflective hydrometeors. The melted particles can be used to identify the location of the BWER in the x-y plane due to the larger quantity of melted particles present within the storm (Figure 12a) and their high reflectivity. The BWER is apparent at all analysis times in reflectivity, but becomes distinct through the lack of melted particles in the BWER region as more embryos are introduced. At 2309 UTC, the sub-severe hailstones (Figure 12a) continue to depict the Kingfisher supercell's bounded weak echo region (BWER).

Another contributing factor for the position of severe hailstones is the horizontal winds. The region where the severe hailstones reside at 2312 UTC is within the "downshear stagnation zone" downshear of the primary updraft maximum (Figure 13e) at mid-levels (i.e., along the edge of the secondary updraft maximum). The downshear stagnation zone is where the horizontal flow moves around the updraft and horizontal flow is minimized before reconverging further downshear. It is within the downshear stagnation zone that the greatest concentration of severe hailstones is present throughout the entire 2251 – 0000 UTC analysis period. The severe hailstones that are not within the downshear stagnation zone are concentrated nearby, where horizontal winds are still weaker than they are farther from the downshear stagnation zone. While this feature is present in all analysis times, the 2312 UTC and 2315 UTC analysis times provide strong visual evidence of the severe hailstones concentrated within or near the downshear stagnation zone (Figure 13e and Figure 14e). The greatest concentration of sub-severe hailstones is also found within the downshear stagnation zone, although the latter encompass a larger area surrounding the downshear stagnation zone. The sub-severe hailstones' location relative to the downshear stagnation zone is exemplified well in the same two analysis times (Figure 13c and Figure 14c). Horizontal winds have a greater influence on the sub-severe hailstones and even greater on the melted particles than they do the severe hailstones. Smaller hailstones, with less mass and lower terminal velocities, are more likely to be transported to a different region of the storm (i.e., less conducive for growth) by the horizontal winds. As horizontal winds increase with distance from the downshear stagnation zone, the concentration of smaller hailstones increases and the concentration of larger hailstones decreases. Overall, trajectories that result in hailstones of any size prefer to spend a majority of their lifecycle within regions of the storm where horizontal winds are weakest during their growth stage.

Hailstones spend most of their residence time growing within the mid-levels, where the ground-relative horizontal flow is westerly. As the hailstones begin to gain mass, thus terminal velocity, they begin to fall to lower levels within the storm. Horizontal winds change with height, resulting in differing effects of the horizontal winds depending on size and location of the hailstone. Initially, the melted particles are advected east by westerly winds in the mid-levels (where most embryos are initialized). Melted particles initialized north of the updraft are advected anti-cyclonically within the mid-level flow around the updraft to the east side of the updraft. Melted particles initialized south of the updraft are advected cyclonically within the mid-level flow around the updraft to the east side of the updraft. Regardless of initial position, melted particles are advected eastward around the updraft in the mid-levels. The melted particles are not co-located with the prime growth region, meaning they are the first to begin their descent to lower levels since they do not experience substantial growth. East of the updraft, where the melted particles are advected, the horizontal flow becomes southerly with decreasing height. The southerly flow with decreasing height results in the advection of melted particles further north. For this reason, the highest concentration of melted particles is always located northeast of the updraft, even though melted particles are broadly initialized in many locations within the storm. To continue to show examples of these features throughout the analysis period, the highest concentration of melted particles northeast of the updraft is exemplified well at 2318 UTC (Figure 15a), though generally seen at all analysis times (Figure 6 – 29a). Both wind speeds and wind directions increase and veer with height. The southerly flow in the lower levels is much weaker than the westerly flow in the mid to upper levels. Since winds at the lower levels are weaker, it is much easier for hailstones to fall to the surface due to the difficulty maintaining the near-balance of the vertical and terminal velocities.

The sub-severe and severe hailstones are affected much differently by the horizontal winds than the melted particles, with the most significant difference being when the horizontal winds begin to influence the hailstones. The sub-severe and severe hailstones remain aloft in the mid-levels longer than the melted particles.  As severe hailstones grow, they must find higher vertical velocities to remain aloft, resulting in the severe hailstones residing closer to the updraft as residence time increases. Continuing forward in time, at 2321 UTC, the highest concentration of sub-severe hailstones is found on the northeast edge of the updraft (Figure 16c,d). Unlike the melted particles, over time the greatest concentration of sub-severe hailstones shifts from the northeast side of the updraft toward the updraft maximum on the southeast side of the updraft in the latter half of the analysis period. This shift is evident as early as 2330 UTC, as discussed in greater detail in the next section. With increasing hail masses and larger terminal velocities, the horizontal winds are increasingly less capable of advecting the severe and sub-severe hailstones east and then north, resulting in large hail increasingly being located closer to the updraft as the hailstorm intensifies.

The horizontal winds have implications on fallout positions as well. The location of the highest concentration of melted particles, sub-severe hailstones, and severe hailstones relative to the updraft at mid-levels foreshadows where the hailstones will fallout. The larger hailstones fallout closer to the updraft and the smaller hailstones fallout ranging from near the updraft to a considerable distance away from the updraft. By 2324 UTC many severe hailstones are beginning to reach the surface. At 2324 UTC, 33 minutes after the first embryos were initialized, the severe hailstones fallout position ranges from the ~1 km southwest of the updraft maximum to ~6 km northeast of the updraft maximum (Figure 17b). The sub-severe hailstones fallout from ~2 km southwest of the updraft to ~10 km northeast of the updraft (Figure 17d). The melted particles melted before reaching the surface, but they completely melt (and fall to the surface as rain) anywhere between ~3 km southwest of the updraft maximum to greater than 25 km northeast of the updraft maximum (Figure 17f). The size-sorting evident in fallout positions are due to size-sorting within the storm due to the horizontal winds. More details on hail fallout at the surface will be provided in the subsequent chapter.

With the availability of multi-Doppler radar analysis, it's possible evaluate the reflectivity values in relation to the hailstones in the storm. The fallout position of the highest concentration of melted particles is within the highest reflectivity values observed in the storm, using 2327 UTC as an example (Figure 18a,b). Both melting and wet-growth hail are understood to cause stronger radar back-scattering, and therefore higher reflectivity values. The sub-severe hailstones fallout within the larger values of reflectivity as well (Figure 18c,d). Opposite of the melted particles and sub-serve hailstones, the severe hailstones fallout where reflectivity values are minimal, along the gradient of high dBZ values and the minimal reflectivity values within in BWER (Figure 18e,f). As the storm strengthens, hailstones are going to fallout closer where the mid-level updraft maximum is located, likely directly below that. Early on in the lifecycle, sub-severe hailstones will likely fallout further away from the mid-level maximum as these hailstones have less mass, thus the vertical velocities within the updraft are not needed by the hailstone to remain aloft. As the storm strengthens and larger hailstones are supported by the storm and environment, the hailstones will gradually fallout closer to the updraft.

**4.2. Hailstone positions (2330 UTC – 0000 UTC)**

Beginning at 2330 UTC to the end of the analysis period, significant differences in the updraft characteristics are present compared to earlier analysis times. The third updraft pulse during the analysis period occurs at 2330 UTC (D16), denoted by the purple vertical velocity contours in Figure 19. Additionally, the volume of the updraft increases as the updraft mass flux increases to 1,500 kg $s^{-1}$ for the first time during the analysis period (D16). For the remainder of the analysis period, the updraft mass flux and updraft volume persistently trend toward larger values. The changes in updraft characteristics are important to note at this time as a new trajectory pathway emerges shortly after.

By 2333 UTC, embryos that will subsequently grow to sub-severe hailstones are beginning to be initialized west of the updraft core (Figure 20c,d), in contrast to hail embryos mainly to the east of the updraft core at earlier times. Sub-severe hailstones continue to initialize west of the updraft through 0000 UTC (Figures 20 – 29c,d). Severe hailstones begin to initialize west of the updraft from 2339 UTC onward through 0000 UTC (Figures 22 – 29e,f). Using the cross-sections from 2354 UTC as an example (Figure 27d,f), west of the updraft, a narrow corridor of hailstones is present within the back-sheared anvil region from upper levels to slightly warmer than freezing. These hailstones are initialized from embryos that initially descend within the back-sheared anvil in westerly middle-tropospheric flow and are subsequently ingested into the updraft region. Reflectivity values substantially greater than 20 dBZ are present at sub-freezing altitudes west of the updraft at 2354 UTC, which strongly supports this hail source region.

As described in the previous section, the region where the highest concentration of melted particles, sub-severe hailstones, and severe hailstones reside in the storm remains nearly constant throughout the analysis period. Within these higher concentrations there are multiple different trajectory pathways. As the storm continually matures and the updraft changes, new trajectory pathways emerge. In the early stages of the supercell, the most common source region is along the edges of the updraft, known as the “embryo corridor”. In the early stages, but increasingly as the storm matures, many embryos are sourced from within the updraft in the lower levels. Hailstones initialize and reside downshear (in this case east or southeast) of the updraft near the downshear stagnation zone at all 24 analysis times. The two main source regions established, while different, are both downshear of the updraft. For the purpose of the following analysis, severe hailstones in either of the two source regions downshear of the updraft will be combined and deemed the "downshear cluster." Later in the supercell's lifecycle, in its most mature stage, embryos are sourced along the rear flank of the updraft aloft, or within the back sheared anvil. Sub-severe and severe hailstones result from the upshear (in this case west or southwest) source region by 2330 UTC and 2339 UTC, respectively. Hailstones initialized from this third main source region will be deemed the "upshear cluster". While our focus was not on source regions in this study, they can provide insight to what trajectory pathways an embryo might follow. The question we aim to answer is how trajectory pathways exist upshear of the updraft region where the ingredients needed for large hail to form do not exist. To answer this question, the environmental characteristics along the trajectory pathways of hailstones sourced in the upshear and downshear clusters are compared.

Since hailstones initialized upshear did not occur until 2339 UTC, the analysis will only include severe hailstones initialized in the 2339 UTC – 0000 UTC analysis times. As time elapsed increases, the sample size decreases as some trajectories are shorter than others (hailstones with smaller residence times). Results are obtained by averaging the trajectory characteristics of every severe hailstone included in the two clusters over time. The 50$^{th}$ percentile (mean), 25$^{th}$ percentile, and 75$^{th}$ percentile were calculated for both clusters. There are 1,113 severe hailstones in the upshear cluster and 2,096 severe hailstones in the downshear cluster.

There are significant differences between the "upshear origin" and "downshear origin" severe hail trajectory clusters with respect to a range of trajectory characteristics (Figure 30). The median of the downshear cluster begins an increase in diameter shortly after initialization occurs (< 50 s), whereas the mean diameter of the upshear cluster does not begin to increase until after the first 300 s of the trajectories (Figure 30a). There is either none or minimal growth in the beginning of the trajectories of the downshear cluster, due to the absence of cloud ice and cloud water for the first ~200 s (Figure 30b,c). The upshear cluster is located west of the updraft maximum at varying levels where there is an absence of cloud water needed for growth. Meanwhile, hailstones in the downshear cluster are initialized within cloud water mixing ratios for the 25$^{th}$ and 75$^{th}$ percentiles ranging from 6 – 9 g kg$^{-1}$.

Trajectories within the upshear cluster vary with height in the first 300 s because they initialize at varying heights within the back-sheared anvil before falling to the base of the storm and ascending in to the updraft. Beginning at 200 s, there is an increase in height of the upshear cluster (Figure 30d) as these trajectories enter the mid-levels of the storm where supercooled cloud water is plentiful (Figure 30c). At the same time, vertical velocity increases (Figure 30e) as hailstones move to the updraft and terminal velocity increases as hailstones gain mass (Figure 30f).

If the first 300 s is omitted from the upshear cluster, and the upshear cluster is instead compared to the downshear cluster relative to the point where the upshear cluster enters the updraft region as the beginning of the latter trajectory, the trends during the growth phase of the two clusters are in somewhat close overall agreement. However, the evolutions of altitude, vertical air velocity, cloud water mixing ratio, size, and fallspeed as well as the final characteristics of the two clusters vary considerably. The fallout positions of the hailstones within the two clusters have notable differences due to the position the hailstones are in as growth begins.

### 4.3. Trajectories at 2339 UTC

Prior analysis of hailstone positions showed that severe hailstones are most likely found within the downshear stagnation zone. The final positions of hailstones relative to the storm core suggest that they move southeast with the storm motion and remain within the downshear stagnation zone through the majority of their lifecycle, especially the growth phase. To further understand hailstone behavior and validate prior stated results, individual trajectories must be considered.

The following analysis looks at individual trajectories of the 20 largest hailstones produced from embryos initialized at 2339 UTC. The 20 hailstones ranged in sizes from ~8 cm to ~10 cm in diameter. The DLA and radar analysis derived contours of reflectivity (colorfilled), vertical velocity (purple), graupel/hail mixing ratio (grey), and cloud water mixing ratio (green) at 2339 UTC (Figure 31; valid at the time hailstones are initialized) and 0000 UTC (Figure 32; valid 21 minutes into the trajectories lifecycle) are overlaid on the individual trajectories. The trajectories are initialized on the edge of the BWER at mid-levels within the mesocyclone. Downstream at 0000 UTC (Figure 32), just before the hailstones begin their descent to the surface, the hailstones are still located in the mid-levels, but on the western edge of the BWER, rather than the eastern edge as seen at their initialization point. To summarize, once the hailstones exit the mesocyclone, they reside in the downshear stagnation zone where there is sufficient supercooled water for growth and vertical velocities to remain aloft. The hailstones remain in this region until their terminal velocities exceed the vertical velocities (e.g., up to ~70 $m\ s^{-1}$) present in their vicinity. The location of the hailstones from beginning to just before descent shows the movement of hailstones through larger vertical velocities as they grow, while remaining in the downshear stagnation zone where the prime growth region is located.

**4.4. Residence times in supercooled cloud water and updraft**

A key question being explored throughout this study relates to hailstone locations both at the surface and aloft. It has been established that severe hailstones reside where there is a balance between vertical velocities and terminal velocities, which is found east of the updraft within the downshear stagnation zone. However, the embryos with greatest success of becoming a large hailstone are initialized near the secondary updraft maximum rather than the primary. It is hypothesized that the location of the cloud water content core coincides with where the growth of the largest hailstones resides within the storm. Due to lateral dynamic entrainment of elevated air parcels into the upshear updraft flank, larger cloud water contents are observed along the edges of the (downshear) secondary updraft maximum at mid-levels rather than being co-located with the primary updraft maximum (Figure 33). The primary updraft maximum is lacking large liquid water contents on the edge of the updraft maximum where vertical velocity is suitable for hailstones to reside.

Further investigation of the vertical velocities and supercooled water contents reveals the importance of these two variables in hail growth. It is noted that spherical hail diameter is assumed in the following discussion. The time hailstones spend within certain thresholds of vertical velocity and supercooled cloud water are compared among differing final diameters at the surface. In order to maximize sample size, trajectories from all 24 analysis times that resulted in a hailstone at the surface greater than 1 cm in diameter will be included. In the following analysis, five bins of final diameter at the surface will be used to determine if linear relationships exist between time spent in prime growth regions and final diameter at the surface. Bins from 1 cm to 11 cm in 2 cm widths are used, where the largest hailstone produced was 10.89 cm. Six threshold values of supercooled water contents and vertical velocities will be used.

The largest hailstones spent the most time in moderately large supercooled water values (Figure 34). This result is logical, since longer residence times tend to produce larger hail growth rates owing to collection of supercooled cloud water as the main source of hailstone mass. The 1 cm – 3 cm hailstones spend more time in supercooled cloud water contents $\geq 0$ g kg$^{-1}$ and $< 2$ g kg$^{-1}$ than any of the larger hailstones (Figure 34a). Time spent in supercooled cloud water contents $\geq 0$ g kg$^{-1}$ and $< 2$ g kg$^{-1}$ decreases as final diameter at the surface increases. Larger hailstones reside closer to the updraft and often are not influenced enough by the airflow patterns to be advected to regions of the storm where supercooled cloud water contents are low, thus spend more time in regions of higher supercooled cloud water contents. The time hailstones spend in supercooled cloud water contents $\geq 2$ g kg$^{-1}$ and $< 4$ g kg$^{-1}$ (Figure 34b) and $\geq 4$ g kg$^{-1}$ and $< 6$ g kg$^{-1}$ (Figure 34c), shows no significant differences between any of the final diameter bins. There are two thresholds that do reveal a significant trend: supercooled cloud water contents $\geq 6$ g kg$^{-1}$ and $< 8$ g kg$^{-1}$ (Figure 34d) and $\geq 8$ g kg$^{-1}$ and $< 10$ g kg$^{-1}$ (Figure 34e). In these two thresholds of supercooled cloud water contents, as hailstone diameter at the surface increase, the residence time in the given threshold of supercooled cloud water contents also increases. Thus, a positive linear relationship between time spent in higher supercooled cloud water contents and final hailstone diameter at the surface exists. Supercooled cloud water contents $\geq 8$ g kg$^{-1}$ and $< 10$ g kg$^{-1}$ most noticeably displays the linear trend. The median values of time spent in supercooled cloud water contents $\geq 8$ g kg$^{-1}$ and $< 10$ g kg$^{-1}$ are 114 s, 142 s, 186 s, 314 s, and 481.5 s for the five final diameter bins, increasing from smallest hailstone to largest hailstone. The last supercooled cloud water contents threshold analyzed is $\geq 10$ g kg$^{-1}$ (Figure

34f), which does not show the same trend with significance. The absence of the linear trend in the final threshold category is likely due to the limited number of hailstones that encounter supercooled water contents of such a high value.

The largest hailstones also spent the most time in moderately large updrafts (Figure 35). The smallest hailstones have the largest residence time within vertical velocities $\geq 0$ m $s^{-1}$ and < 10 m $s^{-1}$ (Figure 35a). As hailstones increase in diameter at the surface, the time spent within vertical velocities $\geq 0$ m $s^{-1}$ and < 10 m $s^{-1}$ decreases. For vertical velocities $\geq 10$ m $s^{-1}$ and < 20 m $s^{-1}$ (Figure 35b) and vertical velocities $\geq 20$ m $s^{-1}$ and < 30 m $s^{-1}$ (Figure 35c) there is little significance in the time spent between the final diameter bins. For time spent in vertical velocities $\geq 30$ m $s^{-1}$ and < 40 m $s^{-1}$ there is a significant difference for the first four final diameter bins, but the last (9 – 11 cm) is an outlier (Figure 35c). The median of the 9 – 11 cm bin falls between that of the 3 cm – 5 cm bin. The 9 – 11 cm bin being an outlier is likely due to the terminal velocity of the hailstones in this bin being greater than 30 m $s^{-1}$ – 40 m $s^{-1}$, so these hailstones must reside in regions of higher vertical velocities to stay aloft. Vertical velocities that are sufficient to sustain a hailstone of 9 cm – 11 cm, so $\geq 40$ m $s^{-1}$ and < 50 m $s^{-1}$ (Figure 35d) as well as $\geq 50$ m $s^{-1}$ (Figure 35e) yield a significant linear relationship between residence time in vertical velocities and hailstone diameter at the surface. As residence time in those regions of moderate updraft increases, the diameter of the hailstone at the surface increases. Therefore, a positive linear relationship between moderate vertical velocities and increasing hailstone size at the surface exists.

### 4.5. Residence times

The total hailstone residence time aloft in the storm is considered within each size category (i.e., sub-severe, severe, significantly severe, and giant) at all analysis times (Figure

36). As in section 4.3, it is again noted that spherical hail diameter is assumed in the following discussion. Both the mean and median residence time for all hailstones within each size category at each analysis time are considered. There is only one giant hailstone (i.e., based on spherical diameter), which initialized at 2339 UTC, making the giant hailstone category too small of a sample size to draw any conclusions from. The mean and median residence time increases as hailstone size category increases at all but two analysis times (2327 UTC and 0000 UTC). Significant changes in updraft characteristics are apparent around 2327 UTC, as noted in previous sections. The hailstones initialized at 2327 UTC have the longest residence time of sub-severe hailstones, but much shorter residence times for significantly severe hailstones.

Relative minima in residence time are present in each size category for hailstones initialized ~3 minutes after the updraft pulsed upward. Hailstones in the early analysis times generally have longer residence times than those at later analysis times when the storm is stronger and more mature. These results are consistent with the hypothesis that when the updraft is stronger, hailstones do not need long residence times to grow large. A correlation between depth of strong, surface-based updraft and cloud water content could likely explain the result that residence time needed to grow to similar sizes decreases as updraft strength increases.

# Chapter 5: Surface Hail

An objective of the NSF-PREEVENTS grant that funded this study was to "validate a microphysically complex hail trajectory model in light of newly available time-varying radar-retrieved wind and buoyancy field and surface hail observations". Using the IBHS hailstones and LSRs, we can explore how well they match our simulated hailstones in both hailstone fall positions and physical characteristics. With 4-D simulated hail trajectories from an observed storm, the ability to compare independent surface hail observations to realistic simulated hailfall is a unique aspect of the present study.

## 5.1. Hail swaths

Hailstone trajectories are terminated when they either melt entirely or reach the surface. Since hailstone fall speeds vary depending on hailstone mass and density, the model produces fall speeds of up to 70-75 m $s^{-1}$ for the largest simulated hailstones. As in prior sections, it is again noted that spherical hail diameter is assumed in the following discussion. Any hailstone within the lowest 75 m at the last second of their trajectory are assumed to be at the surface. Hailstones from 2251 UTC – 0000 UTC at the surface, regardless of final diameter, are used to produce simulated hail swaths.

The number of hailstones in a 250 m × 250 m grid cell over the entire domain is shown in Figure 37 to illustrate the spatial density of hail at the surface. There are two large areas of the hail swath where relatively higher concentrations of greater than 30 hailstones per grid cell are found. The first higher concentration occurs at the beginning of the hail swath and contains an area of grid cells containing greater than 60 hailstones. The first higher concentration is further inward of the hail swath, closer to the NE edge of the hail swath. The second higher concentration occurs later in the hail swath, co-located and south of where the updraft is located at 2348 UTC. The second higher concentration is located closer to the SW extent of the updraft but extends as far NE in the hail swath as the first higher concentration does. The area between the two higher concentrations occurs between where the updraft is located at 2330 UTC and 2348 UTC.

The maximum ice core diameter of the modeled spherical hailstones at the surface is presented in Figure 38. The hail swath illustrates where the largest hailstones fell considering the entire hail swath. There are size-sorting effects taking place within the hail swath, but the size sorting effects evolve in the downstream direction within the hail swath. Around the beginning of the hail swath, hailstones with diameters ≥ 3 cm are located along the southwest edge of the hail swath (although slightly downstream of the updraft core), while slightly smaller hailstones are located farther to the northeast. The detailed hailstone placement relative to the updraft core in the early hailswath is almost certainly a transient effect of the discrete introduction of the first embryos beginning at 2251 UTC that subsequently require up to ~ 20 minutes to grow and reach the surface.  Farther downstream and later in time between the main updraft locations at 2330 UTC and 2348 UTC within the hail swath, the local maximum concentration of the largest hailstones are again located on the far southwestern extent of the updraft. Farther downstream and later in time around the main updraft locations at 0000 UTC within the hail swath, where the second local maximum concentration is located, maximum spherical hail diameters ≤ 2 cm are located on the southwest edge of the hail swath and the larger hailstones are found farther northeast into the hail swath.

**5.2. Hailstone observations**

Since the simulated hailstones are being generated in an observed storm, hail observations can be used to validate the size and position of the simulated hailstones. The IBHS hailstones were picked up from the ground and analyzed in the town of Kingfisher, OK during the period 0057 – 0105 UTC. Results to be discussed in sections 5.3 and 6.5 will reveal that simulated hail fell until 0027 UTC, a transient effect of the last embryos being introduced at 0000 UTC combined with the up to ~ 20 minutes or more required for hail growth and fallout. Hence, the IBHS ground hail sample was obtained about 30 minutes after the final simulated hailstones fell to the surface. However, via a single-radar analysis of WSR-88D radar KTLX observations employing methods described in section 2.5, it was determined that strong reflectivities reached Kingfisher beginning at roughly ~ 0045 UTC. Hence, the IBHS ground hail sampling likely commenced up to ~ 10 minutes after hail initially began falling in Kingfisher. As will also be shown in the later sections, the IBHS hail sample was also located downstream with respect to the storm motion from the final simulated hail position. Due to the latter space-time discrepancy, the IBHS hailstones can only be used indirectly to qualitatively validate the simulated hailstone's sizes and positions. All LSRs associated with the Kingfisher supercell while moving through the counties of Blaine and Kingfisher, OK were used. In the comparisons of the modeled hail swath to individual LSRs, it must be noted that both the LSR locations and times likely contained variable but unknown errors. In addition, it is unknown whether the LSR data pertain to maximum or averaged hail dimension, as well as whether the hail size was measured or merely qualitatively estimated. Finally, surface temperatures were nearing 32 °C, thus implying that significant melting could occur before hailstones could be measured and reported. In total, there were 12 available LSRs meeting the location criteria along the Kingfisher storm's track. Only 4 LSRs are co-located with the simulated hail swath and 2 are located downstream of the hail swath, in addition to the IBHS collection site (Table 2).

The maximum spherical hail diameter of the simulated hail swath is examined in the context of geographical features and LSR locations and reported hail sizes (Figure 39). Of the LSRs that met the criteria, only LSRs 1, 2, 3, and 4 overlapped with the simulated hail swath. LSR 1 is a 3.8 cm hailstone. Simulated spherical hailstones up to 7 cm occur in the immediate area of LSR 1. LSR 2 is a 7 cm hailstone, though the largest simulated spherical hailstone near LSR 2 is 3 cm. LSR 3 is a 5 cm hailstone, with simulated hailstones up to 4 cm in the immediate vicinity of the LSR. LSR 4 is a 3.8 cm hailstone, with simulated hailstones up to 3 cm in the immediate vicinity. Based on LSR 1, the simulated hail swath is reasonable near the observation. The observed hailstones are larger than our simulated hailstones at 3 of the 4 LSR locations (namely LSRs 2-4), which is inconsistent with both the radar-observed reflectivity core swath location and the modeled hail swath (which in turn has been derived from the radar-analyzed storm evolution). It is important to note that, in contrast to the LSR locations, the IBHS hail sample was also located precisely downstream with respect to the storm motion from the maximum-diameter hail swath core on the inflow flank of the Kingfisher storm from 0000 UTC onward.

**5.3. Timing of hailfall**

Understanding the temporal characteristics of the hailfall is important to understanding the previously described spatial characteristics of the hailfall (Figure 40). Hailstones that made it to the surface, regardless of final diameter at the surface, were included in the following analysis (following the methods of the hail swaths). The first hailstone made it to the surface between 2300 – 2303 UTC and the last hailstone between 0024 – 0027 UTC (Figure 40). The earlier times have less hailstones due to less embryos simulated prior to that time compared to the later times. A greater number of embryos are initialized going forward in time, thus the increase in number of hailstones falling to the surface at later times. Despite the number of embryos, it is apparent that larger hailstones fall out predominantly after 2330 UTC under the influence of significant changes in the strength, volume, and shape of the updraft (Figure 1). Between 2339 – 2342 UTC there is a relative minimum in the number of hailstones falling out of the storm, suggesting a feature of the storm or environment to be the cause. After 0000 UTC, beyond our analysis period, surface hailfall frequencies decline as the largest hailstones (≥ 8 cm) begin to fall out of the storm.

The surface arrival time reveals temporal characteristics of the hailfall within a spatial hail swath context (Figure 41). Features of note include the relative lack of hailstones in the hail swath that fell out between 2339 – 2342 UTC, as seen in Figure 40 as well. Between 2342 UTC – 2348 UTC, the hail swath extends to the northwest further than in any other part of the hail swath. Between 2348 UTC – 0000 UTC, the northwesterly hail swath extension is smaller than at any other portions of the hail swath.

**5.4. Surface Hailstone Counts**

Results show there is time-varying size sorting occurring along the hail swath. To further investigate, a 3 km × 3 km subdomain was chosen and hailstones that fell within the subdomain between a chosen time period were counted. The subdomain size was chosen to provide adequately high particle concentrations to resolve the averaged particle size count distribution (Waugh et al. 2018). As shown in Figure 42, the domain chosen was from 52 km – 55 km in east-west position (x) and 12 km – 15 km in north-south (y) position for hailstones that fell to the surface between 0015 UTC – 0030 UTC. Hail formed from embryos initialized at any analysis time were included, as long as they reached the surface as a hailstone between 0015 UTC – 0030 UTC. The Control ASZ16-HAILCAST hail growth physics were used for the following analysis.

The particle size count histogram (Figure 42a) approximates a Gamma function distribution of diameter of all the hailstones that fell to the surface within the subdomain (black box in Figure 42b) and the noted time period. This result is consistent with Z83, who sampled hailstones immediately downshear of the main updraft, and also obtained a Gamma function distribution fit of their collected hailstones. Similar again to Z83, there is a steep drop off in hailstone count below 1 cm. The lack of hailstones below 1 cm is hypothesized to be attributed to a combination of size sorting, melting resulting in the depletion of the smaller particles present, and slower-falling particles which increases melting residence time. Contrary to Z83, the peak in the hailstone counts is between 3.0 cm – 3.5 cm, whereas Z83 observed a peak at ~2 cm. The difference in peaks could be attributed to a multitude of factors, including exact collection location, storm mode, and overall range in hailstone sizes produced by the specific storm. In future work, both smaller and differing subdomains can be generated over differing time periods to compare how the distribution of hailstone particle size distributions change as the updraft and storm evolve.

# Chapter 6: Sensitivity Tests

Sensitivity tests were conducted in order to validate the ASZ16-HAILCAST growth physics in light of more realistic microphysical storm characteristics. While the IBHS hailstones were not able to be used to validate the positions and size of the simulated hailstones, we can infer information from their visual characteristics. The IBHS hailstone samples visually reveal evidence of dry growth (i.e., opaque ice) in all the hail samples, with many evidencing large amounts of dry growth (Figure 43). The pictured hailstones also show that they are generally spheroidal rather than spherical, as assumed for the above results of the present study as well as prior hail growth studies (Chapter 1). In order to assess the validity of the ASZ16 hail growth physics module (referred to as the Control or "CNTL" model), the following three sensitivity tests have been conducted.

### 6.1. Oblateness effects with increased heat transfer

The transfer of heat between the hailstone and the ambient air is not well understood, as it is not a process that can be observed in nature and there are limited laboratory experiments aimed at measuring this process. Heat transfer is important for both growth and melting, and $\chi$ is seen in both of those calculations. To evaluate the sensitivity of the transfer of heat away from the hailstone, $\chi$ has been modified following the methods for oblate spheroidal hailstones as described in Section 3.2. $\chi$ is present in the calculation of $T_s$ (Eq. 10) and $F_w$ (Eq. 11) through $\overline{f_H}$, which controls the transfer of heat away from the hailstone to the ambient air during dry growth and wet growth, respectively. As Re increases, $\chi$ decreases, and the amount of heat transferred away from the hailstone to the ambient air increases. In the following sensitivity test, hailstones are assumed to be oblate spheroids, and the value of $\chi$ is parameterized to better represent the physical processes occurring for oblate hailstones. We hypothesis that oblate spheroidal hailstones will have the following impacts on hail growth: (1) greater efficiency at collecting supercooled cloud water due to an increased horizontal surface area and sweep out volume; (2) greater efficiency at dissipating fusion heat release from the ice surface into the ambient environment; and (3) larger sizes but smaller fallspeeds for given sizes, yielding important changes in hail trajectories. The oblate spheroidal hail growth sensitivity test is referred to as the Shape or "SHAP" test.

**6.2. Ice collection efficiency**

Ice collection efficiencies of hailstones are generally unknown. A lack of understanding of the fraction of water surrounding the hailstone (Pruppacher and Klett 1997) contributes to the uncertainty of how efficiently hailstones collect ice. Due to the uncertainties, ice collection efficiencies must be parameterized based on knowledge of aggregation of ice for snow particles and the understanding of ice crystal surfaces. Generally, as hailstone temperature decreases, the ice collection efficiency is believed to decreases since a water shell or quasi-liquid layer is less likely to exist. Ice sticking to ice is less likely physically than ice sticking to water. In the following sensitivity test, $E_{cx}$ follows that of KL20 as described in Section 3.4. Since ice collection is not the main driver of hail growth and an inefficient collection process based on prior knowledge, it is hypothesized that this test will demonstrate rather weak sensitivity to treatment of ice collection efficiency. The ice collection efficiency hail growth sensitivity test is referred to as the "EICE" test.

**6.3. Shedding threshold**

In order for a hailstone to transition from wet growth to dry growth, the surface of the hailstone must be completely frozen, or absent of liquid water. List (1959, 1960a,b) and Macklin (1961) determined that little to no shedding takes place while in the wet growth regime. While shedding is limited, a liquid water present on the surface of the hailstone does exist while in wet growth, therefore cannot be discounted. In the ASZ16-HAILCAST growth physics used in our simulations, $M_{wcrit}$ remains a constant as stated in Section 3.3. Chong and Chen (1974) stated that particles greater than 1 cm in diameter would be unable to maintain a liquid water layer, thus shedding would occur for hailstones 1 cm or larger. Heymsfield et al. (1987) took a similar approach to limiting shedding based on diameter, where after the hailstones reaches 9 mm, shedding occurs. RH87a adjusted their equation based on the work of Rasmussen et al. (1984b), which observed much more liquid water present on the surface of a given hailstone. The following sensitivity test will use the $M_{wcrit}$ from RH87a as described in Section 3.3. We hypothesize the $M_{wcrit}$ from RH87a will result in smaller hailstones, as they are less likely to shed their water shell and go through efficient growth as easily. The following results will explore what effects the additional $F_w$ stored on the hailstone has. Since previous studies have stated shedding is not a significant process, we not do expect a strong sensitivity to changes in the shedding threshold. The shedding threshold hail growth sensitivity test is referred to as the "SHED" test.

### 6.4. Sensitivity tests results

The three previously described modifications are compared to the control using hailstones initialized at 2339 UTC and will be referred to as the shape test (SHAP), ice collection efficiency test (EICE), and the shedding threshold test (SHED). The following results note differences in bulk hail growth and the characteristics along the trajectories between the CNTL model run and the SHAP, EICE, and SHED sensitivity tests.

The differences in hailstone counts for embryos initialized at 2339 UTC were compared between the CNTL run and the SHAP, EICE, and SHED tests (Figure 44). The CNTL run

(Figure 44a) is most similar to EICE (Figure 44c). The EICE run produced only 10 fewer hailstones (n=3511) than the control (n=3521), with no noticeable differences in the distribution of hailstones sizes. The SHAP run (Figure 44b) produced significantly more hailstones (n=8210) than the CNTL, EICE, or SHED runs. The SHAP run produced more hailstones generally across all hailstone sizes. However for the largest hailstones (≥ 6 cm), the CNTL and EICE runs produced very slightly more hailstones than the SHAP run. The SHED run produced the least number of total hailstones (n=2893) (Figure 44). To further explore why the differences in bulk hail production exist, characteristics of the hailstone and environment along the trajectory are analyzed, following the methods described in section 4.2.

The oblate spheroidal hailstones differ greatly in their characteristics along the trajectories compared to the other three sensitivity tests (Figure 45). It was hypothesized that the increase in sweep out volume for an oblate hailstone would increase the amount of supercooled water collected. Figure 45a shows how much mass is added during each time step due to collection of supercooled cloud water, where the shape test results in greater increase in mass due to collection of supercooled water than the other tests. Between 1250 s and 1400 s, the median mass increase due to collection of supercooled water is greater than the 75$^{th}$ percentile of the control (and any other test). The heights (Figure 45b), ambient temperatures (Figure 45c), and cloud water mixing ratios (Figure 45d) along the trajectories explain why there might be an increase in supercooled water between 1250 s and 1400 s. At 1250 s, the hailstones in the shape test experience an increase in height, followed by a decrease in ambient temperature and increase in cloud water mixing ratios. Additionally, in height the shape test (Figure 45b) results in hailstones moving to higher heights initially, but they fall to lower levels quicker. Overall, the shape test hailstones have shorter residence times though it does not negatively impact final hailstone diameters (Figure 45e). Shorter residence times are due to greater hailstone mass, leading to a quicker increase in terminal velocities. Although terminal velocities increase at a faster rate, increased collection of supercooled water offsets the shorter residence times.

Overall, the SHAP run differs from CNTL in the former's "wavy" pattern in height. Due to this pattern in height, other variables follow, as an increase in height would result in more favorable conditions for growth as trajectories traverse the mid-levels of the storm (i.e., the prime growth region). Recall, there is more than one trajectory pathway that is present at 2339 UTC, meaning some of this "wavy" pattern could be a result of the pathway from the upshear cluster. To assure this is not the case, the same analysis was completed at 2330 UTC before the upshear pathway emerged, though not shown. The 2330 UTC revealed a wavy pattern in the shape test as well.

The EICE run differs the least from CNTL of all the sensitivity tests. Most variables in CNTL and EICE are almost undistinguishable. The severe hailstones at 2339 remain in ambient temperatures warmer than -40 °C, but cloud ice is found in its highest concentrations at ambient temperatures colder than -40 °C, meaning the hailstones in the Kingfisher, OK supercell do not encounter much cloud ice. Due to the lack of cloud ice encountered, it is reasonable that the ice collection efficiency test does not show sensitivity. The modified ice collection efficiency should represent a more physical parametrization of ice collection efficiency, such as that of KL20, as described in Section 3.4.

The SHED run produced significantly fewer hailstones, although only the $F_w$ time series difffered significantly from CNTL (Figure 45f). Early in the trajectory, the median $F_w$ is over 0.1 in the first ~50 s. In sharp contrast, the $F_w$ from CNTL is essentially zero. The increase in $F_w$ is only apparent in the early portion of the trajectories, since the shedding threshold decreases after hailstones grow larger than 9 mm diameter,. With the addition of a larger $F_w$, both the overall mass and fallspeed of the hailstone would increase. Since fallspeed is increased, the median height of the SHED hailstones (Figure 45b) tends to be somewhat less than the CNTL hailstone heights throughout most of the trajectory lifecycle. The exception of relative SHED and CNTL heights occurs both between ~200 – 400 s and at the end of the trajectory lifecycle, the latter being less consequential since hailstone fallout depletes the sample size. Since the SHED test results in hailstones residing at lower heights on average, residence time in the prime growth region (i.e., the mid-levels) where there are larger cloud water mixing ratios (Figure 45d) is limited.

### 6.5. Oblateness effects with increased heat transfer results

Due to the significant demonstrated sensitivity of the oblate spheroidal hailstones via their increased heat transfer, trajectories initialized at all 24 analysis times were generated for the SHAP run to enable direct comparisons with CNTL spanning the full analysis time period. To compare spherical hailstones to the oblate spheroidal hailstones, the hail swath analyses were repeated for the oblate spheroidal hailstones. The resulting oblate spheroidal hail swaths shown below are compared to the spherical hail swaths presented in Chapter 5.

Overall, the biggest difference between the spherical hailstones and the oblate hailstones is the total number of hailstones produced. While this feature was noted at 2339 UTC in the prior section, it is evident in the hail swaths over all analysis times. In Figure 46, showing concentration of oblate hailstones at the ground in a 250 m × 250 m grid cell, the oblate hailstones show the same trends shown in the spherical hailstones (Figure 37). The differences are due to significantly more hailstones present in the oblate swath, resulting in a smoother, more uniform look to the hail swath. Similarly, the hail swath of maximum hailstone ice diameter at the surface for oblate hailstones (Figure 47) resembles that of spherical hailstones (Figure 38) with significantly more hailstones. Just as the higher concentration hail swath, the maximum ice diameter hail swath for oblate hailstones shows the same trends as the spherical hailstones, but with a more uniform appearance.

The maximum $D_{eq}$ simulated hail swath overlaid with geographical features and the LSRs for oblate hailstones is shown in Figure 48. The LSRs used are the same described in Chapter 5 for the spherical hailstones, seen in Figure 39. LSR 1 is a 3.8 cm hailstone with up to 8 cm hailstones in the vicinity. LSR 2 is a 7 cm hailstone with the largest simulated hailstone near LSR 2 being just 4 cm. LSR 3 is a 5 cm hailstone, with simulated hailstones up to 5 cm in the immediate vicinity of the LSR. LSR 4 is a 3.8 cm hailstone, with simulated hailstones up to 3 cm in the immediate vicinity.

As stated in Chapter 3, $D_{\mathrm{max}} = aD_{\mathrm{eq}}$ (S21), therefore, the same hail swath can be produced using $D_{max}$ rather than $D_{eq}$. Using $D_{max}$, the largest hailstone produced is 15.23 cm rather than 10.896 cm for the largest $D_{eq}$ for the oblate hailstones. Hailstones ≥ 15 cm are defined as "gargantuan" by Kumjian et al. (2020). Figure 49 shows the same hail swath as shown in Figure 48, but using $D_{max}$. Comparing to the same LSRs, LSR 1 is now in the vicinity of near 12 cm hailstones rather than 8 cm. LSR 2 has hailstones of 6 cm near, which is still 1 cm shy of what was observed. LSR 3 has up to 8 cm hailstones in the vicinity, 1 cm larger than what was observed. LSR 4 has 4 cm hailstones in the vicinity, which is 0.2 cm larger than the observation. The timing of the hail fall shows minimal differences between oblate hailstones (Figure 50) and spherical hailstones (Figure 40), as the trends observed for spherical hailstones is the same for the oblate hailstones. The biggest difference is the apparent smaller residence time for oblate hailstones compared to the spherical hailstones, as noted in prior results. The first spherical hailstone to arrive at the surface occurs between 2257 UTC – 2300 UTC, rather than between 2300 UTC – 2303 UTC for the oblate hailstones despite shorter residence times on average. The greatest number of hailstones fall to the surface between 0000 UTC – 0003 UTC for spherical hailstones and between 0003 UTC – 0006 UTC for the oblate hailstones. The other relative peaks for oblate hailstones occur at a 3-minute lag compared to the spherical hailstones. The hail swath showing arrival time of hailstone at the surface for oblate hailstones (Figure 51) differs from the spherical hailstones (Figure 41) in the same ways mentioned previously, primarily the number of hailstones in the swath.

# Chapter 7: Discussion

The objective of our study, with a novel hail trajectory dataset, is to identify where and why hailstones of varying sizes grow within the storm and fall to the surface. The previously presented results address hail locations as the storm and environment evolve through the analysis period. In the following discussion, the evolution of hailstone trajectories from initialization to surface occurrence is described to address why large hail develops via new hypotheses and prior works.

Many of the embryos that result in hailstones are sourced along the secondary updraft maximum and spend a majority of their growth period within the secondary updraft maximum. As an embryo's distance from the updraft increases, final diameter at the surface decreases. A larger region of moderate vertical velocities (or wider updraft) is favorable for hail growth (Foote 1984; Nelson 1983; Ziegler et al. 1983; Picca and Ryzhkov 2012; Kumjian et al. 2021) because it would enlarge the embryo source region (Dennis and Kumjian 2017); thus, more hailstones could be realized. Past literature has not talked about the impact multiple updrafts might have on hailstone production. In the Kingfisher, OK supercell, while there is one updraft, there are two distinct maxima present within the updraft. The sub-severe and severe hailstones reside for the majority of their growth phase on the edges and within the secondary maximum rather than the primary maximum. Within the secondary maximum, higher supercooled water contents in the mid-levels and moderate vertical velocities (30 – 50 m $s^{-1}$) are present, the ideal conditions for hailstone growth. Future work should consider maxima within the updraft, a new developing updraft, as well as updrafts from cell mergers to understand how these additional regions of updraft or moderate vertical velocities could impact hail growth.

In a study of the microphysics of the Kingfisher, OK supercell, D16 notes the minimum reflectivity associated with the BWER was shifted east of the "region of strong diverging flow around the midlevel core of the largest updraft speeds." The region described in D16 is the known as the downshear stagnation zone. The downshear stagnation zone is confined to a small region within the storm. Within the downshear stagnation zone, hailstones are minimally impacted by the horizontal winds. The downshear stagnation zone is created due to the flow of hailstones around the updraft. We theorize the shape of the updraft plays a critical role in the hail growth zone (as well as fallout position). Theoretically, if the updraft is elongated parallel to the mid-level flow, the downshear stagnation zone downshear of the updraft will be smaller, as the horizontal flow will reconverge closer to the downshear extent of the updraft. If the updraft is elongated perpendicular to the mid-level flow, the downshear stagnation zone downshear of the updraft will be larger, as the horizontal flow will reconverge further away from the downshear extent of the updraft. Updraft shape (specifically aspect ratio in relation to the mid-level flow) rather than simply an assumed circular updraft with equivalent radius, could reveal details about hail growth within the storm and surface occurrence of hailstones. Future work should explore the effects updrafts of varying shapes have on hail growth as well as additional storm dynamics. The BWER throughout time is co-located with the region where the largest hailstones are located and where melted particles are at their lowest concentrations. Based on our knowledge of hailstone's preference to the downshear stagnation zone, the BWER could have implications on forecasting where the hail growth zone is located in real time since we are unable to measure supercooled cloud water and precise vertical velocities in real time.

As the storm strengthened after 2330 UTC, a new trajectory pathway appeared, indicating the strength of the updraft could have implications on how many pathways are open for hailstones to traverse. Since the analysis only goes through 0000 UTC, we are unable to determine if the new pathway steadily produces an increasing number of severe hailstones. The overall number of hailstones produced increased after 2339 UTC once the new pathway appeared. Hailstones from both the upshear and downshear cluster grow from the same mechanisms, with the one apparent difference being the overall residence time. While the residence time differed, the residence time spent in the growth phase did not. There may be many trajectory pathways, possibly others within the upshear and downshear cluster identified within this study. Our results focused on where all hailstones were present within the storm, rather than individual trajectories.

We hypothesize the shape of updrafts throughout time are cause the of resultant positions of the higher concentrations of hailstones at the surface as well. As the updraft evolves over time, the surface positions and patterns of larger hailstones also changes. The updraft strength and rotation of the mesocyclone may hold clues as to why the size-sorting effects differ throughout the hail swath. Larger hailstones have more mass, therefore must reside within higher vertical velocities to stay aloft. As hailstones grow larger, they are found closer to the updraft. The storm must have varying vertical velocities needed to maintain the balance hailstones with varying masses. Differing vertical velocities needed to remain aloft in the mid-levels within the growth zone for differing hailstones leads to size-sorting within the storm prior to reaching the surface (Ryzhkov et al. 2005; Kumjian and Ryzhkov 2008, 2012; Dawson et al. 2014). Size-sorting within the storm leads to size sorting effects evident at the surface.

Since the hailstones are assumed to be spherical, we are likely underestimating the maximum hailstone size in the spherical simulated hail swath. English (1973) notes that oblateness results in enhanced growth which leads to underestimation of diameter. Hailstones could be up to 20% larger whenever oblateness is accounted for (Shedd et al. 2021). In the oblate hail swaths, the hailstones are larger and better match the LSRs. While our sample is too small and LSRs have too many limitations to conclude with confidence our simulated hail swath for oblate hailstones is representative of the actual hail swath produced on 29 – 30 May from the Kingfisher, OK supercell, the observations add confidence to the truthfulness of the simulated oblate hail swaths. Additionally, while 200,000+ hailstones are included in the hail swath, in the real world a supercell would be producing significantly more hailstones than produced in this study.

Our results give us a realistic representation of maximum hail size at the surface. The most widely used tool to simulate hail swaths include MESH, which is best used to determine if hail is present within the storm rather than its precise fallout location (Ortega 2018; Murillo and Homeyer 2019). In a study of hail swaths using the HailTrack model Brook et al. (2021) stated, "most attempts at comparing radar measurements directly to hail observations at ground level introduce two implicit assumptions: 1) hailstone sizes remain constant from detection aloft until impact, and 2) hailstones land directly below where they are detected aloft." Models such as HailTrack and HAILCAST are not able to be used operationally in real time yet due to computational time demands. Until that is feasible, understanding the differences in MESH and hail swaths such as the ones shown in our study and Brook et al. (2021) could lead to further understanding of the inaccuracies that arise from products such as MESH.

# Chapter 8: Conclusions

The overarching questions concerning how, when, and where hailstones grow and fall to ground, as well as the physical characteristics of observed surface hail, have each been addressed in the present thesis. Through the use of 4-D hailstone trajectories simulated in a radar-observed storm, the present hail trajectory dataset introduces rather uniquely important time varying information. Using true 4-D environmental and hailstone variables, trajectories and their respective surface fallout locations reveal distinguishing factors between different sized hailstones. Using radar analyses, DLA retrievals, and a proven hail trajectory model, a novel dataset of hail trajectories was created using observations from the 29 – 30 May 2012 Kingfisher, OK supercell. The combination of hail trajectories and in-situ surface hail observations facilitated a comparison of the two datasets. While there were limitations in comparing two different types of data, questions arose which led to discoveries that are expected to improve the hail growth trajectory model. Although the present study is limited to only a single supercell storm case in relation to the Kingfisher supercell's environment, robust conclusions about supercell hail growth have been gleaned from our large sample size of greater than 2.7 million simulated trajectories.

A detailed hail trajectory analysis has delineated where hailstones of differing sizes are able to grow. Hailstones positions throughout the storm, individual trajectories, and characteristics along these trajectories have led to the following main findings:

- Larger hailstones initialize from embryos sourced closer to the updraft. As distance from the updraft increases, embryos are less likely to result in a hailstone.
- Hailstones are more likely to reside in the secondary updraft maximum rather than the primary updraft maximum.

- Hailstones spend most of their growth stage within the downshear stagnation zone where they are minimally impact by the horizontal winds.
- Horizontal winds cause size-sorting to take place within the storm which results in size-sorting at the surface.
- The surface occurrence of numerically simulated severe hail is favored over non-severe hail by significantly longer residence times in 30-50 m/s updrafts and supercooled cloud water contents exceeding 5 g/kg.
- Later in the lifecycle, as the storm intensifies and matures, severe hailstones are sourced from the edge of the backsheared anvil upshear from the main updraft.
- Although hail size is actually defined according to maximum dimension thresholds (Kumjian et al. 2020), the assumed-spherical hailstone trajectory calculations in the present thesis nevertheless produce significant amounts of severe hail including "significantly severe" (≥ 5 cm) hailstones and at least one "giant" (≥ 10 cm) hailstone. The oblate spheroidal hail trajectory calculations produce at least one "gargantuan" (≥ 15 cm) hailstone (Kumjian et al. 2020) as well as greater numbers of significantly severe and giant hailstones relative to the spherical hail trajectory calculations. The gargantuan oblate spheroidal hail production in the present thesis is the first example to the author's knowledge of gargantuan hail trajectory calculations in a radar-observed storm.

Hailstorms receive attention whenever they impact humans, mostly through destruction of surface property and agriculture. An analysis of where and why hailstones form and fall to ground has revealed important aspects of surface hailfall. Simulated hail swaths provide spatio-temporal understanding of hail sizes and concentrations at the surface. An analysis of surface hail observations from the IBHS team and local storm reports compared to the modeled hailfall results have led to the following main findings:

- The characteristics of the updraft such as shape, width, maximum strength, and volume impact the appearance of the hail swath.
- The size-sorting effects evidenced in the numerically modeled hail swath are variable in time.

The value of conducting targeted sensitivity tests was revealed by comparison of the in-situ surface hail observations to the hail trajectory model output. These sensitivity tests address an important sub-objective of the thesis, namely to identify potential improvements of the ASZ16-HAILCAST hail growth physics model. The results of the hail growth model sensitivity tests have led to the following main findings:

- The current ice collection efficiency shows no sensitivity. Due to simplicity and physical understanding, we recommend using the Kumjian and Lombardo (2020) method of calculating ice collection efficiency in future uses of the ASZ16-HAILCAST model.
- The shedding threshold resulted in less hailstones than the Control run. While there are many unknowns still regarding water shells on hailstones, a 4 mm water shell would not be a common physical occurrence. For this reason, we suggest the shredding threshold remain as it is in the ASZ16-HAILCAST control physics.
- Allowing oblate spheroidal hailstones via modified heat transfer within the hail growth physics results in significantly more hailstones than in the case where hailstones are assumed to be spherical. The oblate spheroidal hail swaths are more

physically realistic than the Control run. The oblate spheroidal option in the ASZ16-HAILCAST should be used instead of the spherical hailstone assumption.

This thesis has aimed to confirm conventional hail growth models through a uniquely realistic and detailed dataset composed of a state-of-art hail growth trajectory model, comprehensive 4-D multi-radar airflow and retrieved thermal-microphysical fields, and a comparison between modeled hail and independent in situ hail collections in an observed supercell storm. Combining these elements has facilitated an improved process understanding of hail growth, particularly of severe and large hail growth. Additional complementing studies that incorporate storm cases from differing regions and storm environments are needed to further improve understanding of the dominant modulating controls on hail growth. There is also a significant potential role for combining in-situ hail observations of unprecedented detail, with hail growth trajectory modeling, to further advance process understanding of hail growth and its societal impact and helping forecasters develop further improvements of operational hail prediction.

# References


Adams-Selin, R., and C. L. Ziegler, 2016: Forecasting hail using a one-dimensional hail growth model within WRF. *Mon. Wea. Rev*., **144**, 4919–4939, https://doi.org/10.1175/MWR-D-16-0027.1.

Adams-Selin, R. D., A. J. Clark, C. J. Melick, S. R. Dembek, I. L. Jirak, and C. L. Ziegler, 2019: Evolution of WRF-HAILCAST during the 2014–16 NOAA/Hazardous Weather Testbed Spring Forecasting Experiments. *Wea. Forecasting*, **34**, 61–79, https://doi.org/10.1175/WAF-D-18-0024.1.

Adams-Selin, R.D., C. Kalb, T. Jansen, J. Henderson, T. Supinie, L. Harris, and Y. Wang: Just what is "good"? Musings on hail forecast verification through evaluation of FV3-HAILCAST hail forecasts. Wea. Forecasting, submitted.

Allen, J. T., I. M. Giammanco, M. R. Kumjian, H. J. Punge, Q. Zhang, P. Groenemeijer, M. Kunz, and K. Ortega, 2020: Understanding hail in the Earth system. *Rev. Geophys*., **58**, e2019RG000665, https://doi.org/10.1029/2019RG000665.

Barth, M. C., and Coauthors, 2015: The Deep Convective Clouds and Chemistry (DC3) Field Campaign. *Bull. Amer. Meteor. Soc.*, **96**, 1281–1309, https://doi:10.1175/BAMS-D-13-00290.1.

Bela, M. M., M. C. Barth, O. B. Toon, A. Fried, C. L. Ziegler, K. A. Cummings, Y. Li, K. E. Pickering, C. R. Homeyer, H. Morrison, and Q. Yang, 2018: Effects of scavenging, entrainment, and aqueous chemistry on peroxides and formaldehyde in deep convective outflow over the central and southeast United States. *J. Geophys. Res. Atmos.,* **123**, 1-21, doi:10.1029/ 2018JD028271.

Biggerstaff, M. I., and Coauthors, 2005: The Shared Mobile Atmospheric Research and Teaching Radar: A Collaboration to Enhance Research and Teaching. *Bull. Amer. Meteorol. Soc.*, **86**, 1263–1274, doi:10.1175/BAMS-86-9-1263.

Blair, S. F., D. R. Deroche, J. M. Boustead, J. W. Leighton, B. L. Barjenbruch, and W. P. Gargan, 2011: A radar-based assessment of the detectability of giant hail. *Electron. J. Severe Storms Meteor*., **6** (7), https://ejssm.org/archives/2011/vol-6-7-2011/.

Böhm, H. P., 1989: A general equation for terminal fall speed of solid hydrometeors. J. Atmos Sci., 46, 2419–2427, https://doi.org/10.1175/1520-0469(1989)046,2419:AGEFTT.2.0.CO;2.

Brimelow, J. C., G. W. Reuter, and E. R. Poolman, 2002: Modeling maximum hail size in Alberta thunderstorms. *Wea. Forecasting*, **17**, 1048–1062, https://doi:10.1175/1520-0434(2002)017,1048: MMHSIA.2.0.CO;2.

Brimelow, J. C., G. W. Reuter, R. Goodson, and T. W. Krauss, 2006: Spatial forecasts of maximum hail size using prognostic model soundings and HAILCAST. Wea. Forecasting,

**21**, 206–219, doi:10.1175/ WAF915.1.

Brook, J. P., A. Protat, J. Soderholm, J. T. Carlin, H. McGowan, and R. A. Warren, 2021: HailTrack—Improving radar-based hailfall estimates by modeling hail trajectories. *J. Appl. Meteor. Climatol.*, **60**, 237–254, https://doi.org/10.1175/JAMC-D-20-0087.1.

Browning, K. A., 1963: The growth of large hail within a steady updraught. *Quart. J. Roy. Meteor. Soc.*, **89**, 490-506, https://doi.org/10.1002/qj.49708938206.

Browning, K. A., and G. B. Foote, 1976: Air-flow and hail growth in supercell storms and some implications for hail suppression. *Quart. J. Roy. Meteor. Soc.*, **102**, 499–533, https://doi.org/10.1002/qj.49710243303.

Conway, J. W., and D. S. Zrnic, 1993: A study of embryo production and hail growth using dual-Doppler and multiparameter radars. *Mon. Wea. Rev.*, **121**, 2511–2528, https://doi.org/10.1175/1520-0493(1993)121,2511:ASOEPA.2.0.CO;2.

Chmielewski, V. C., D. R. MacGorman, C. L. Ziegler, E. DiGangi, D. Betten, and M. I. Biggerstaff, 2020: Microphysical and transportive contributions to normal and anomalous polarity subregions in the 29-30 May 2012 Kingfisher storm. *Journal of Geophysical Research*, **125**, doi:10.1029/2020JD032384.

Chmielewski, V. C., J. Blair, D. Kennedy, D. MacGorman, and K. M. Calhoun, 2022: A comparison of processing methods for the Oklahoma Lightning Mapping Array. *Earth and Space Science*, **9**, e2021EA002081, https://doi.org/10.1029/2021EA002081.

Chong, S.-L., and C. S. Chen, 1974: Water shells on ice pellets and hailstones. *J. Atmos. Sci.*, **31**, 1384–1391, doi:10.1175/ 1520-0469(1974)031,1384:WSOIPA.2.0.CO;2.

Davenport, C. E., C. L. Ziegler, and M. I. Biggerstaff, 2019: Creating a more realistic idealized supercell thunderstorm evolution via incorporation of base-state environmental variability. *Mon. Wea. Rev.*, **147**, 4177-4198, doi: 10.1175/MWR-D-18-0447.1.

Dawson, D. T., E. R. Mansell, Y. Jung, L. J. Wicker, M. R. Kumjian, and M. Xue, 2014: Low-level ZDR signatures in supercell forward flanks: The role of size sorting and melting of hail. *J. Atmos. Sci.*, **71**, 276–299, https://doi.org/10.1175/JAS-D-13-0118.1.

Dennis, E. J., and M. R. Kumjian, 2017: The impact of vertical wind shear on hail growth in simulated supercells. *J. Atmos. Sci.*, **74**, 641–663, https://doi.org/10.1175/JAS-D-16-0066.1.

Depue, T. K., P. C. Kennedy, and S. A. Rutledge, 2007: Performance of the hail differential reflectivity (HDR) polarimetric radar hail indicator. J. Appl. Meteor. Climatol., 46, 1290–1301, https://doi.org/10.1175/JAM2529.1.

DiGangi, E., 2014: A study of the electrical, kinematic, and microphysical properties of the 29 May 2012 Kingfisher supercell, M.S. thesis, Sch. of Meteorol., The Univ. of Oklahoma, 106 pp.

DiGangi, E. A., D. R. MacGorman, C. L. Ziegler, D. Betten, M. Biggerstaff, M. Bowlan, and C. K. Potvin, 2016: An overview of the 29 May 2012 Kingfisher supercell during DC3. *J. Geophys. Res. Atmos.*, **121**, 14 316–14 343, https://doi.org/10.1002/2016JD025690.

DiGangi, E. A., C. L. Ziegler, and D. R. MacGorman, 2021: Lightning and secondary convection in the anvil of the May 29, 2012 Oklahoma supercell storm observed by DC3, *Journal of Geophysical Research*: *Atmospheres*, **126**, e2020JD033114. https://doi.org/10.1029/2020JD033114

English, M., 1973: Growth of large hail in the storm. Alberta Hailstorms, *Meteor. Monogr.*, **36**, Amer. Meteor. Soc., 37–98, https://doi:10.1007/978-1-935704-32-4_2.

Foote, G. B., 1984: A study of hail growth utilizing observed storm conditions. *J. Climate Appl. Meteor.*, **23**, 84–101, doi:10.1175/1520-0450(1984)023<0084:ASOHGU>2.0.CO;2.

Foote, G. B., and H. W. Frank, 1983: Case study of a hailstorm in Colorado. Part III: Airflow from triple-Doppler measurements. *J. Atmos. Sci*., **40**, 686–707, https://doi.org/10.1175/1520-0469(1983)040<0686:CSOAHI>2.0.CO;2.

Giammanco, I. M., T. M. Brown, R. G. Grant, D. L. Dewey, J. D. Hodel, and R. A. Stumpf, 2015: Evaluating the hardness characteristics of hail through compressive strength measurements. *J. Atmos. Oceanic Technol.,* **32**, 2100–2113, https:// doi.org/10.1175/JTECH-D-15-0081.1.

Gilmore, M. S., J. M. Straka, and E. N. Rasmussen, 2004: Precipitation and evolution sensitivity in simulated deep convective storms: Comparisons between liquid-only and simple ice and liquid phase microphysics, Mon. Wea. Rev., **132**(8), 1897–1916, doi:10.1175/ 1520-0493(2004)132<1897:PAESIS>2.0.CO;2.

Goyer, G. G., Lin, S. S., Gitlin, S. N., and Plooster, M. N., 1969: On the Heat Transfer to Ice Spheres and the Freezing of Spongy Hail. *J. Atmos. Sci.,* **26**, 319-326, https://doi.org/10.1175/1520-0469(1969)026<0319:OTHTTI>2.0.CO;2>

Grant, L. D., and S. C. van den Heever, 2014: Microphysical and dynamical characteristics of low-precipitation and classic supercells. *J. Atmos. Sci*., **71**, 2604–2624, https://doi.org/10. 1175/JAS-D-13-0261.1.

Heymsfield, A. J., 1978: The characteristics of graupel particles in northeastern Colorado cumulus congestus clouds. *J. Atmos. Sci*., **35**, 284–295, doi:10.1175/1520-0469(1978)035,0284:TCOGPI.2.0.CO;2.

Heymsfield A. J., A. R. Jameson, and H. W. Frank, 1980: Hail growth mechanisms in a Colorado storm. Part II: Hail formation processes. *J. Atmos. Sci.,* **37**, 1779-1813, doi.org/10.1175/1520-0469(1980)037<1779:HGMIAC>2.0.CO;2.

Heymsfield A. J., 1982: A comparative study of the rates of development of potential graupel and hail embryos in high plains storms. *J. Atmos. Sci*., **39**, 2867–2897, doi:10.1175/1520-0469(1982)039,2867: ACSOTR.2.0.CO;2.

Heymsfield, A. J., 1983a: A technique for investigating graupel and hail development. *J. Climate Appl. Meteor.*, **22**, 1143–1160, doi:10.1175/ 1520-0450(1983)022,1143:ATFIGA.2.0.CO;2.

Heymsfield, A. J., 1983b: Case study of a hailstorm in Colorado. Part IV: Graupel and hail growth mechanisms deduced through particle trajectory calculations. *J. Atmos. Sci.*, **40**, 1482–1509, doi:10.1175/1520-0469(1983)040,1482:CSOAHI.2.0.CO;2.

Heymsfield, A. J., and D. J. Musil, 1982: Case study of a hailstorm in Colorado. Part II: Particle growth processes at mid-levels deduced form in-situ measurements. *J. Atmos. Sci.*, **39**, 2847–2866, https://doi.org/10.1175/1520-0469(1982)039<2847:CSOAHI>2.0.CO;2.

Heymsfield, A. J., and J. C. Pflaum, 1985: A quantitative assessment of the accuracy of techniques for calculating graupel growth. *J. Atmos. Sci.*, **42**, 2264–2274, https://doi.org/10.1175/1520-0469(1985)042<2264:AQAOTA>2.0.CO;2.

Heymsfield, A. J, Szakáll, M., Jost, A., Giammanco, I., and Wright, R., 2018: A comprehensive observational study of graupel and hail terminal velocity, mass flux, and kinetic energy. *J. Atmos. Sci.,* **75**, 3861-3885, doi.10.1175/JAS-D-18-0035.1.

Heymsfield, A., Szakáll, M., Jost, A., Giammanco, I., Wright, R., and Brimelow, J., 2020: CORRIGENDUM. *J. Atmos. Sci.*, **77**, 405-412, https://doi.org/10.1175/JAS-D-19-0185.1.

Jewell, R., and J. Brimelow, 2009: Evaluation of Alberta hail growth model using severe hail proximity soundings from the United States. Wea. Forecasting, 24, 1592–1609, doi:10.1175/ 2009WAF2222230.1.

Kennedy, P. C., and A. G. Detwiler, 2003: A case study of the origin of hail in a multicell thunderstorm using in situ aircraft and polarimetric radar data. *J. Appl. Meteor.*, **42**, 1679–1690, https://doi.org/10.1175/1520-0450(2003)042,1679:ACSOTO.2.0.CO;2.

Knight, C. A., and N. C. Knight, 1970: The falling behavior of hailstones. J. Atmos. Sci., 27, 672–681, doi:10.1175/ 1520-0469(1970)027,0672:TFBOH.2.0.CO;2.

Knight, C. A., D. H. Ehhalt, N. Roper, and N. C. Knight, 1975: Radial and tangential variation of deuterium in hailstones. *J. Atmos. Sci.*, **32**, 1990–2000, https://doi.org/10.1175/1520-0469(1975)032<1990:RATVOD>2.0.CO;2.

Knight, C. A., and N. C. Knight, 2005: Very large hailstones from Aurora, Nebraska. *Bull. Amer. Meteor. Soc.*, **86**, 1773-1782, doi:10.1175/BAMS-86-12-1773.

Knight, C. A., N. C. Knight, and K. A. Kime, 1981: Deuterium Contents of Storm Inflow and Hailstone Growth Layers. *J. Atmos. Sci.*, **38**, 2485-2499, https://doi.org/10.1175/1520-0469(1981)038<2485:DCOSIA>2.0.CO;2.

Knight, N. C., 1981: The climatology of hailstone embryos. J. Appl. Meteor., **20**, 750–755.

Knight, N. C., 1986: Hailstone shape factor and its relation to radar interpretation of hail. *J. Climate Appl. Meteor.,* **25**, 1956–1958, https://doi.org/10.1175/1520-

0450(1986)025,1956:HSFAIR. 2.0.CO;2.

Knight, C. A., and K. R. Knupp, 1986: Precipitation growth trajectories in a CCOPE storm. *J. Atmos. Sci.*, **43**, 1057–1073, https://doi.org/10.1175/1520-0469(1986)043<1057:PGTIAC>2.0.CO;2.

Knight, C. A., P. T. Schlatter, and T. W. Schlatter, 2008: An unusual hailstorm on 24 June 2006 in Boulder, Colorado. Part II: Low- density growth of hail. *Mon. Wea. Rev.,* **136**, 2833–2348, doi:10.1175/2008MWR2338.1.

Kumjian, M. R., and K. A. Lombardo, 2020: A hail growth trajectory model for exploring the environmental controls on hailsize: Model physics and idealized tests. *J. Atmos. Sci.*, **77**, 2765–2791, https://doi.org/10.1175/JAS-D-20-0016.1.

Kumjian, M. R., Gutierrez, R., Soderholm, J. S., Nesbitt, S. W., Maldonado, P., Luna, L. M., Marquis, J., Bowley, K. A., Imaz, M. A., and Salio, P., 2020: Gargantuan Hail in Argentina. *Bull. Amer. Meteor. Soc.*, **101**, E1241-E1258, https://doi.org/10.1175/BAMS-D-19-0012.1.

Kumjian, M. R., and K. A. Lombardo, and S. Loeffler, 2021: The evolution of hail production in simulated supercell storms. *J. Atmos. Sci.*, **78**, 3417–3440, https://doi.org/10.1175/JAS-D-21-0034.1.

Kumjian, M. R., and A. V. Ryzhkov, 2008: Polarimetric signatures in supercell thunderstorms. *J. Appl. Meteor. Climatol.*, **47**, 1940–1961, https://doi.org/10.1175/2007JAMC1874.1.

Kumjian, M. R., and A. V. Ryzhkov, 2012: The impact of size sorting on the polarimetric radar variables. *J. Atmos. Sci.*, **69**, 2042–2060, https://doi.org/10.1175/JAS-D-11-0125.1.

Jewell, R., and J. Brimelow, 2009: Evaluation of Alberta hail growth model using severe hail proximity soundings from the United States. *Wea. Forecasting.*, **24**, 1592–1609, doi:10.1175/ 2009WAF2222230.1.

Johnson, A. W., and K. E. Sugden, 2014: Evaluation of soundingderived thermodynamic and wind-related parameters associated with large hail events. *Electron. J. Severe Storms Meteor.*, **9** (5), https://ejssm.org/archives/2014/vol-9-5-2014/.

Lamb, D., and J. Verlinde, 2011: Physics and Chemistry of Clouds. 1st ed. Cambridge University Press, 584 pp.

Lesins, G. B., and R. List, 1986: Sponginess and drop shedding of gyrating hailstones in a pressure-controlled icing wind tunnel. *J. Atmos. Sci.*, **43**, 2813–2825, doi:10.1175/1520-0469(1986)043<2813:SADSOG>2.0.CO;2.

List, R., 1960a: Growth and structure of graupel and hailstones. *Physics of Precipitation, Geophys. Monogr.*, **5**, Amer. Geophys. Union, 317–324.

List, R., 1960b: New developments in hail research. *Science*, **132**, 1091–1098, https://doi: 10.1126/science.132.3434.1091

Ludlam, F. H., 1958: The hail problem. *Nubila*, **1**, 12–96.

Macklin, W. C., 1961: Accretion in mixed clouds. *Quart. J. Roy. Meteor. Soc.*, **87**, 413–424, doi:10.1002/qj.49708737312.

Macklin, W. C., 1963: Heat transfer from hailstones. *Quart. J. Roy. Meteor. Soc*., **89**, 360–369, https://doi.org/10.1002/qj.49708938107.

Majcen, M., P. Markowski, Y. Richardson, D. Dowell, and J. Wurman, 2008: Multipass objective analyses of Doppler radar data. *J. Atmos. Oceanic Technol*., **25**, 1845–1858, doi:10.1175/2008JTECHA1089.1.

Mansell, E. R., C. L. Ziegler, and E. Bruning, 2010: Simulated Electrification of a Small Thunderstorm with Two-Moment Bulk Microphysics. *J. Atmos. Sci.,* **67**, 171-194, 10.1175/2009JAS2965.1.

Miller, L. J., and J. C. Fankhauser, 1983: Radar echo structure, air motion and hail formation in a large stationary multicellular thunderstorm. *J. Atmos. Sci.*, **40**, 2399–2418, https://doi.org/10.1175/1520-0469(1983)040<2399:RESAMA>2.0.CO;2.

Miller, L. J., J. D. Tuttle, and C. A. Knight, 1988: Airflow and hail growth in a severe northern plains supercell. *J. Atmos. Sci.*, **45**, 736–762, https://doi.org/10.1175/1520-0469(1988)045,0736: AAHGIA.2.0.CO;2.

Miller, L. J., J. D. Tuttle, and G. B. Foote, 1990: Precipitation production in a large Montana hailstorm: Airflow and particle growth trajectories. *J. Atmos. Sci.*, **47**, 1619–1646, https://doi.org/10.1175/1520-0469(1990)047<1619:PPIALM>2.0.CO;2.

Musil, D. J., 1970: Computer modeling of hailstone growth in feeder clouds. *J. Atmos. Sci.*, **27**, 474–482, doi:10.1175/1520-0469(1970)027<0474:CMOHGI>2.0.CO;2.

Musil, D. J., A. J. Heymsfield, and P. L. Smith, 1986: Microphysical characteristics of a well-developed weak echo region in a high-plains supercell thunderstorm. *J. Climate Appl. Meteor.*, **25**, 1037–1051, https://doi.org/10.1175/1520-0450(1986)025<1037:MCOAWD>2.0.CO;2.

Morgan, G. M., Jr, 1972: On the Growth of Large Hail. *Mon. Wea. Rev*, **100**, 196-205, https://doi.org/10.1175/1520-0493(1972)100<0196:OTGOLH>2.3.CO;2>.

Nelson, S. P., 1983: The influence of storm flow structure on hail growth. *J. Atmos. Sci.*, **40**, 1965–1983, https://doi.org/10.1175/1520-0469(1983)040<1965:TIOSFS>2.0.CO;2.

Nelson, S. P., and N. C. Knight, 1987: The hybrid multicellular–supercellular storm—An efficient hail producer. Part I: An archetypal example. *J. Atmos. Sci.*, **44**, 2042–2059, doi.org/10.1175/1520-0469(1987)044%3c2042:THMSEH>2.0.CO;2.

Nelson, S. P., 1987: The hybrid multicellular-supercellular storm—An efficient hail producer. Part II: General characteristics and implications for hail growth. *J. Atmos. Sci.*, **44**, 2060–

2073, https://doi.org/10.1175/1520-0469(1987)044<2060:THMSEH>2.0.CO;2.

Ortega, K. L., J. M. Krause, and A. V. Ryzhkov, 2016: Polarimetric radar characteristics of melting hail. Part III: Validation of the algorithm for hail size discrimination. J. Appl. Meteor. Climatol., 55, 829–848, https://doi.org/10.1175/JAMC-D-15-0203.1.

Orville, Harold D., and Fred J. Kopp, 1977: Numerical Simulation of the Life History of a Hailstorm. *J. Atmos. Sci.*, **34**, 1596-1618. https://doi.org/10.1175/1520-0469(1977)034<1596:NSOTLH>2.0.CO;2.

Paluch, I. R., 1978: Size sorting of hail in a three-dimensional updraft and implications for hail suppression. *J. Appl. Meteor. Climatol.*, **17**, 763–777, doi.org/10.1175/15200450(1978)017,0763:SSOHIA.2.0.CO;2.

Peters, J. M., C. J. Nowotarski, and H. C. Morrison, 2019: The role of vertical wind shear in modulating maximum supercell updraft velocities. *J. Atmos. Sci.*, **76**, 3169–3189, https://doi.org/10.1175/JAS-D-19-0096.1.

Peters, J. M., H. Morrison, C. J. Nowotarski, J. P. Mulholland, and R. L. Thompson, 2020a: A formula for the maximum vertical velocity in supercell updrafts. *J. Atmos. Sci.*, **77**, 3747–3757, https://doi.org/10.1175/JAS-D-20-0103.1.

Picca, J. C., and A. V. Ryzhkov, 2012: A dual-wavelength polarimetric analysis of the 16 May 2010 Oklahoma City extreme hailstorm. *Mon. Wea. Rev.*, **140**, 1385–1403, https://doi.org/10.1175/MWR-D-11-00112.1.

Poolman, E. R., 1992: Die voorspelling van haelkorrelgroei in Suid-Afrika (The forecasting of hail growth in South Africa). M.S. thesis, Faculty of Engineering, University of Pretoria, 113 pp.

Pruppacher, H. R., and J. D. Klett, 1997: Microphysics of Clouds and Precipitation. 2nd ed. Kluwer Academic, 954 pp.

Rasmussen, R. M., and A. J. Heymsfield, 1985: A generalized form for impact velocities used to determine graupel accretional densities. J. Atmos. Sci., **42**, 2275–2279.

Rasmussen, R. M., and A. J. Heymsfield, 1987a: Melting and shedding of graupel and hail. Part I: Model physics. *J. Atmos. Sci.*, **44**, 2754–2763, doi:10.1175/1520-0469(1987)044,2754:MASOGA.2.0.CO;2.

Rasmussen, R. M., and A. J. Heymsfield, 1987b: Melting and shedding of graupel and hail. Part III: Investigation of the role of shed drops as hail embryos in the 1 August CCOPE severe storm. *J. Atmos. Sci.*, **44**, 2783–2803, https://doi.org/10.1175/ 1520-0469(1987)044,2783:MASOGA.2.0.CO;2.

Roos, D. S., and A. E. Carte, 1973: The falling behavior of oblate and spiky hailstones. *J. Rech. Atmos.*, **7**, 39–52.

Rosinski, J., Knight, C. A., Nagamoto, C. T., Morgan, G. M., Knight, N. C., and Prodi, F., 1979: Further Studies of Large, Water-Insoluble Particles within Hailstones. *J. Atmos. Sci.*, **36**, 882-891, https://doi.org/10.1175/1520-0469(1979)036<0882:FSOLWI>2.0.CO;2

Ryzhkov, A. V., T. J. Schuur, D. W. Burgess, and D. S. Zrnić, 2005: Polarimetric tornado detection. *J. Appl. Meteor.*, **44**, 557–570, https://doi.org/10.1175/JAM2235.1.

Shedd, L., M. R. Kumjian, I. Giammanco, T. Brown-Giammanco, and B. R. Maiden, 2021: Hailstone Shapes. *J. Atmos. Sci*., **78**, 639-652, https://doi.org/10.1175/JAS-D-20-0250.1.

Taszarek, M., H. E. Brooks, and B. Czernecki, 2017: Sounding derived parameters associated with convective hazards in Europe. *Mon. Wea. Rev.*, **145**, 1511–1528, https://doi.org/10.1175/MWR-D-16-0384.1.

Waugh, S. M., C. L. Ziegler, C. L., and D. R. MacGorman, 2018: In situ microphysical observations of the 29–30 May 2012 Kingfisher, OK, supercell with a balloon-borne video disdrometer. J. Geophys. Res: Atmospheres, **123**. https://doi.org/ 10.1029/2017JD027623.

Witt, A., D. W. Burgess, A. Seimon, J. Allen, J. C. Snyder, and H. B. Bluestein, 2018: Hailstone Shapes. *Wea. Forecasting*, **33**, 1263-1282, https://doi.org/10.1175/WAF-D-18-0003.1.

Witt, A., M. D. Eilts, G. J. Stumpf, J. T. Johnson, E. D. W. Mitchell, and K. W. Thomas, 1998: An enhanced hail detection algorithm for the WSR-88D. Wea. Forecasting, 13, 286–303, https://doi.org/10.1175/1520-0434(1998)013<0286:AEHDAF>2.0.CO;2.

Yang, Q. , R. C. Easter, P. Campuzano-Jost, J. Jimenez, J. D. Fast, S. J. Ghan, H. Wang, L. K. Berg, M. C. Barth, Y. Liu, M. B. Shrivastava, B. Singh, H. Morrison, J. Fan, C. L. Ziegler, M. Bela, E. Apel, G. S. Diskin, T. Mikoviny, and A. Wisthaler, 2015: Aerosol transport and wet scavenging in deep convective clouds: A case study and model evaluation using a multiple passive tracer analysis approach. *J. Geophys. Res. Atmos.,* **120**, 8448–8468, doi:10.1002/ 2015JD023647.

Ziegler, C. L., P. S. Ray, and N. C. Knight, 1983: Hail growth in an Oklahoma multicell storm. *J. Atmos. Sci.*, **40**, 1768–1791, doi:10.1175/1520-0469(1983)040<1768:HGIAOM>2.0.CO;2.

Ziegler, C. L., 1985: Retrieval of thermal and microphysical variables in observed convective storms. Part I: Model development and preliminary testing. *J. Atmos. Sci.,* **42**, 1487-1509.

Ziegler, C. L., 1988: Retrieval of thermal and microphysical variables in observed convective storms. Part II: Sensitivity of cloud processes to variation of the microphysical parameterization. *J. Atmos. Sci*., **45**, 1072-1090.

Ziegler, C. L., D. MacGorman, J. Dye, and P. Ray, 1991: A model evaluation of non-inductive graupel-ice charging in the early electrification of a mountain thunderstorm. *J. Geophys. Res.*, **96**, 12,833-12,855.

Ziegler, C. L., 2013a: A diabatic Lagrangian technique for the analysis of convective storms. Part I: Description and validation via an observing system simulation experiment. *J. Atmos.*

*Oceanic Technol.*, **30**, 2248–2265, https://doi.org/10.1175/JTECH-D-12-00194.1.

Ziegler, C. L., 2013b: A diabatic Lagrangian technique for the analysis of convective storms. Part II: Application to a radar-observed storm. *J. Atmos. Oceanic Technol.*, **30**, 2266–2280, https://doi.org/10.1175/JTECH-D-13-00036.1.

# Appendix A: Tables

**Table 1.** List of hail trajectory model parameters and variables.

| Variable Name | Symbol | Units | Value |
|---|---|---|---|
| drag coefficient | $C_D$ | unitless | |
| **specific heat capacity of ice** | $c_{p,i}$ | | |
| specific heat capacity of water | $c_{p,w}$ | | |
| hailstone diameter | $D$ | m | |
| **cloud droplet diameter** | $D_c$ | m | |
| equivalent spherical volume diameter | $D_{eq}$ | m | |
| minimum oblate spheroidal diameter | $D_{min}$ | m | |
| maximum oblate spheroidal diameter | $D_{max}$ | m | |
| **diffusivity of water vapor in air** | $D_v$ | | |
| oblate spheroidal hailstone aspect ratio upper limit | $\varphi_{\text{high}}$ | unitless | |
| oblate spheroidal hailstone aspect ratio lower limit | $\varphi_{\text{low}}$ | unitless | |
| oblate spheroidal hailstone aspect ratio | $\varphi_{\text{min}}$ | unitless | |
| saturation vapor pressure of the environment | $e_{s.a}$ | | |
| saturation vapor pressure at the hailstone surface | $e_{s,s}$ | | |
| **cloud water collection efficiency** | $E_{cw}$ | unitless | |
| cloud ice collection efficiency | $E_{cx}$ | unitless | |
| mean ventilation coefficient for heat | $\overline{f_H}$ | | |
| water vapor ventilation coefficient | $\overline{f_v}$ | | |
| hailstone water fraction | $F_w$ | unitless | |
| gravitational acceleration | g | m s$^2$ | 9.8 |
| **heat transfer rate** | $h$ | | |
| latent heat of vaporization | $L_e$ | | |
| **latent heat of melting** | $L_m$ | | |
| hailstone mass | $m$ | kg | |
| hailstone ice core mass | $M_{ice}$ | kg | |
| **surface water shell mass** | $M_{sfc}$ | kg | |
| **surface water shell mass threshold** | $M_{wcrit}$ | kg | |
| Prandtl number | Pr | | |
| cloud water mixing ratio | $q_c$ | g kg$^{-1}$ | |
| cloud ice mixing ratio | $q_x$ | g kg$^{-1}$ | |
| gas constant for water vapor | $R_v$ | | |
| **Reynolds number** | Re | Unitless | |
| Reynolds number (Best number relationship) | $Re_X$ | unitless | |
| **Schmidt number** | Sc | | |
| ambient environmental temperature | $T_a$ | K | |
| hailstone surface temperature | $T_s$ | K | |
| hailstone impact velocity | $V_t$ | | |
| hailstone terminal velocity | $V_{imp}$ | m s$^{-1}$ | |
| hailstone terminal velocity | $V_{t\,(\text{oblate})}$ | m s$^{-1}$ | |
| Best number | $X$ | unitless | |

**Table 1 (continued).** List of hail trajectory model parameters and variables.

| | | | |
|---|---|---|---|
| u-component (West-East) | u | m s$^{-1}$ | |
| v-component (South-North) | v | m s$^{-1}$ | |
| w-component (vertical) | w | m s$^{-1}$ | |
| **reflectivity** | Z | dBZ | |
| **change in hailstone mass since last timestep** | $\Delta m$ | kg | |
| hailstone mass growth due to ice accretion since last timestep | | | |
| change in hailstone heat content since last timestep | $\Delta q$ | | |
| difference in temperature between ambient air and equilibrium state at the hailstone surface | $\Delta T$ | K | |
| difference in vapor density between ambient air and equilibrium state at the hailstone surface | $\Delta \rho$ | kg m$^{-3}$ | |
| air density | $\rho_a$ | kg m$^{-3}$ | |
| air density at Mean Sea Level | $\rho_{a0}$ | kg m$^{-3}$ | 1.225 |
| **bulk** hail **density** | $\rho_h$ | kg m$^{-3}$ | |
| hail ice **layer density** | $\rho_l$ | kg m$^{-3}$ | |
| water vapor density at the hailstone surface | $\rho_{v,s}$ | kg m$^{-3}$ | |
| water vapor density of the ambient environment | $\rho_{v,a}$ | kg m$^{-3}$ | |
| dynamic viscosity of air | $\nu_d$ | | |
| kinematic viscosity of air | $\nu_k$ | | $1.252 \times 10^{-5}$ |
| heat transfer coefficient | $\chi$ | unitless | |
| heat transfer coefficient upper limit | $\chi_{\text{high}}$ | unitless | |
| heat transfer coefficient lower limit | $\chi_{\text{low}}$ | unitless | |

**Table 2.** List of radar analysis time with (x, y) embryo domain origin coordinates relative the fixed ground-relative radar analysis origin.

| Radar Analysis Time | X origin | Y origin |
|---|---|---|
| 2251 UTC | 17 | 28 |
| 2254 UTC | 18 | 27 |
| 2257 UTC | 19 | 26 |
| 2300 UTC | 20 | 25 |
| 2303 UTC | 21 | 24 |
| 2306 UTC | 22 | 23 |
| 2309 UTC | 23 | 22 |
| 2312 UTC | 24 | 21 |
| 2315 UTC | 25 | 20 |
| 2318 UTC | 26 | 19 |
| 2321 UTC | 27 | 18 |
| 2324 UTC | 28 | 17 |
| 2327 UTC | 29 | 16 |
| 2330 UTC | 30 | 15 |
| 2333 UTC | 31 | 14 |
| 2336 UTC | 32 | 13 |
| 2339 UTC | 33 | 12 |
| 2342 UTC | 34 | 11 |
| 2345 UTC | 35 | 10 |
| 2348 UTC | 36 | 9 |
| 2351 UTC | 37 | 8 |
| 2354 UTC | 38 | 7 |
| 2357 UTC | 39 | 6 |
| 0000 UTC | 40 | 5 |

**Table 3**. Numbered local storm reports (LSRs) and IBHS hail observations in Blaine and Kingfisher Counties, OK that were within or near the path of the Kingfisher, OK supercell. The maximum diameter (cm) of the sampled IBHS hailstones (sampled in Kingfisher beginning around 0056 UTC on 30 May) ranged from 1.1 cm to 7.8 cm (i.e., "variable*" Obs #13).

| Obs # | Time (UTC) | Size (in) | Size (cm) | Location | County | Lat | Lon |
|---|---|---|---|---|---|---|---|
| 1 | 0006 | 1.50 | 3.80 | 1 E Loyal | Kingfisher | 35.97 | -98.10 |
| 2 | 0008 | 2.75 | 7.00 | 5 E Loyal | Kingfisher | 35.97 | -98.03 |
| 3 | 0016 | 2.00 | 5.00 | 5 SW Dover | Kingfisher | 35.93 | -97.97 |
| 4 | 0017 | 1.50 | 3.80 | 5 N Kingfisher | Kingfisher | 35.93 | -97.93 |
| 5 | 0045 | 2.75 | 7.00 | 1 E Kingfisher | Kingfisher | 35.86 | -97.91 |
| 6 | 0048 | 3.00 | 7.60 | 2 S Kingfisher | Kingfisher | 35.83 | -97.93 |
| 7 | 0056 | variable* | variable* | Kingfisher | Kingfisher | 35.85 | -97.93 |

# Appendix B: Figures

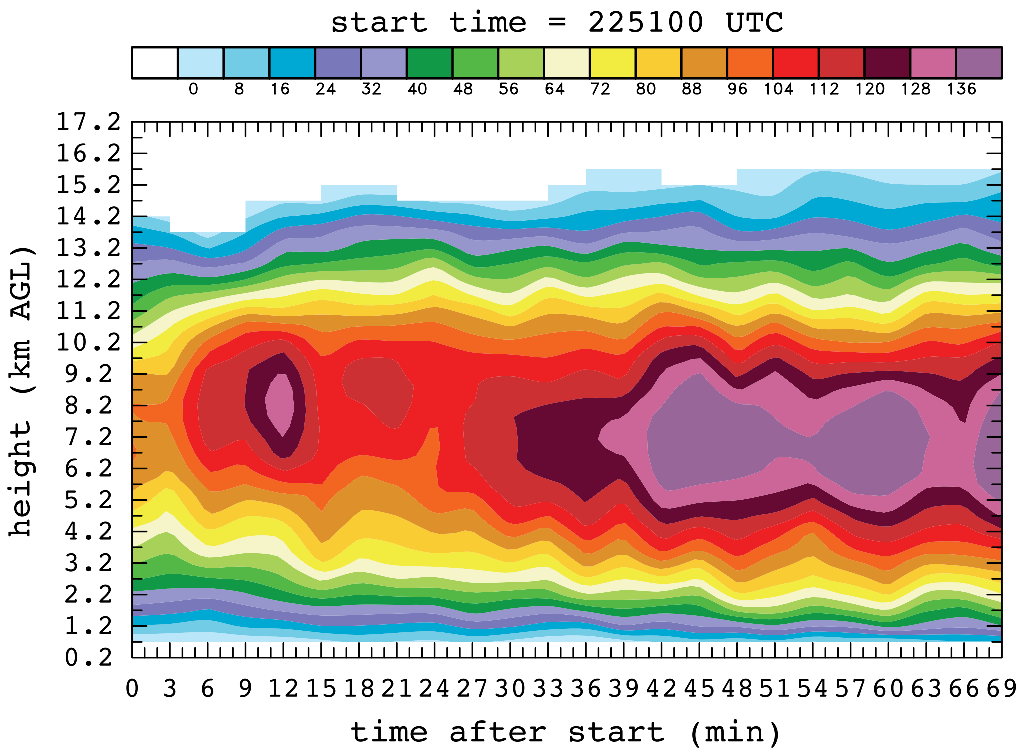


**Figure 1**. Time series of updraft volume during analysis period between 2251 UTC (0 minutes) – 0000 UTC (69 minutes).

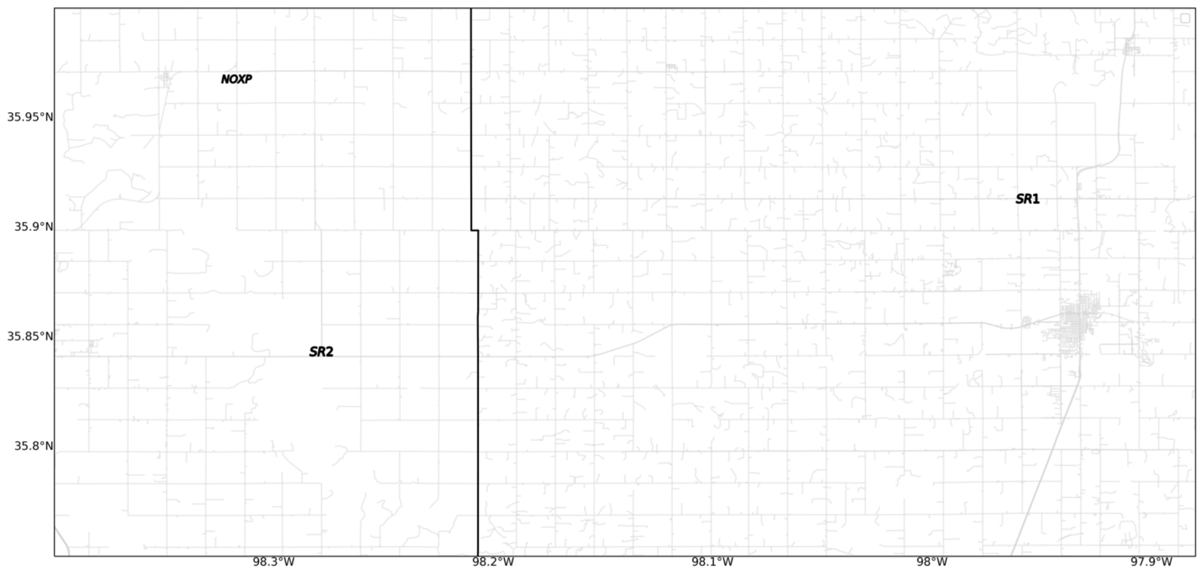


**Figure 2.** Road network and mobile radar (SR1, SR2, and NOXP) locations.

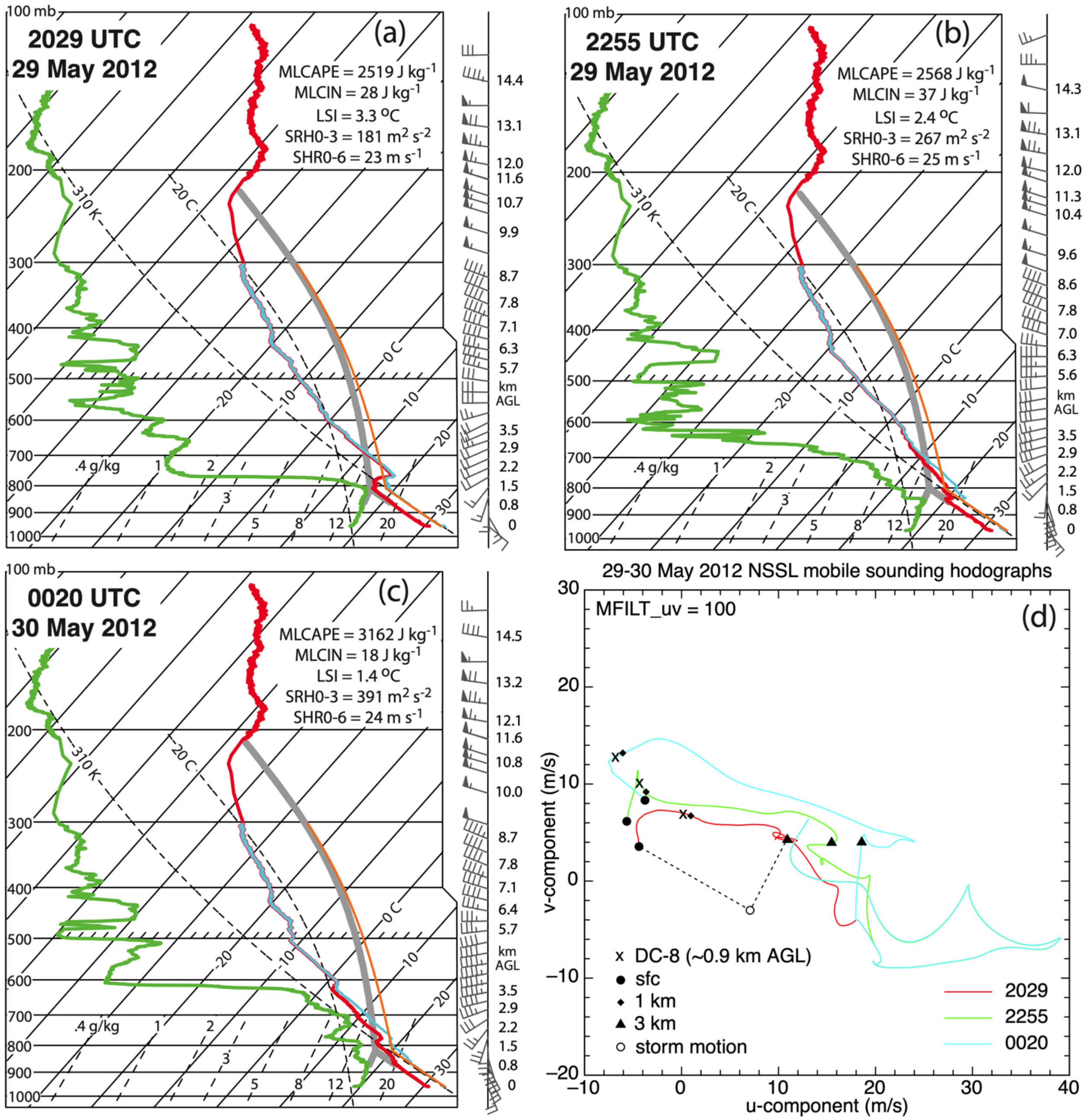


**Figure 3.** Far-environmental, mobile storm-following soundings taking at (a) 2029 UTC on 29 May, (b) 2255 UTC, and (c) 0020 UTC on 30 May 2012. Panel (d) depicts the hodograph evolution from the three soundings, with 2029 UTC (red), 2255 UTC (green), and 0020 UTC (cyan). The surface is denoted by a solid black dot, 1 km by a solid diamond, and 3 km by a solid triangle. The open circle denotes the storm motion. Figure adapted from Fig. 1 of Davenport, Ziegler, and Biggerstaff (MWR, 2019), by courtesy of the authors and the American Meteorological Society.

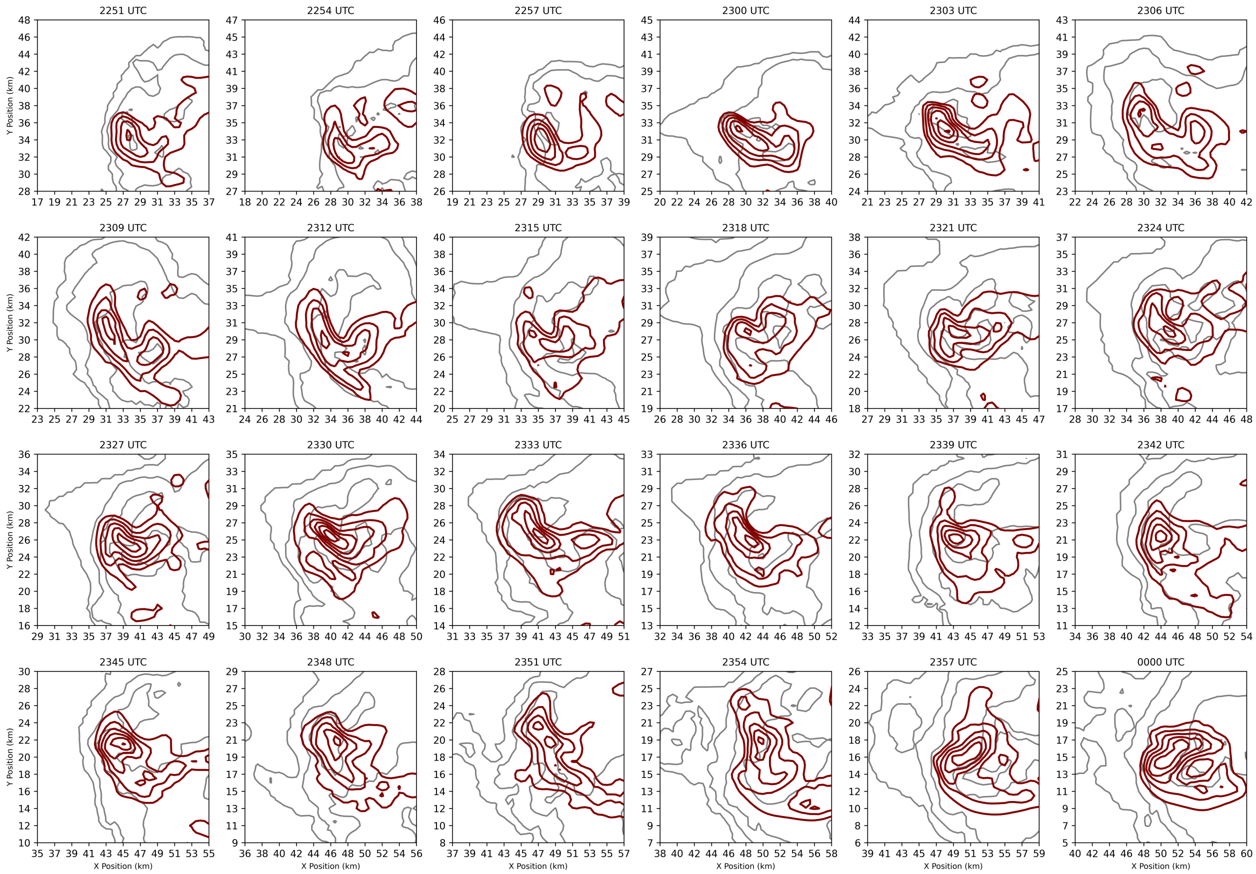

**Figure 4.** Embryo domain (20 km x 20 km) for all 24 analysis times between 29 May 2251 UTC and 30 May 0000 UTC. Red contours are vertical velocity at 10 m s$^{-1}$ beginning at 10 m s$^{-1}$ intervals and gray contours are reflectivity contoured at 20 dBZ intervals beginning at 10 dBZ.

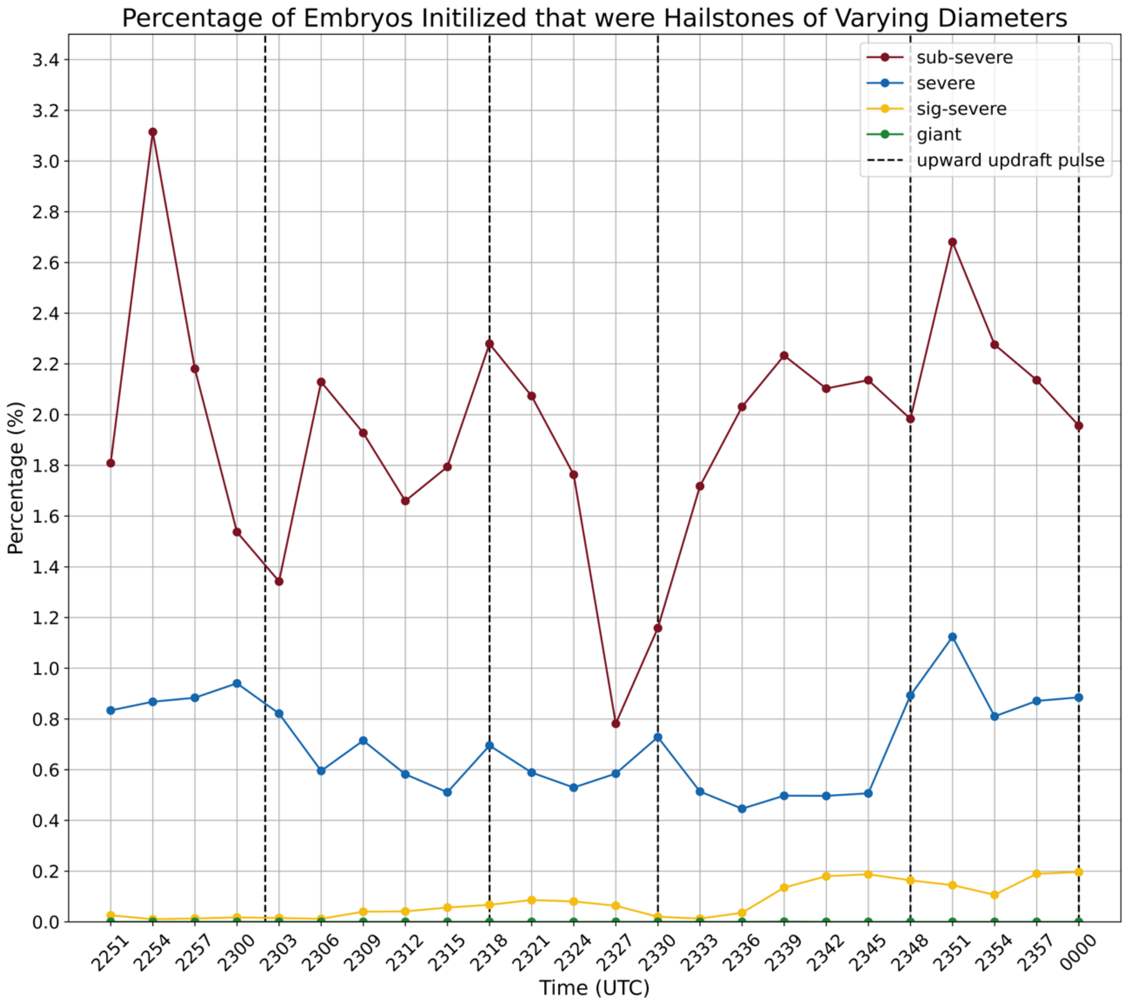


**Figure 5.** Percentage of embryos that resulted in sub-severe (red), severe (blue), significantly severe (yellow), and giant (green) hailstones from all embryos initialized at that analysis time. Percentages are shown for all 24 analysis times. The dotted black lines represent the times the updraft pulsed upward.

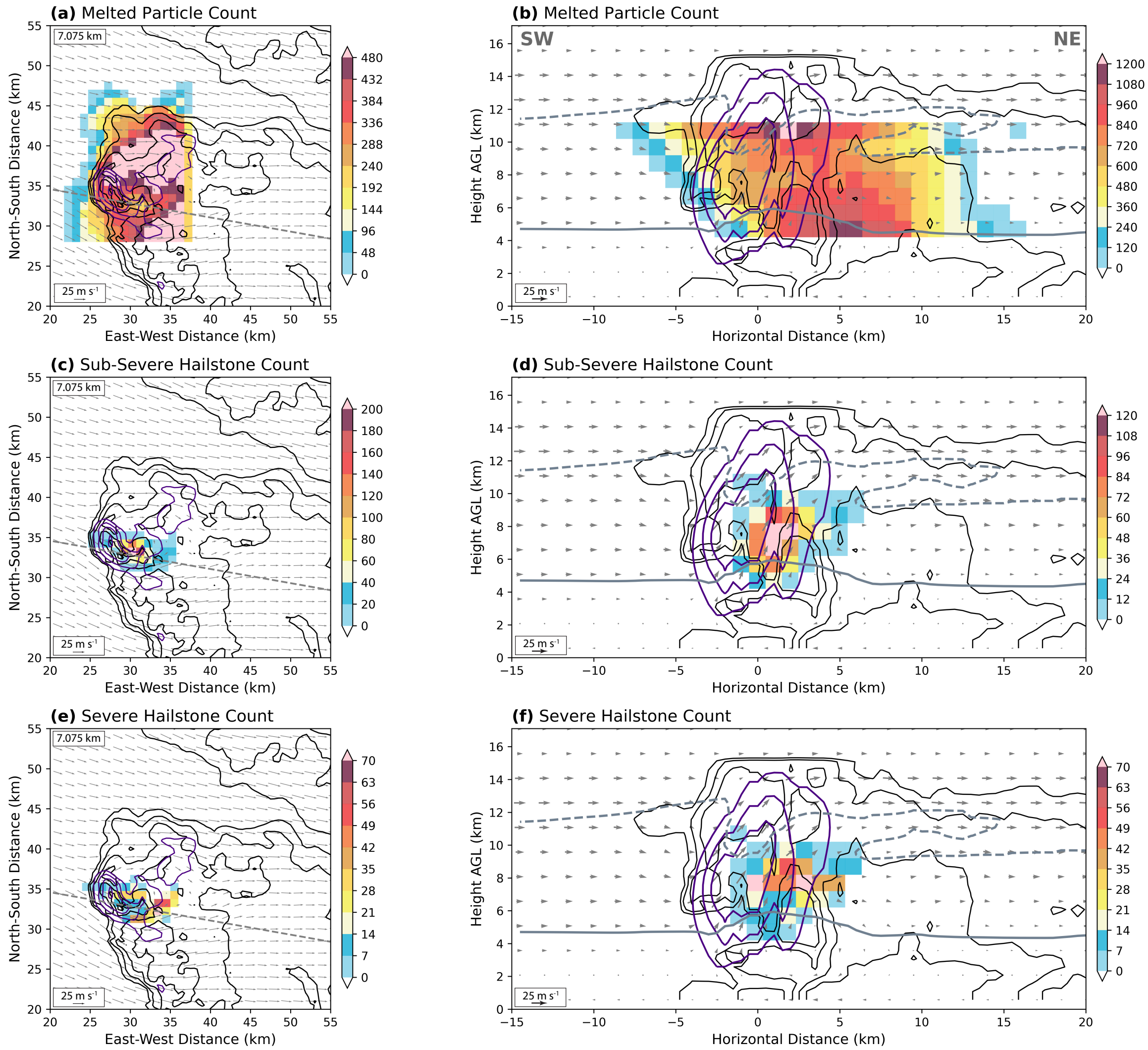


**Figure 6.** 2-D histograms of modeled hail particles that illustrate initial locations of (a, b) hail particles that completely melt above ground, (c, d) surface sub-severe hailstones, and (e, f) surface severe hailstones in the Kingfisher storm at 2251 UTC. (a, c, e) Hailstone counts in a 1 km x 1 km grid cell in the x-y plane integrated through the full radar analysis domain depth. Wind vectors denoted by the gray arrows are ground relative at 7.075 km (AGL). Black contours are reflectivity starting at 20 dBZ at 10 dBZ increments at 7.075 km. Purple contours are vertical velocity starting at 10 m s$^{-1}$ at 10 m s$^{-1}$ increments at 7.075 km. A black "x" is shown where the maximum of the mean vertical velocity at all levels is found. A dashed black line denotes the cross section shown directly to the right of the panel. (b, d, f) Hailstone counts in a 1 km x 1 km grid cell in the corresponding cross section denoted by the black dashed line in (a, b, c), where grid cells are horizontally integrated across the full radar analysis domain in the direction normal to the cross-section. The dashed gray line indicates the -40 °C level and the solid gray line indicates the 0 °C level.

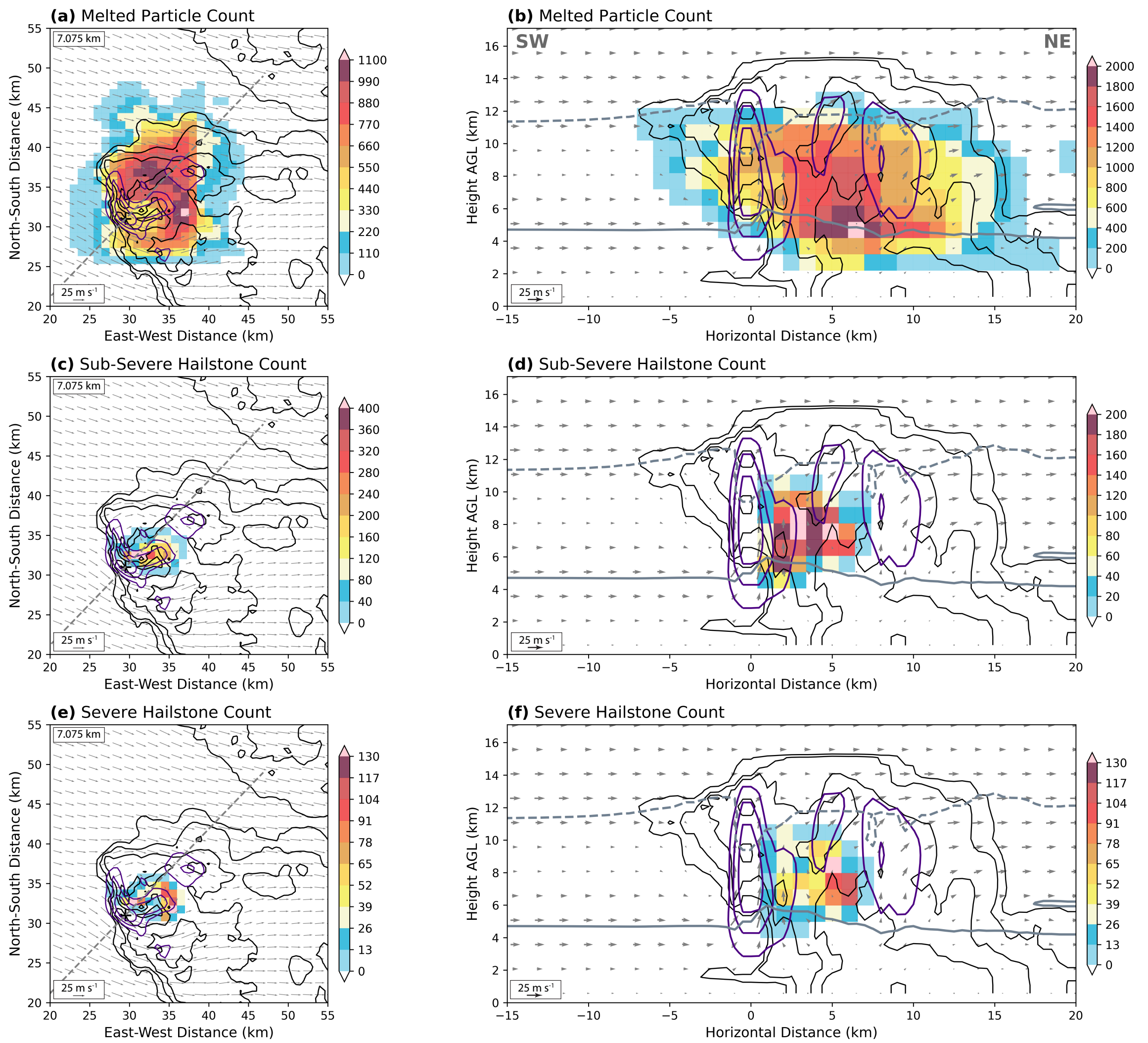


**Figure 7.** As in Figure 6, but 2254 UTC.

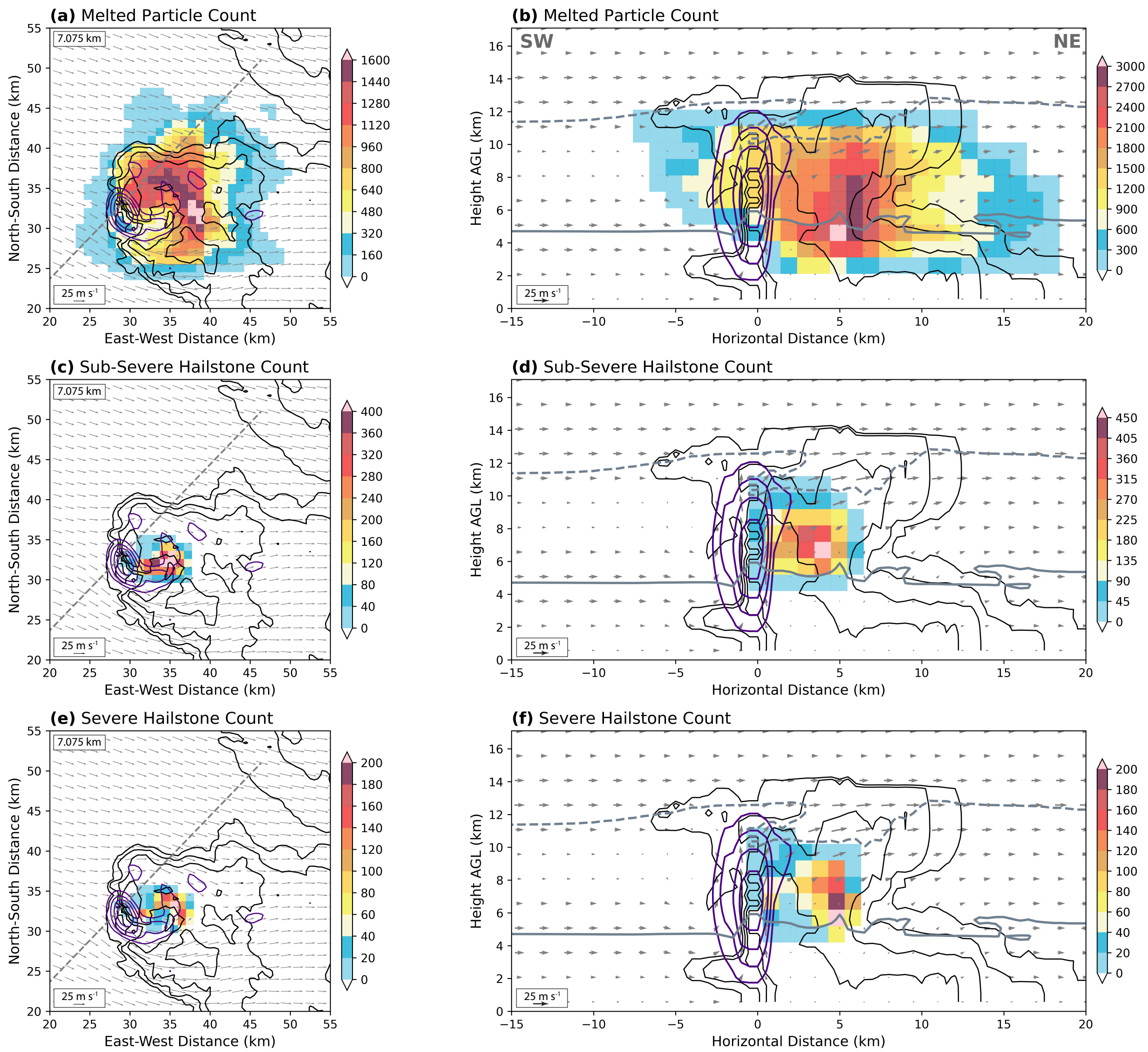


**Figure 8.** As in Figure 6, but 2257 UTC.

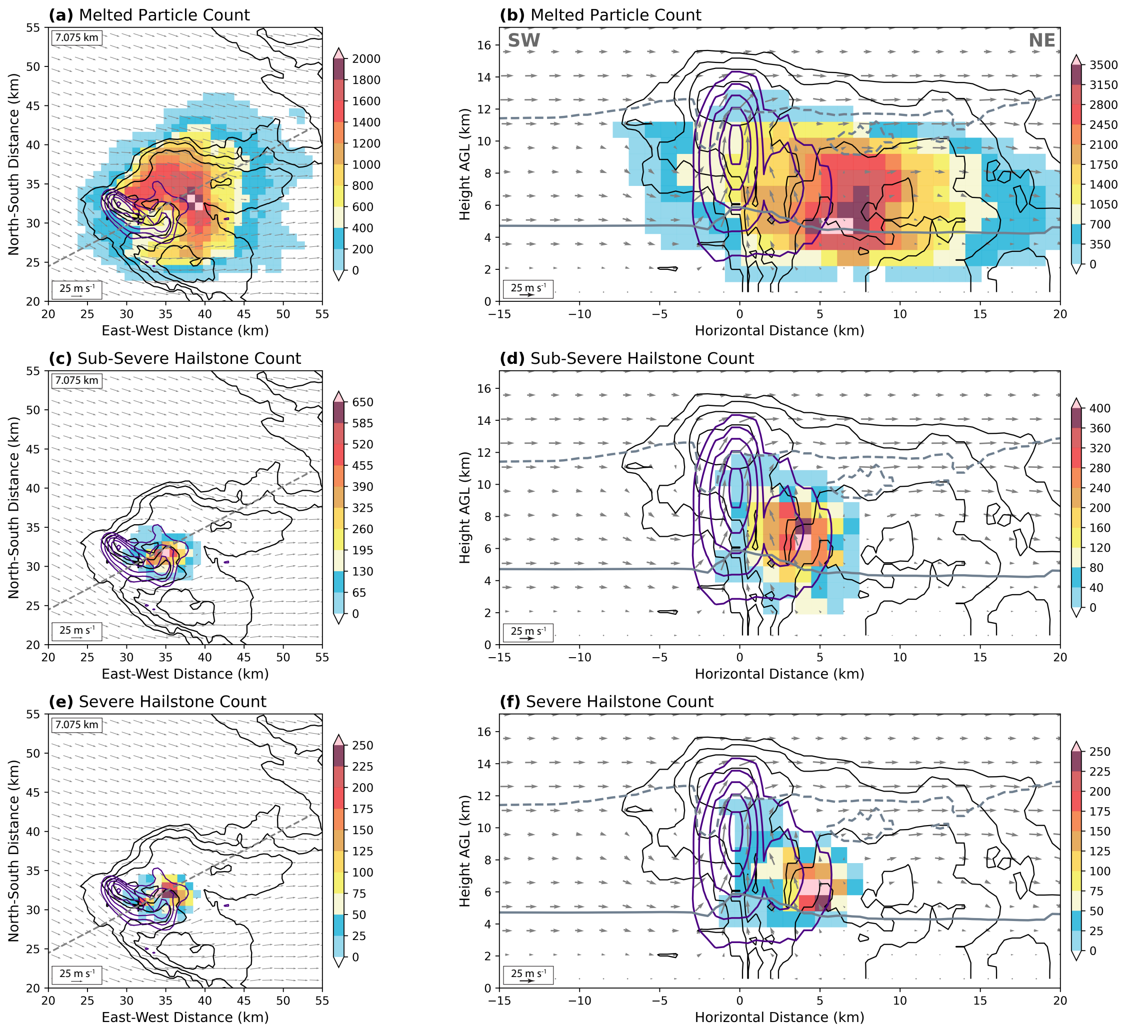


**Figure 9.** As in Figure 6, but 2300 UTC.

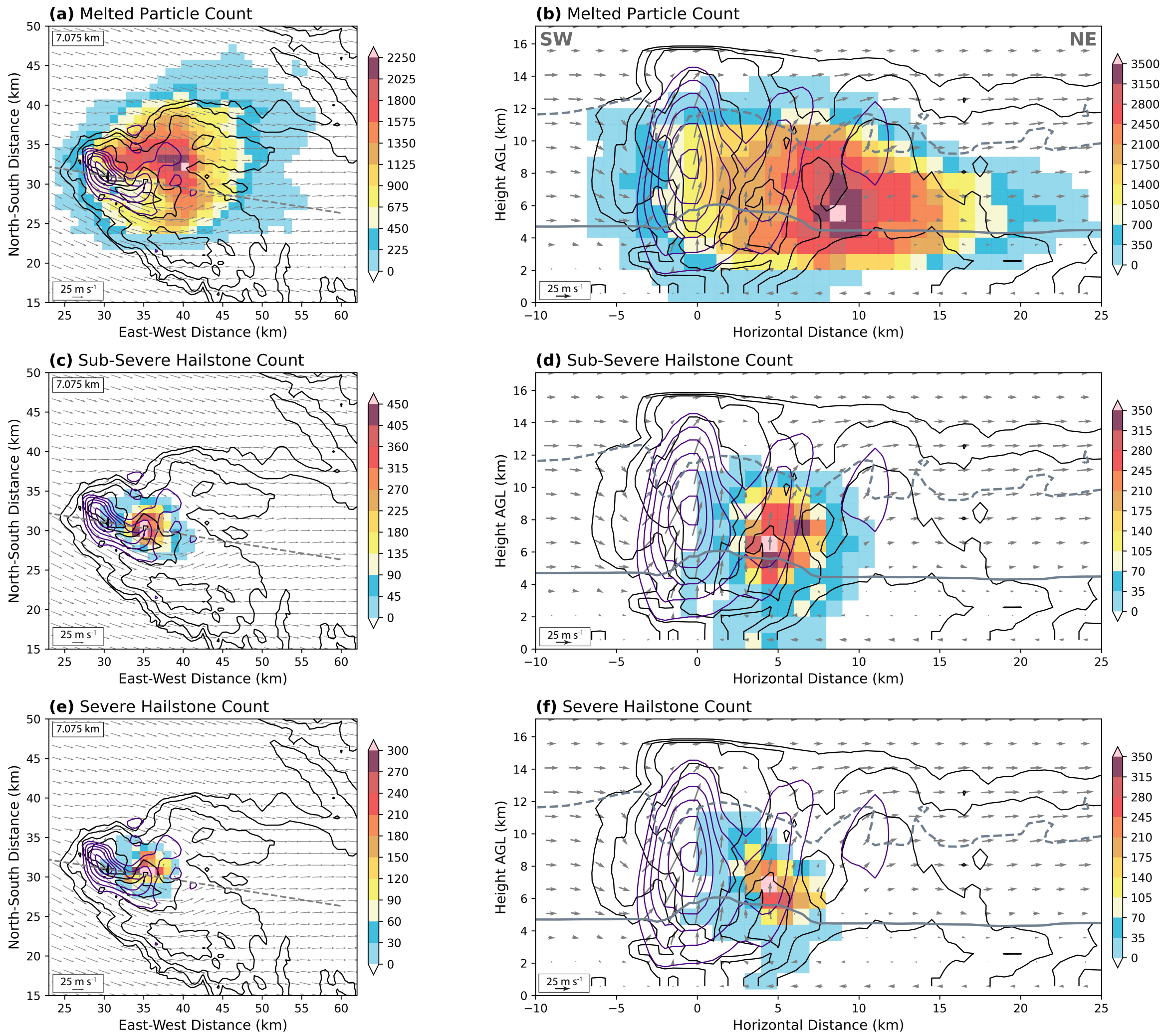


**Figure 10.** As in Figure 6, but 2303 UTC.

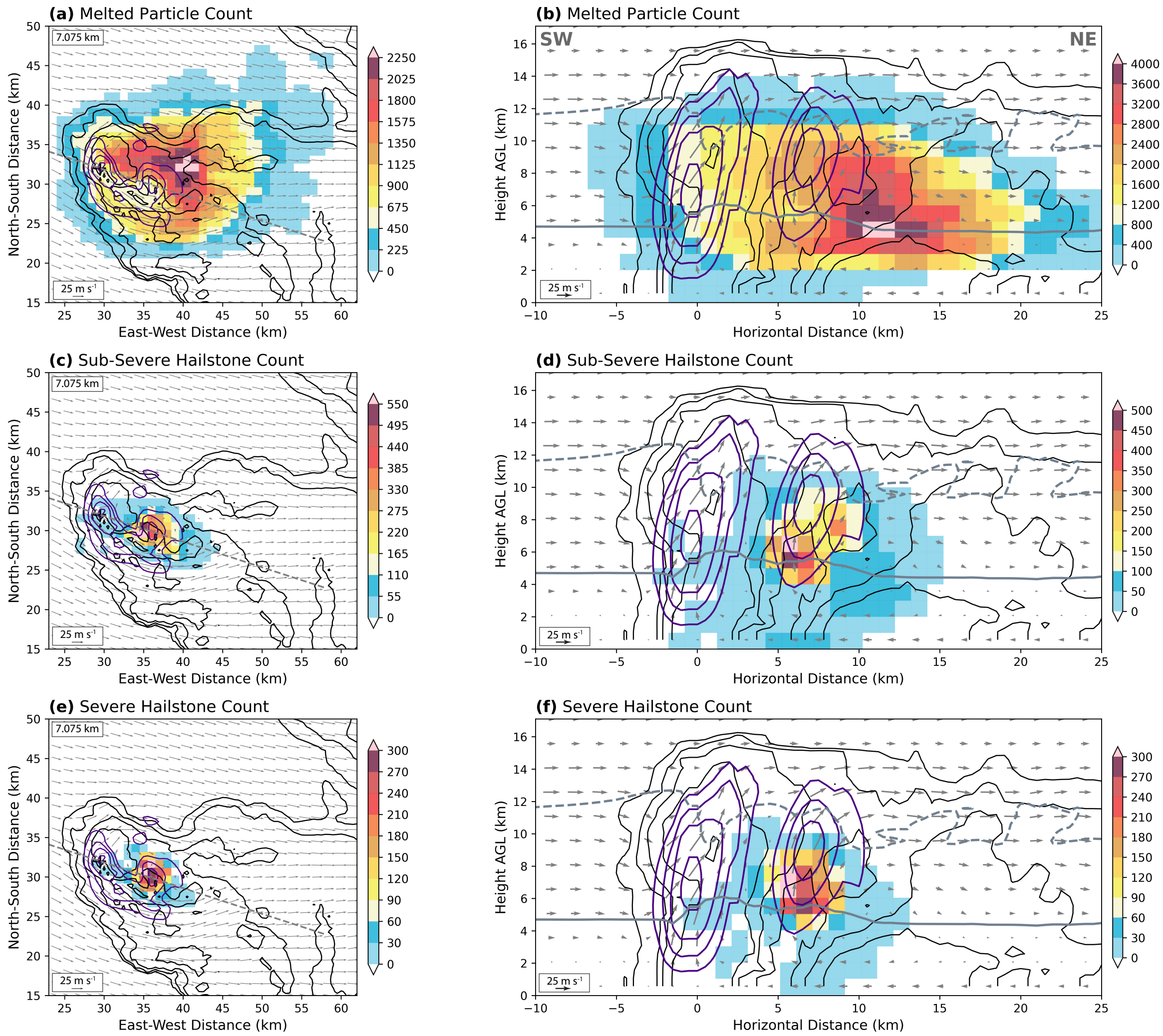


**Figure 11.** As in Figure 6, but 2306 UTC.

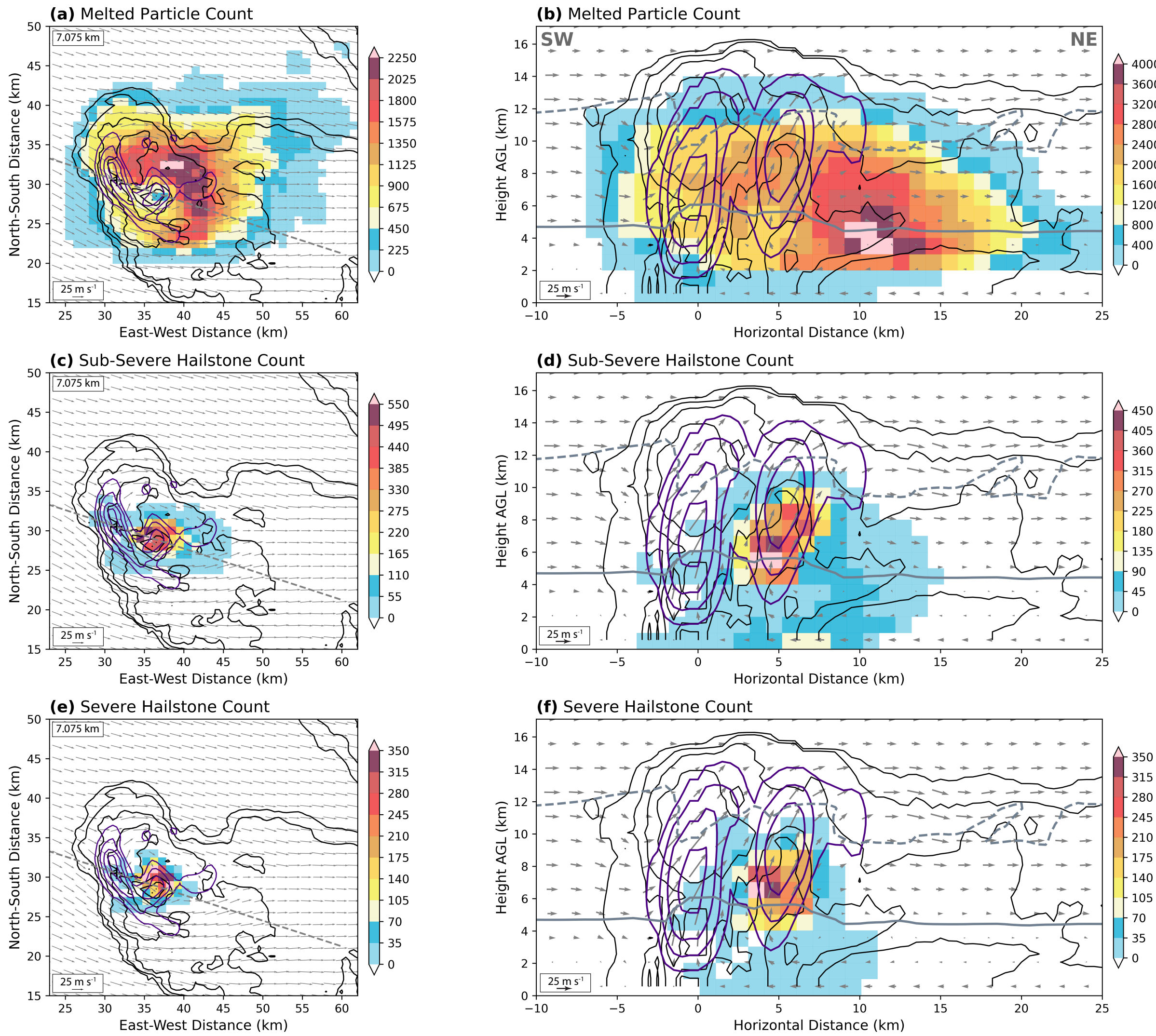


**Figure 12.** As in Figure 6, but 2309 UTC.

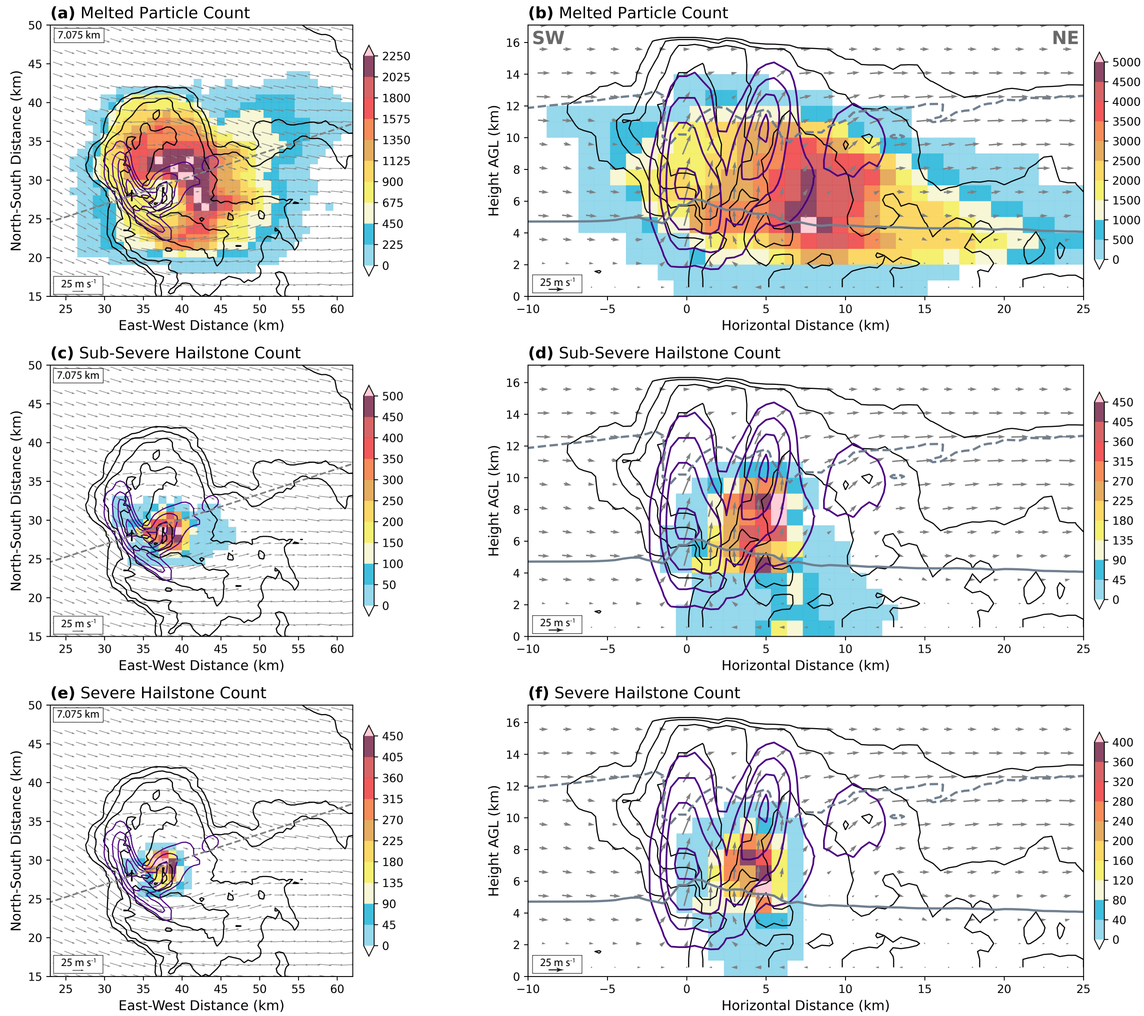


**Figure 13.** As in Figure 6, but 2312 UTC.

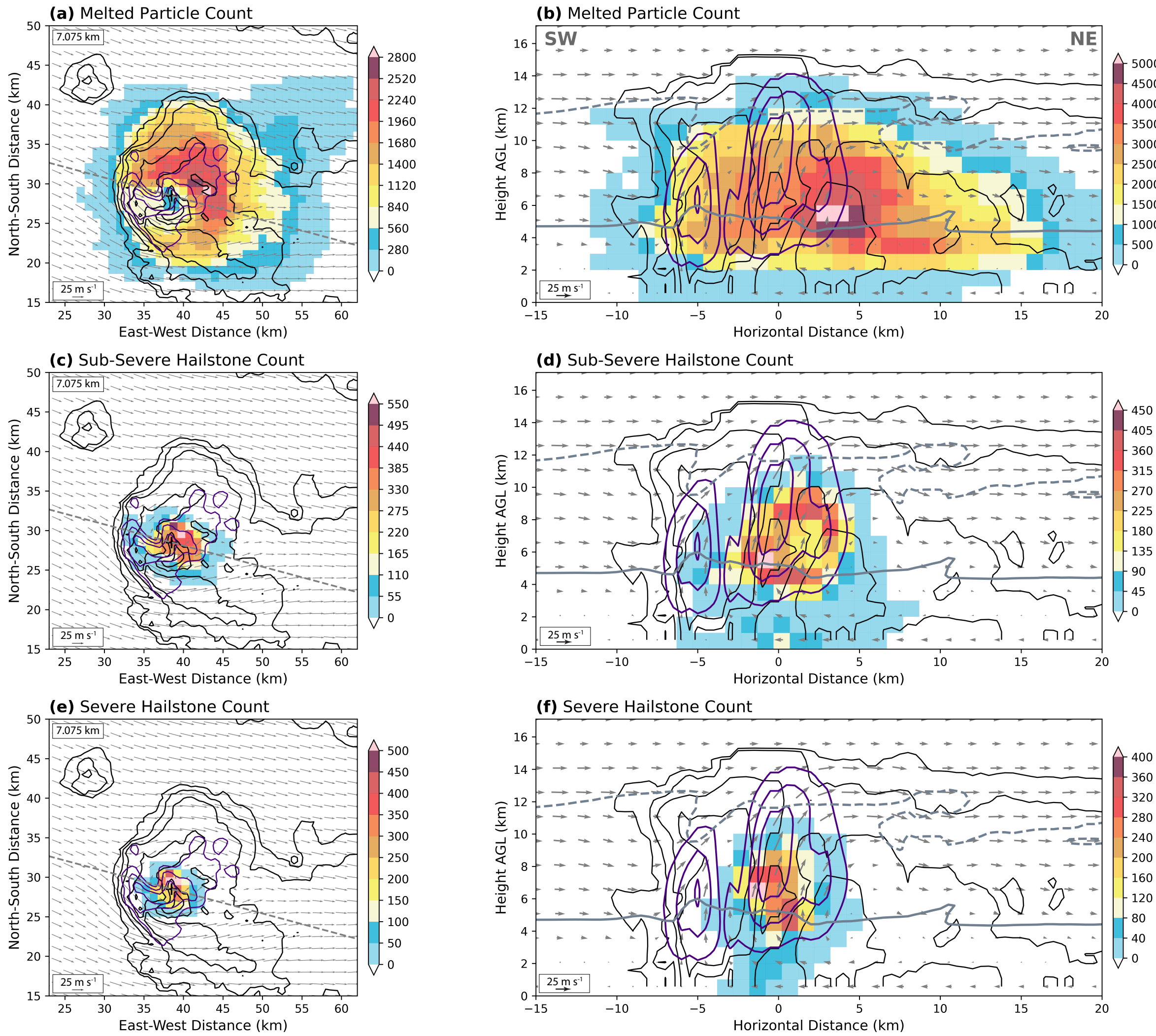


**Figure 14.** As in Figure 6, but 2315 UTC.

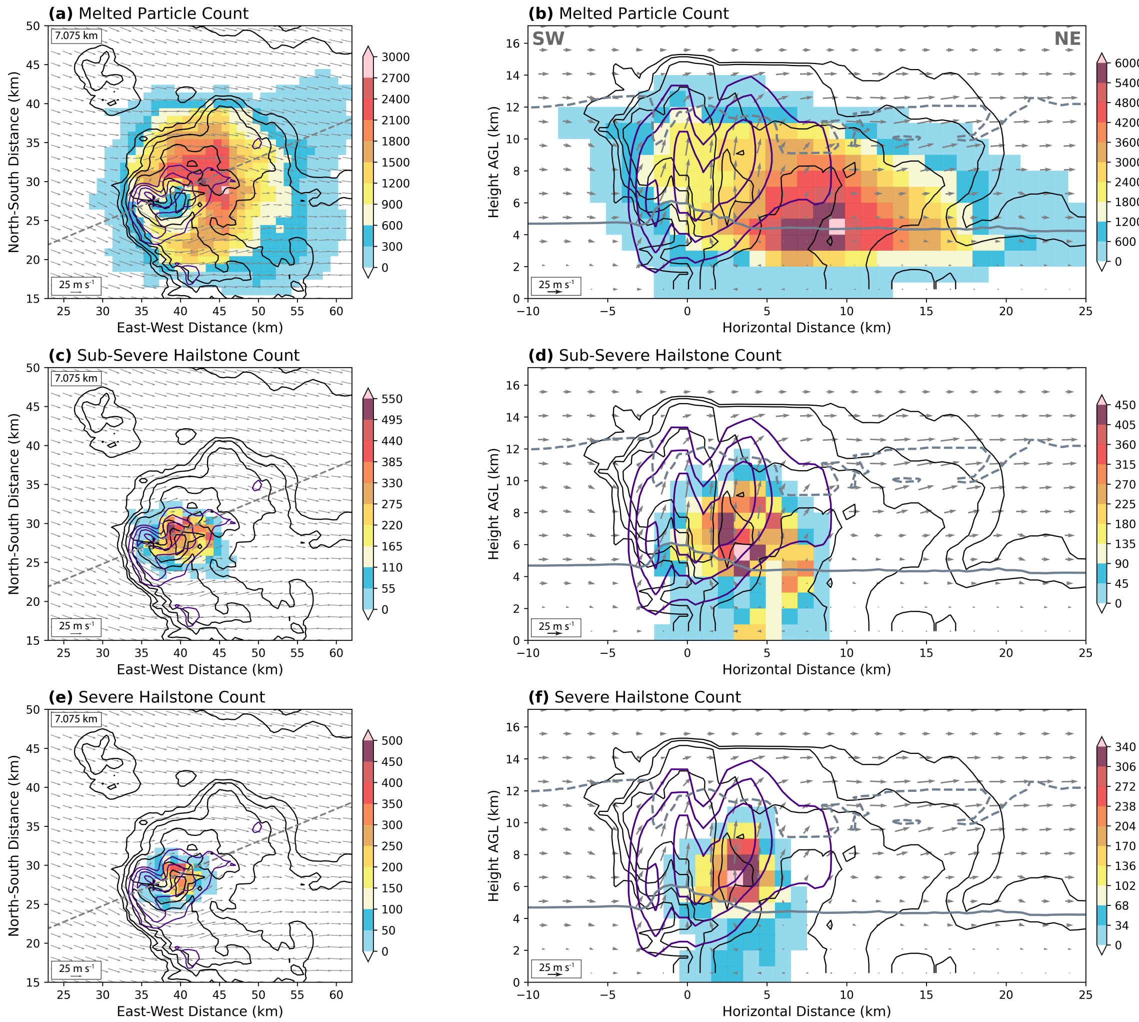


**Figure 15.** As in Figure 6, but 2318 UTC.

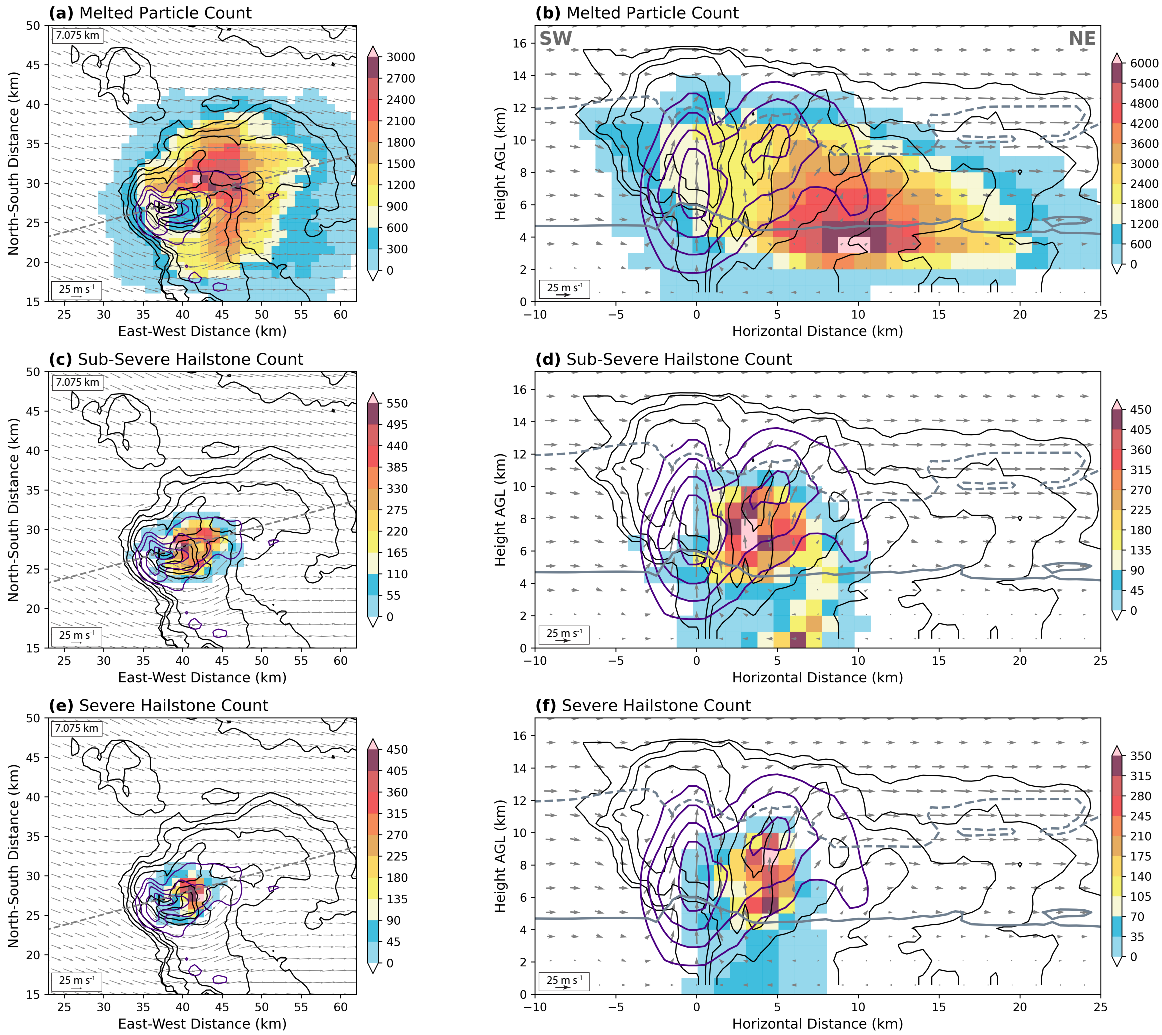


**Figure 16.** As in Figure 6, but 2321 UTC.

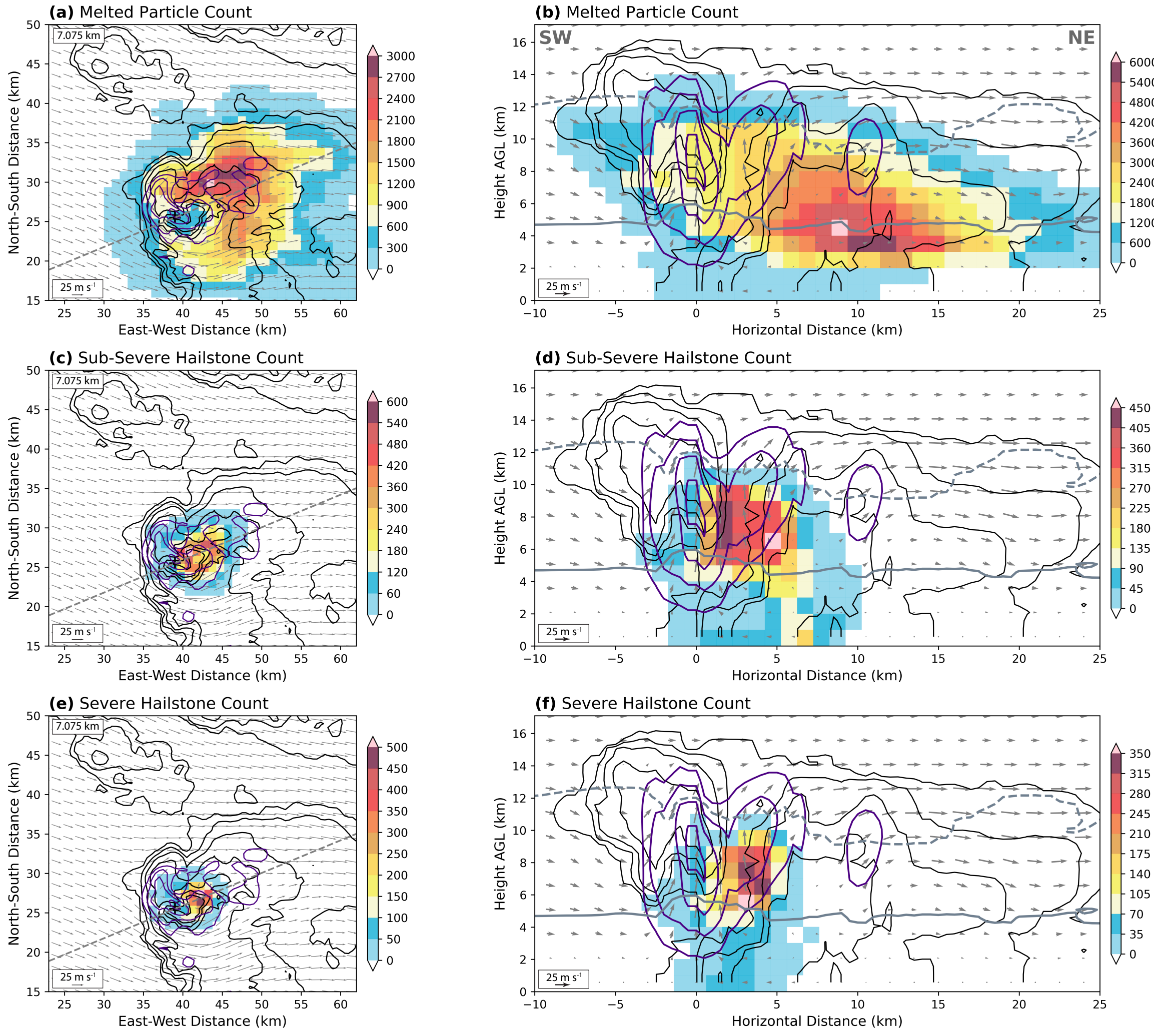


**Figure 17.** As in Figure 6, but 2324 UTC.

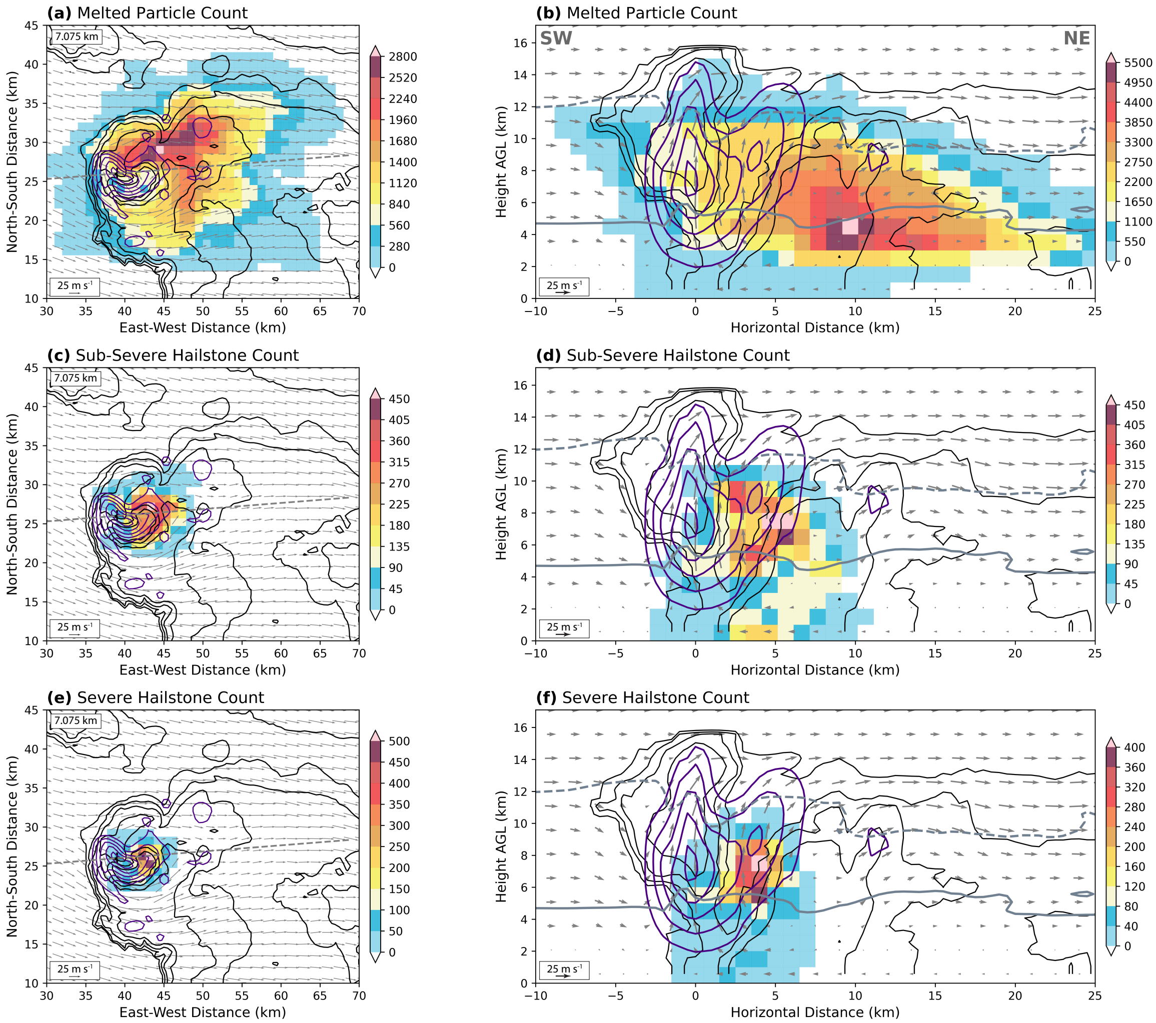


**Figure 18.** As in Figure 6, but 2327 UTC.

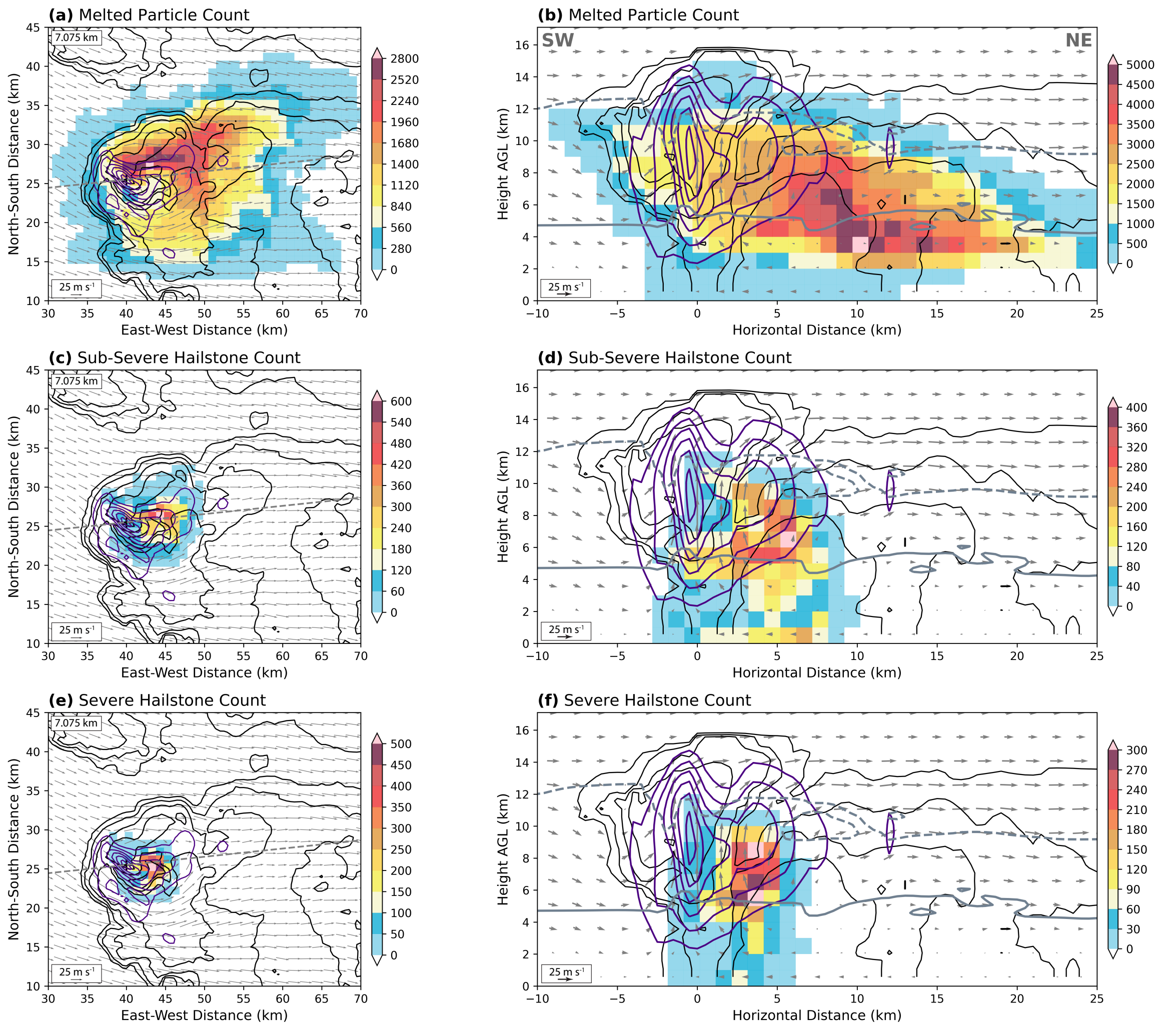


Figure 19. As in Figure 6, but 2330 UTC.

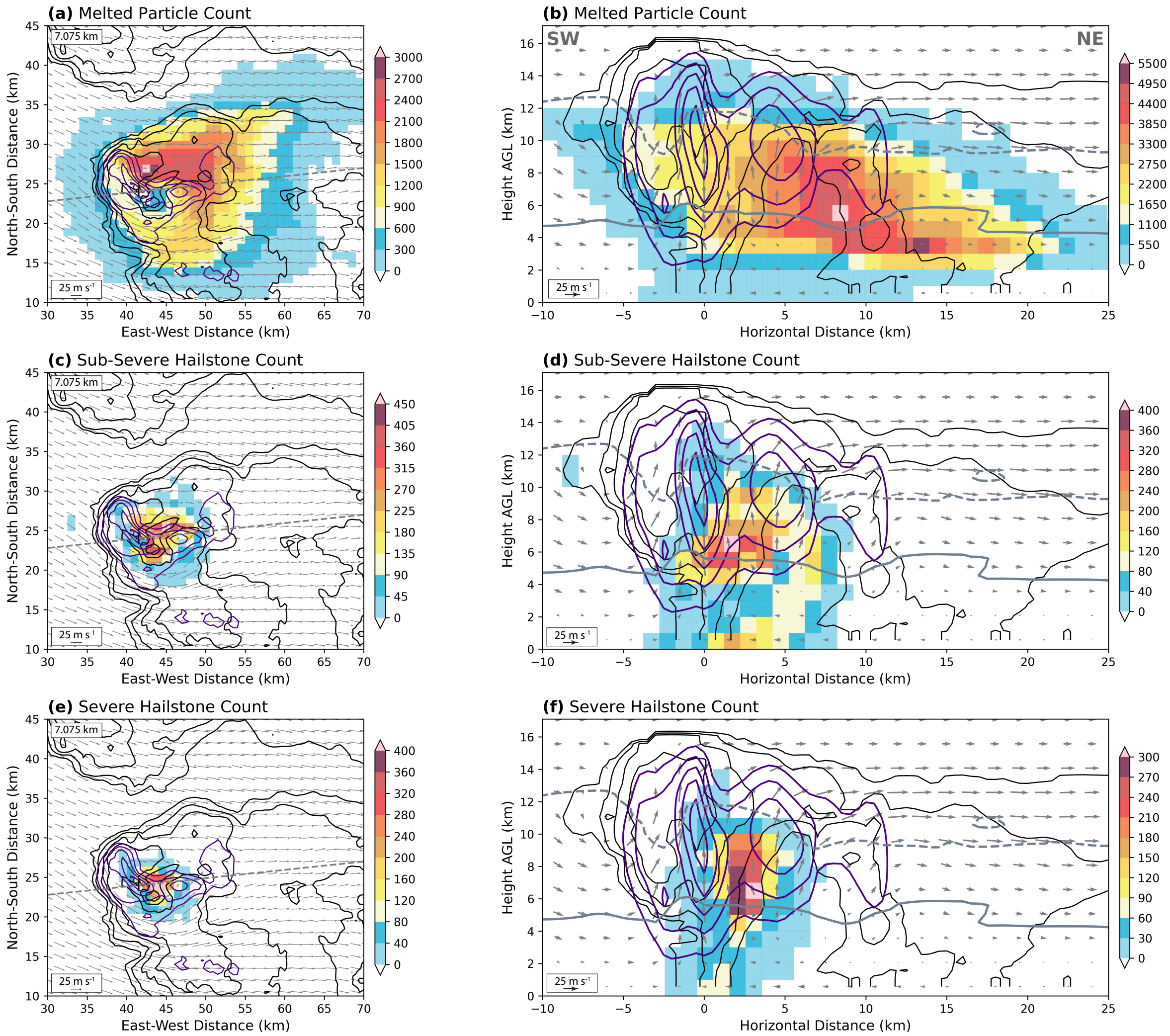


**Figure 20.** Same as in Figure 6, but 2333 UTC.

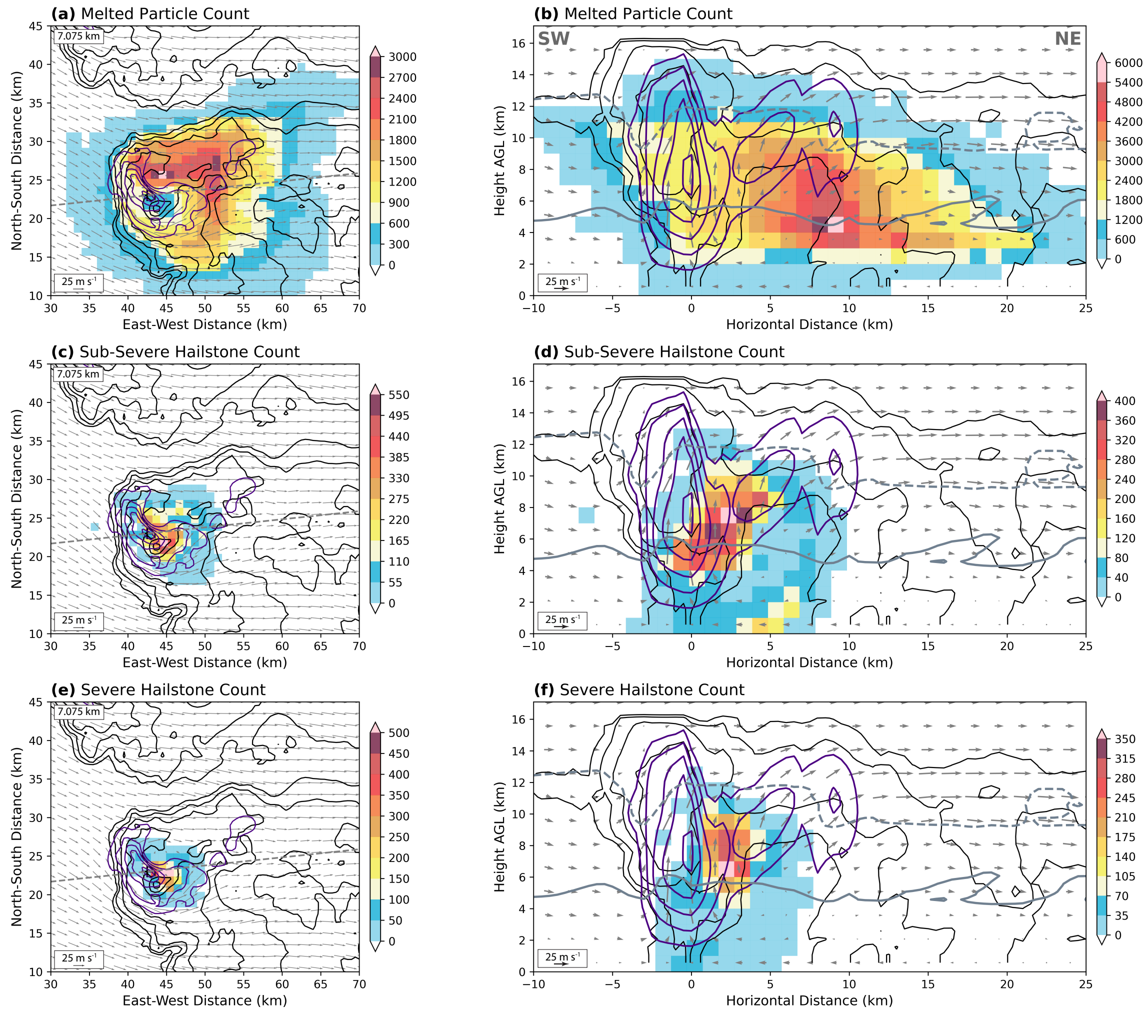


**Figure 21.** Same as in Figure 6, but 2336 UTC.

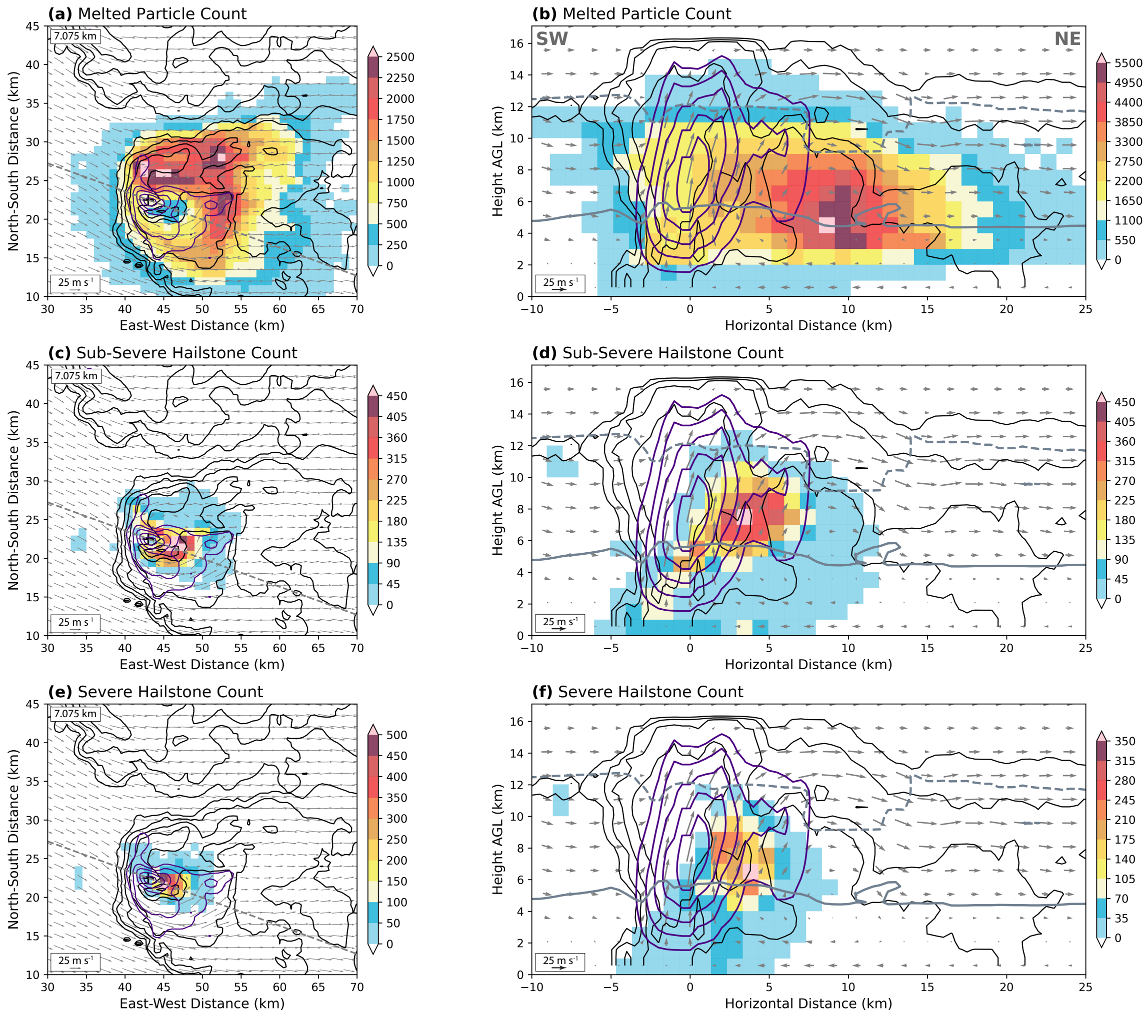


**Figure 22.** Same as in Figure 6, but 2339 UTC.

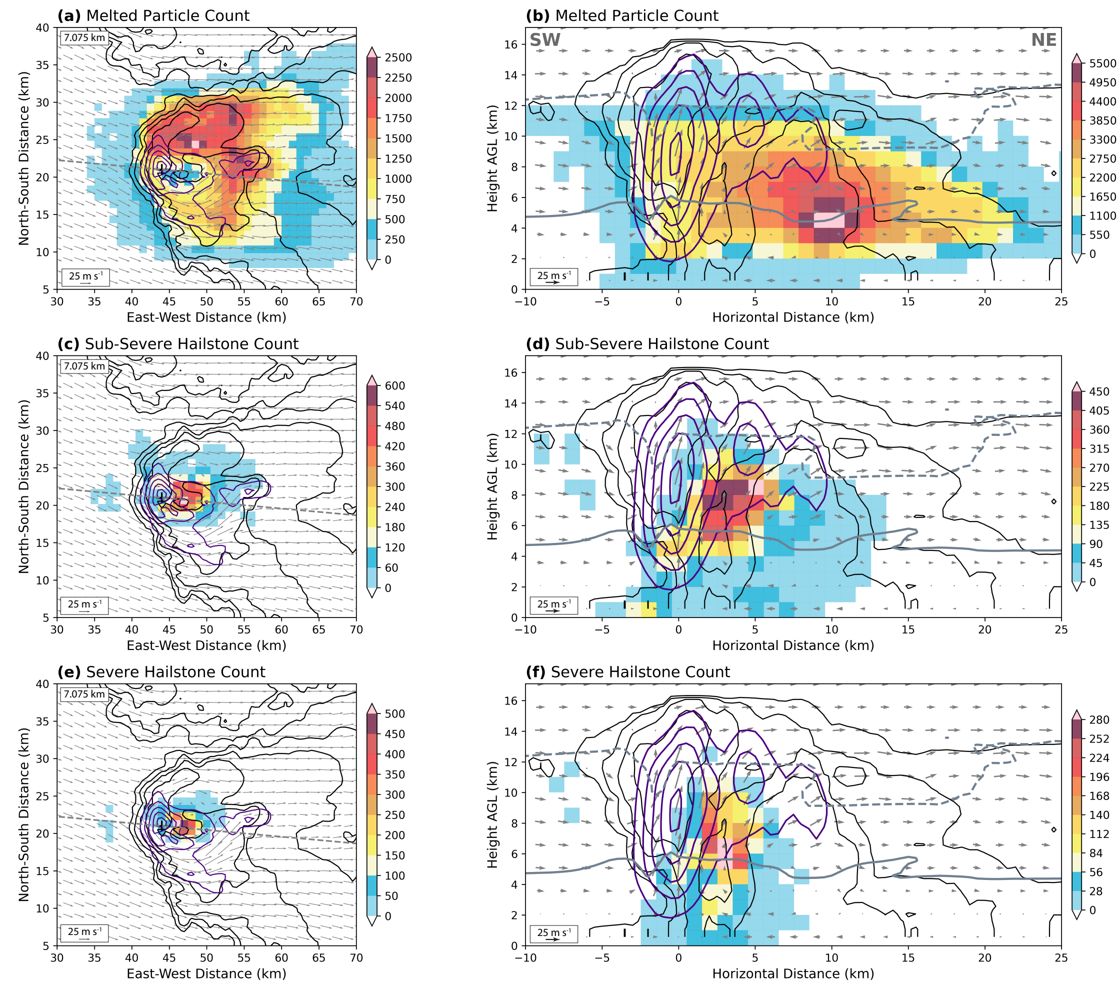


**Figure 23.** Same as in Figure 6, but 2342 UTC.

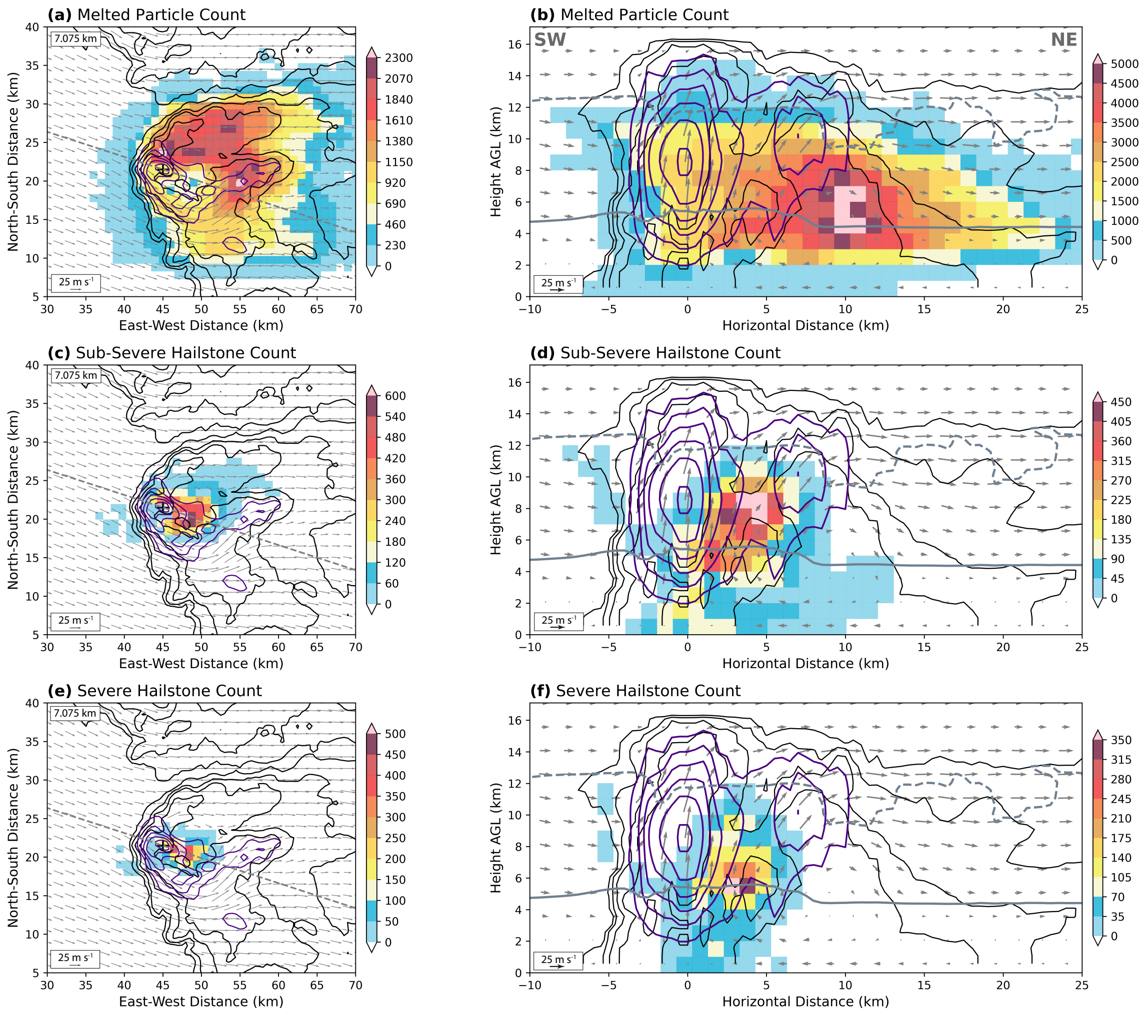


**Figure 24.** Same as in Figure 6, but 2345 UTC.

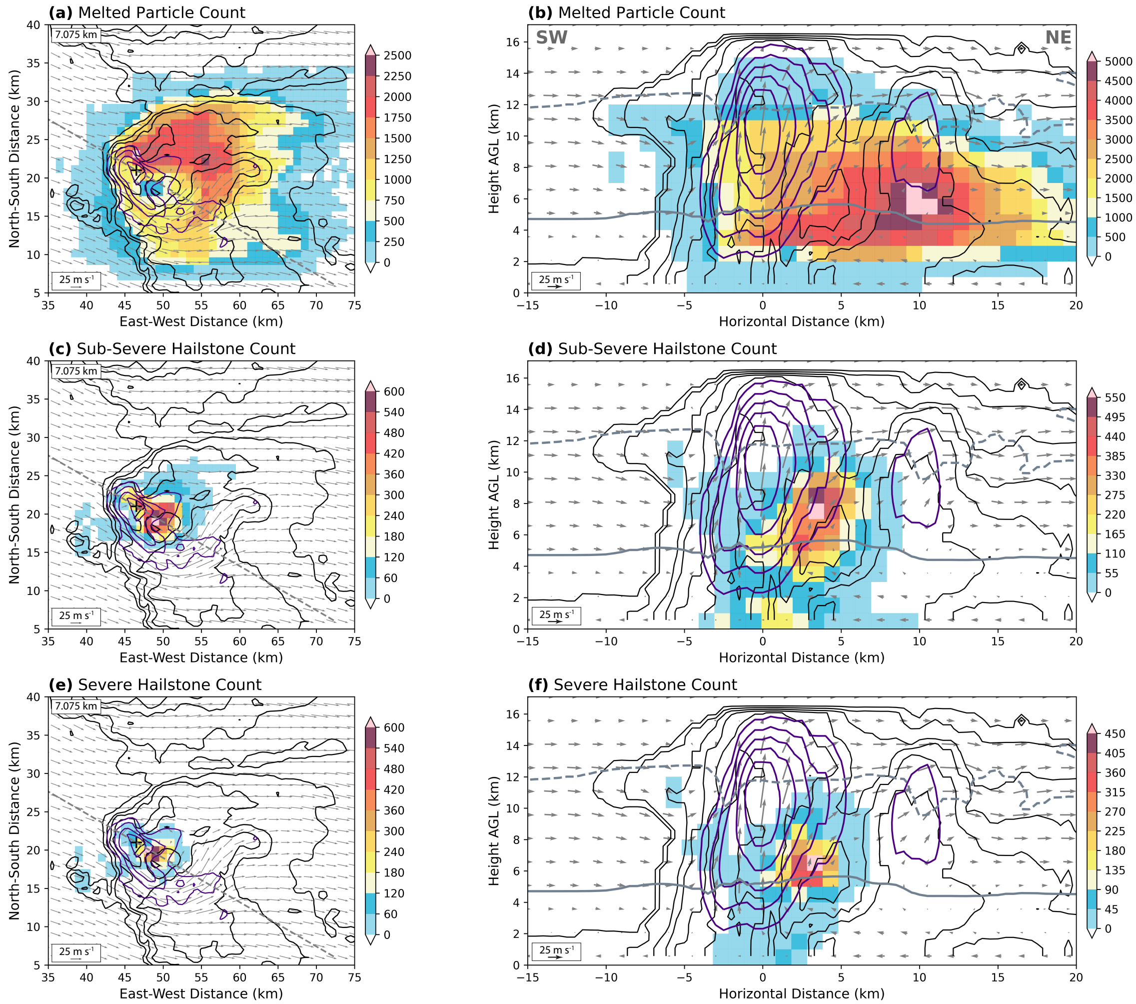


**Figure 25.** Same as in Figure 6, but 2348 UTC.

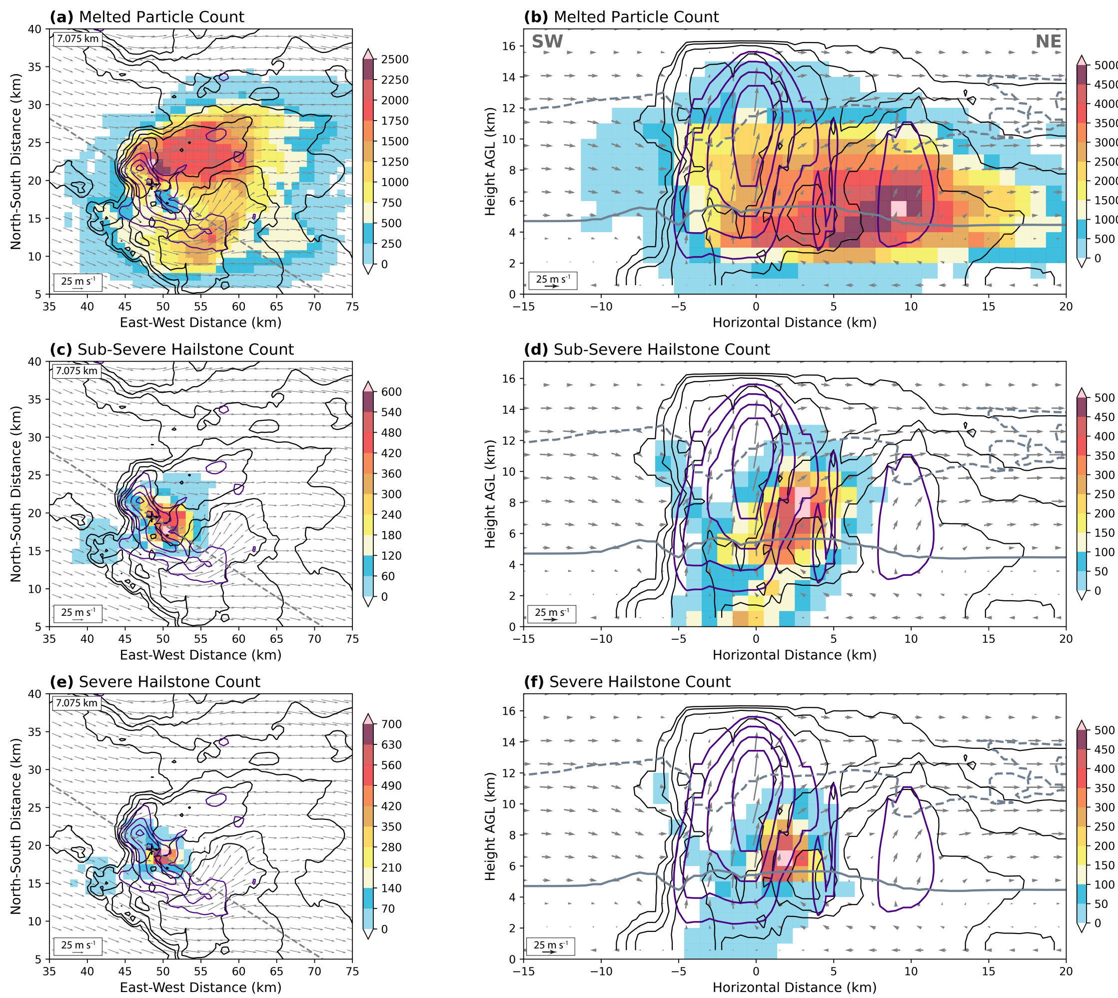


**Figure 26.** Same as in Figure 6, but 2351 UTC.

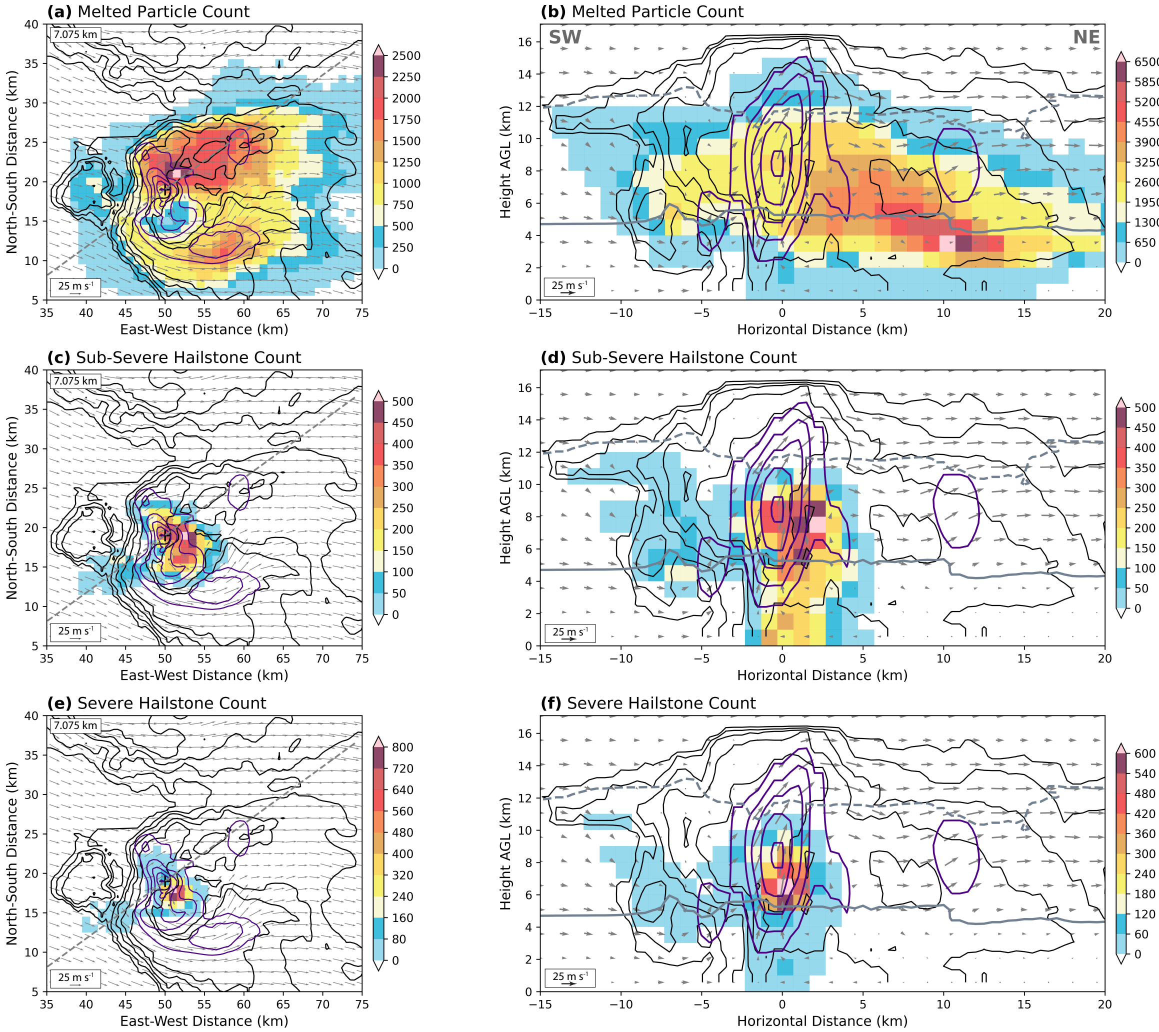


**Figure 27.** Same as in Figure 6, but 2354 UTC.

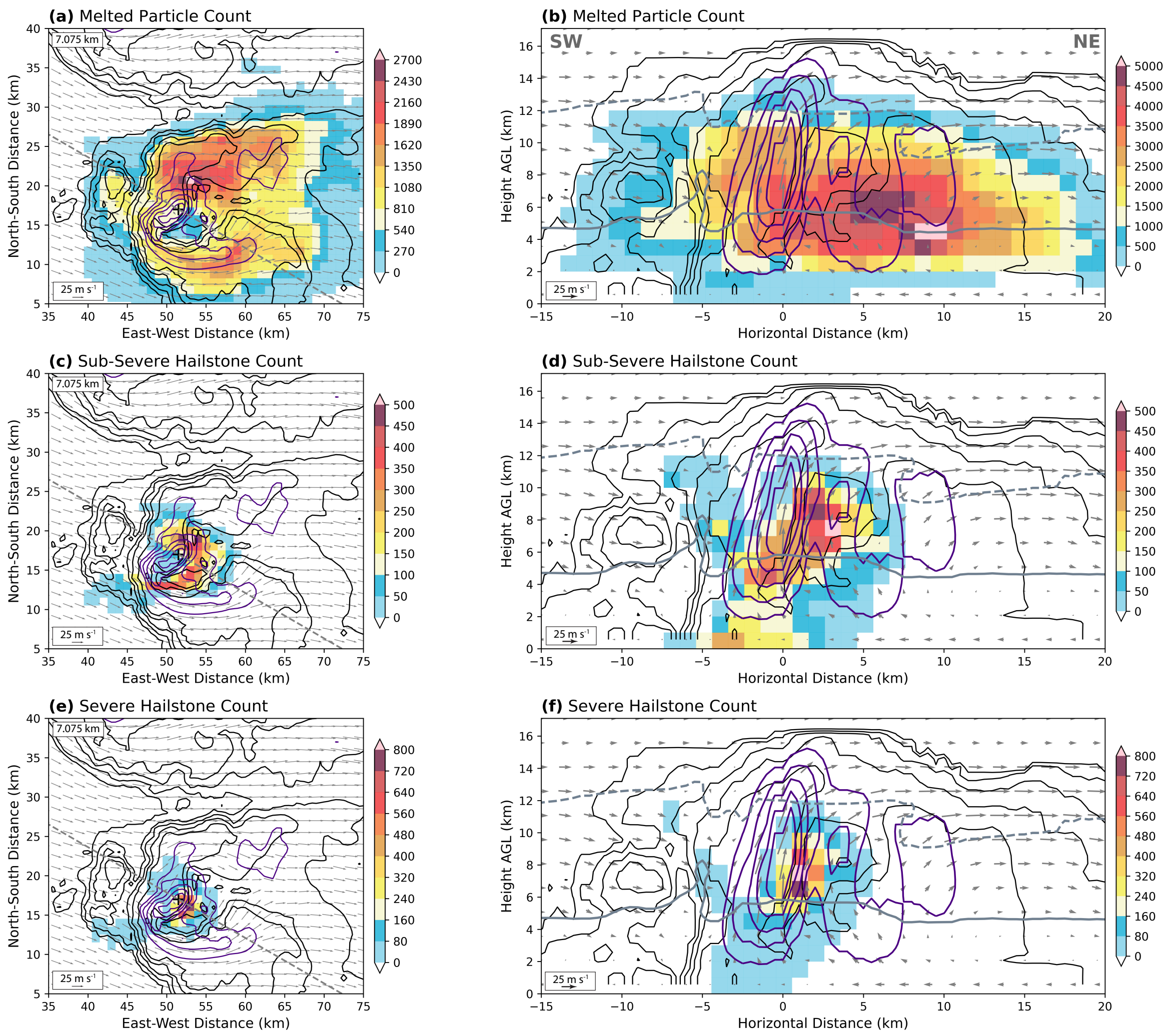


**Figure 28.** Same as in Figure 6, but 2357 UTC.

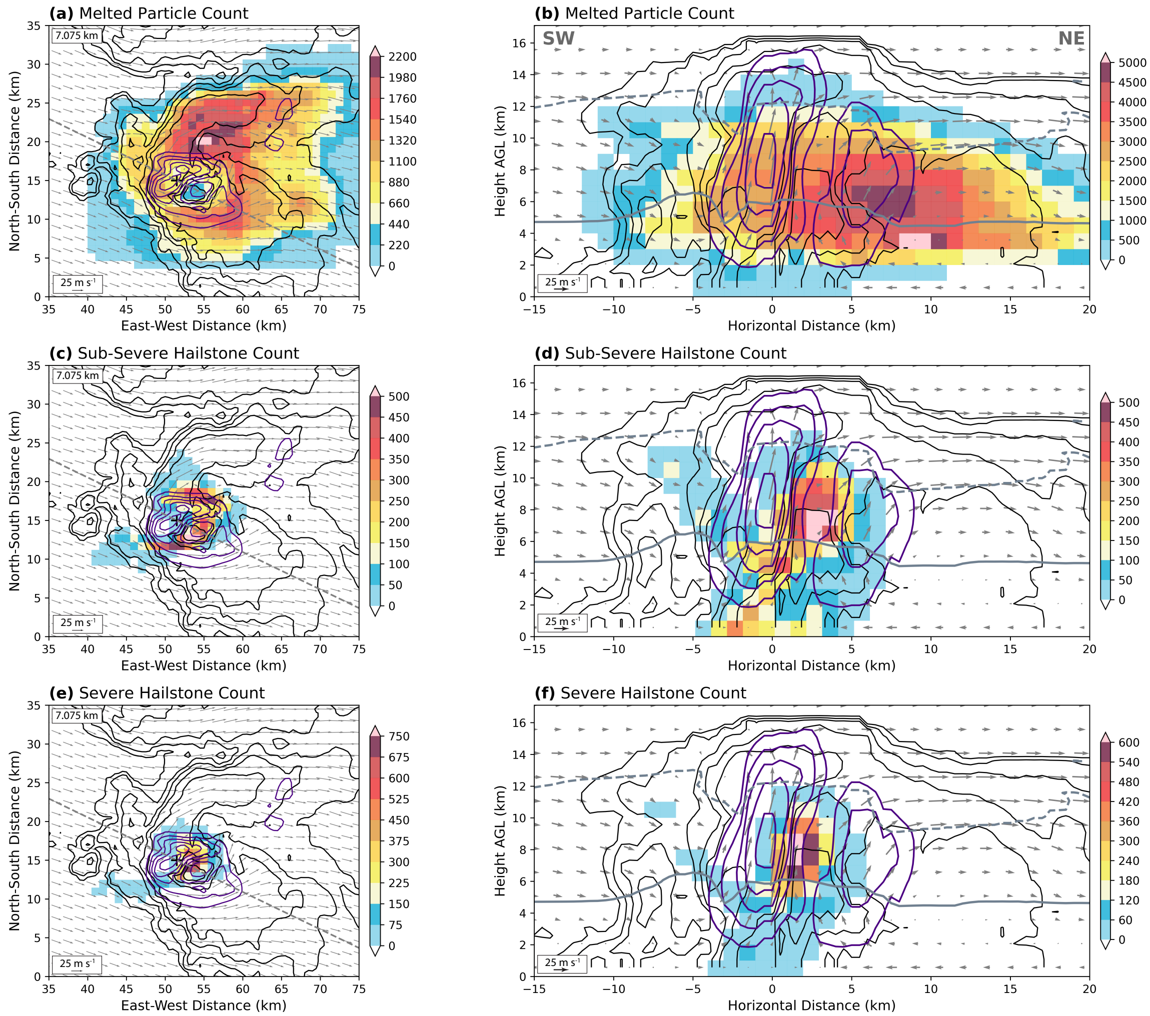


**Figure 29.** Same as in Figure 6, but 0000 UTC.

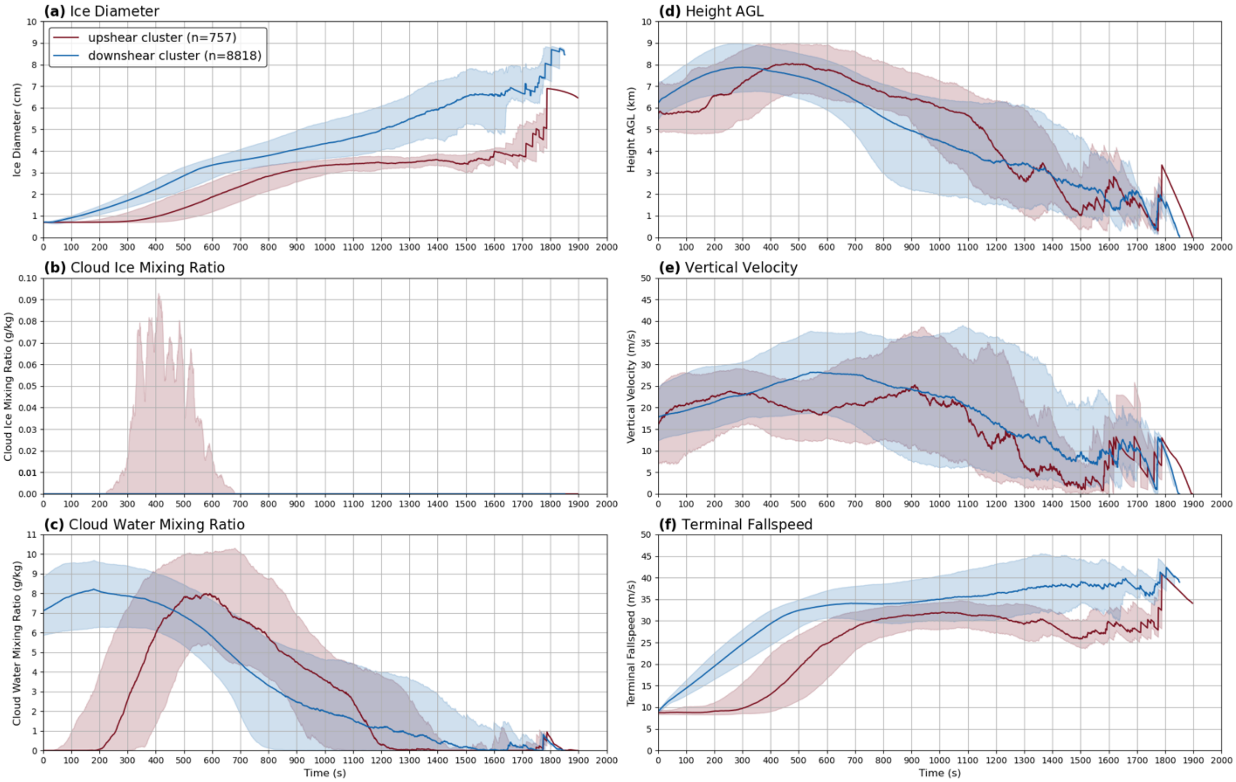


**Figure 30.** Upshear (SW) cluster (red) and downshear (SE) cluster (blue) environmental characteristics time series of severe hailstones from 2339 UTC – 0000 UTC (7 total analysis times). The solid lines represent the mean of all severe hailstones in the cluster. The shaded region are the values between the 25th and 75th percentiles. Environmental characteristics shown are: a) ice diameter (cm), b) cloud ice mixing ratio (g $kg^{-1}$), c) cloud water mixing ratio (g $kg^{-1}$), d) height (km), e) vertical velocity (m $s^{-1}$), and f) terminal velocity (m $s^{-1}$).

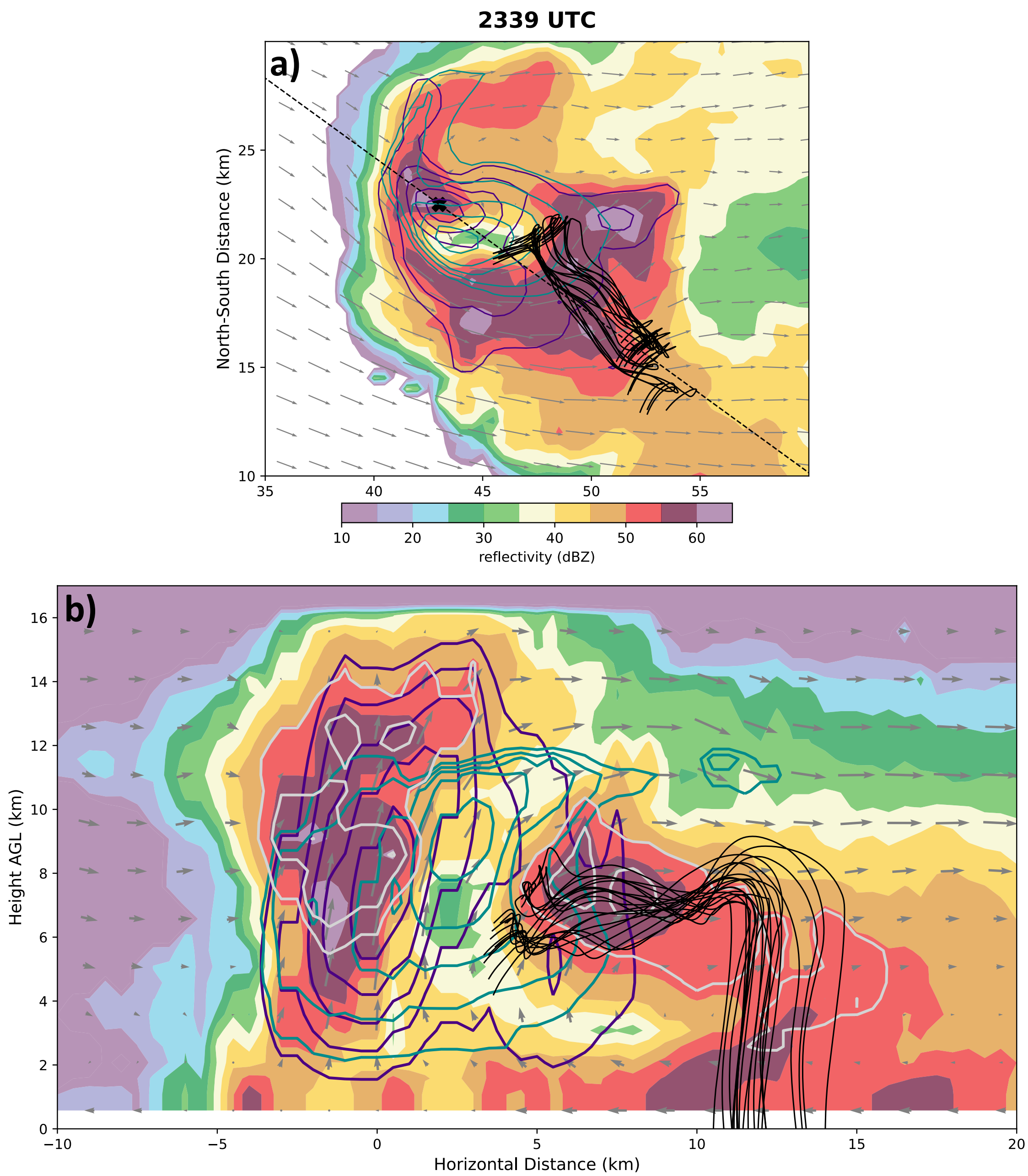


**Figure 31.** DLA and radar analysis fields at 2339 UTC overlaid with the 20 largest hail trajectories (ranging from ~8 cm – ~10 cm in diameter at surface) resultant from embryos initialized at 2339 UTC, shown by solid black lines. The colorfill is reflectivity shown beginning at 10 dBZ contoured in 5 dBZ increments up to 65 dBZ, with the colorscale as denoted by the colorbar. Contours are graupel/hail mixing ratio at 2 g kg$^{-1}$ intervals beginning with 2 g kg$^{-1}$ (grey), vertical velocity at 10 m s$^{-1}$ intervals beginning with 10 m s$^{-1}$ (purple), and cloud water mixing ratio at 2 g kg$^{-1}$ intervals beginning with 2 g kg$^{-1}$ (green). Contours are shown at a) 7.075 km and within b) the cross section indicated by the black dotted line in a) passing through the updraft maximum as indicated by the black "x".

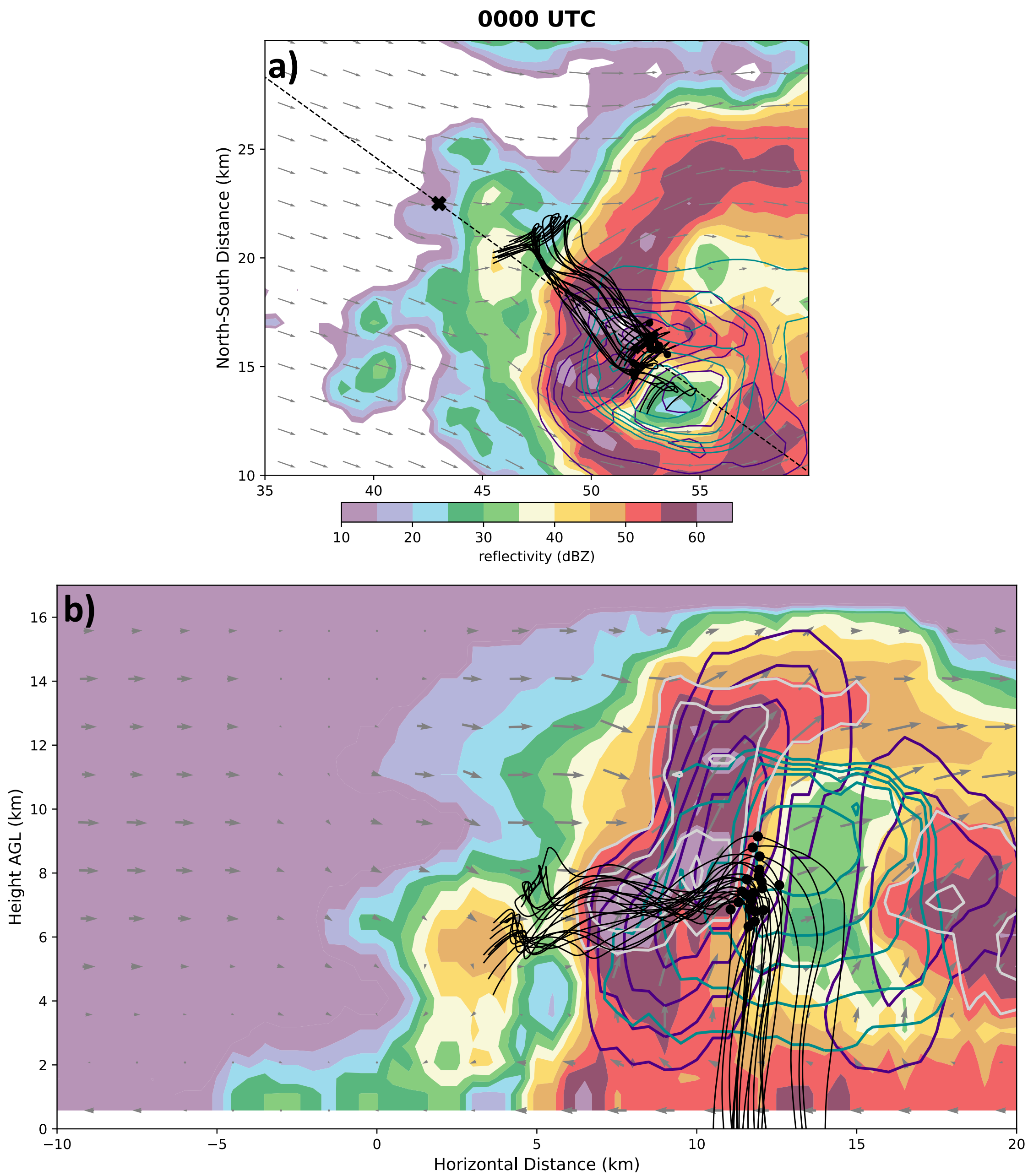


**Figure 32.** DLA and radar analysis fields at 0000 UTC overlaid with the 20 largest hail trajectories (ranging from ~8 cm – ~10 cm in diameter at surface) resultant from embryos initialized at 2339 UTC, shown by solid black lines. The colorfill is reflectivity shown beginning at 10 dBZ contoured in 5 dBZ increments up to 65 dBZ, with the colorscale as denoted by the colorbar. Contours are graupel/hail mixing ratio at 2 g kg$^{-1}$ intervals beginning with 2 g kg$^{-1}$ (grey), vertical velocity at 10 m s$^{-1}$ intervals beginning with 10 m s$^{-1}$ (purple), and cloud water mixing ratio at 2 g kg$^{-1}$ intervals beginning with 2 g kg$^{-1}$ (green). Contours are shown at a) 7.075 km and within b) the cross section indicated by the black dotted line in a) passing through the updraft maximum as indicated by the black "x". Additionally, the black dots represent the location of each hailstone along their trajectory at 0000 UTC.

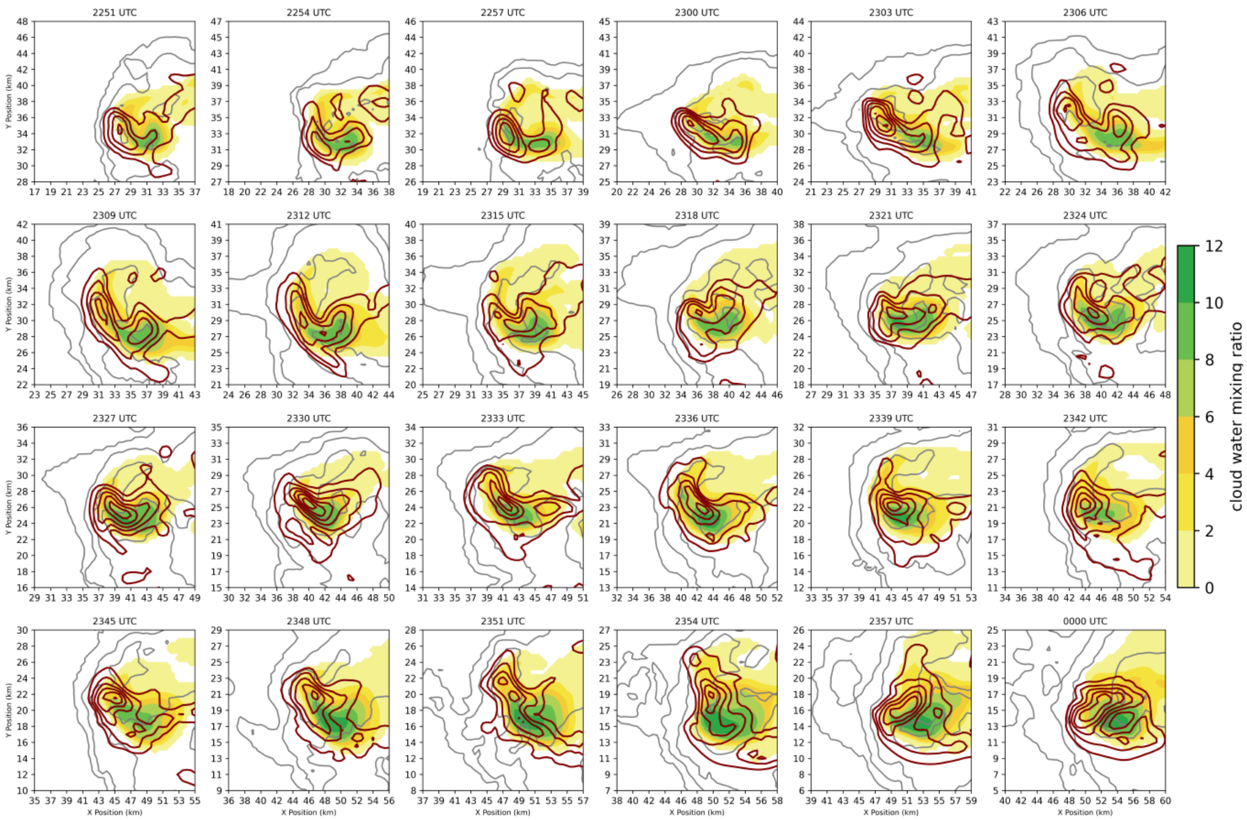

**Figure 33.** Embryo domain (20 km x 20 km) for all 24 analysis times between 29 May 2251 UTC and 30 May 0000 UTC. Red contours are vertical velocity at 10 m s$^{-1}$ beginning at 10 m s$^{-1}$ intervals and gray contours are reflectivity contoured at 20 dBZ intervals beginning at 10 dBZ. The shaded regions are $q_c$ contoured at 1 g kg$^{-1}$ intervals from 0 g kg$^{-1}$ to 12 g kg$^{-1}$.

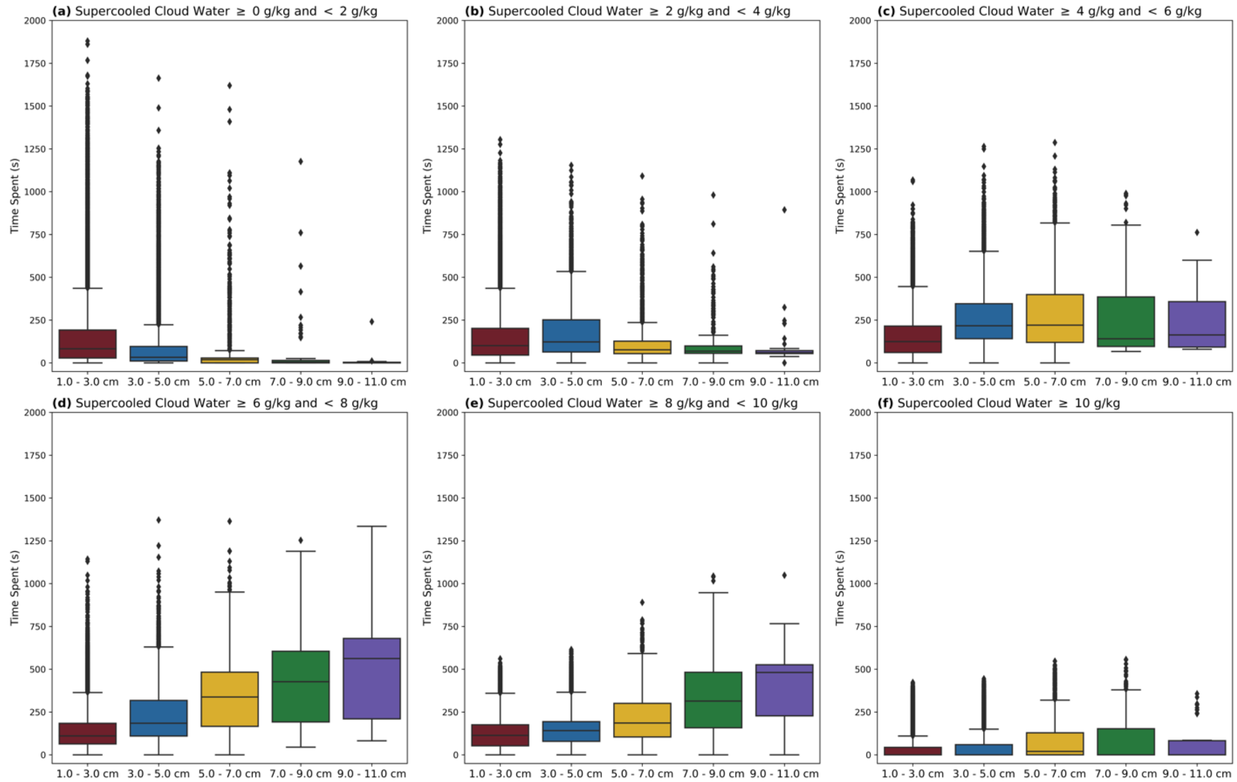


**Figure 34**. Time (s) hailstones spend within a given range of values of supercooled cloud water: a) $\geq 0$ g kg$^{-1}$ and $< 2$ g kg$^{-1}$, b) $\geq 2$ g kg$^{-1}$ and $< 4$ g kg$^{-1}$, c) $\geq 4$ g kg$^{-1}$ and $< 6$ g kg$^{-1}$, d) $\geq 6$ g kg$^{-1}$ and $< 8$ g kg$^{-1}$, e) $\geq 8$ g kg$^{-1}$ and $< 10$ g kg$^{-1}$, f) $\geq 10$ g kg$^{-1}$. Hailstones from 2251 UTC – 0000 UTC are included if their final diameter at the surface was at least 1 cm. Five different size bins are used: 1 cm – 2 cm (red), 2 cm – 3 cm (blue), 3 cm – 4 cm (yellow), 4 cm – 5 cm (green), and 5 cm – 6 cm (purple). Color filled area denotes the inter-quartile range, or the points between the first quartile (upper) and third quartile (lower) of the data. The black line within the color fill is the median of the data. The whiskers represent 1.5x the inter-quartile range. Solid diamonds represent outliers, or points which reside outside of the whiskers.

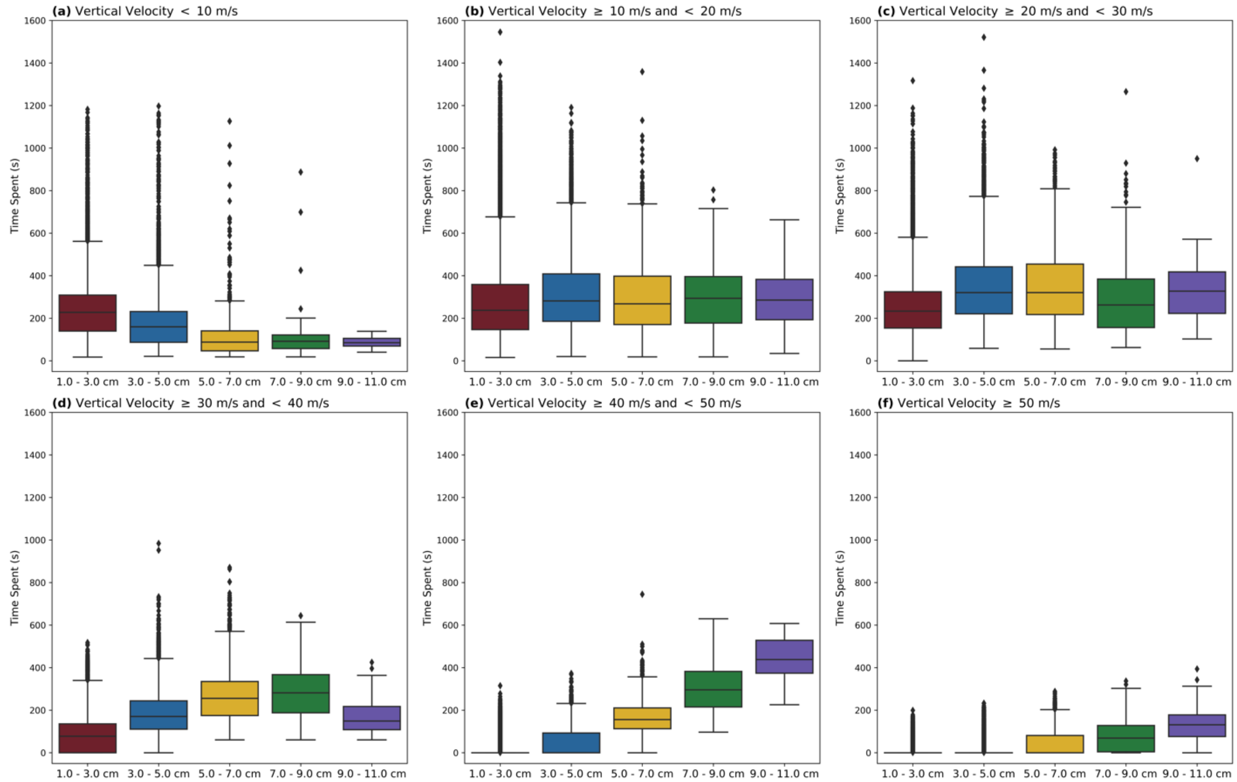


**Figure 35**. Time (s) hailstones spend within a given range of values of vertical velocities: a) $\geq 0$ m $s^{-1}$ and $< 10$ m $s^{-1}$, b) $\geq 10$ m $s^{-1}$ and $< 20$ m $s^{-1}$, c) $\geq 20$ m $s^{-1}$ and $< 30$ m $s^{-1}$, d) $\geq 30$ m $s^{-1}$ and $< 40$ m $s^{-1}$, e) $\geq 40$ m $s^{-1}$ and $< 50$ m $s^{-1}$, and f) $\geq 50$ m $s^{-1}$. Hailstones from 2251 UTC – 0000 UTC are included if their final diameter at the surface was at least 1 cm. Five different size bins are used: 1 cm – 2 cm (red), 2 cm – 3 cm (blue), 3 cm – 4 cm (yellow), 4 cm – 5 cm (green), and 5 cm – 6 cm (purple). Color filled area denotes the inter-quartile range, or the points between the first quartile (upper) and third quartile (lower) of the data. The black line within the color fill is the median of the data. The whiskers represent 1.5x the inter-quartile range. Solid diamonds represent outliers, or points which reside outside of the whiskers.

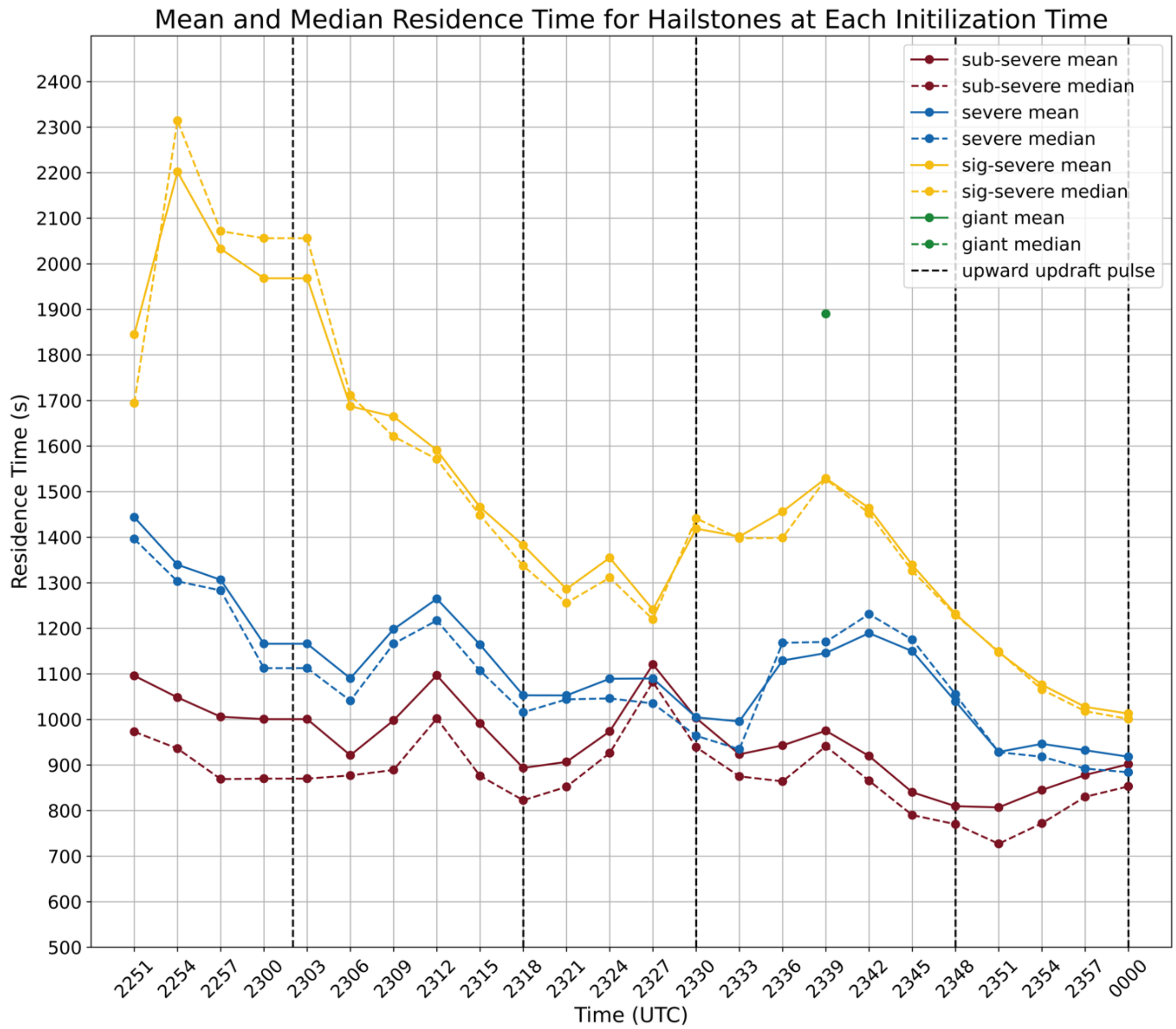


**Figure 36.** Mean (solid) and median (dashed) residence time of hailstones in each size category at every analysis time. The size categories include sub-severe (red), severe (blue), significantly severe (yellow), and giant (green).

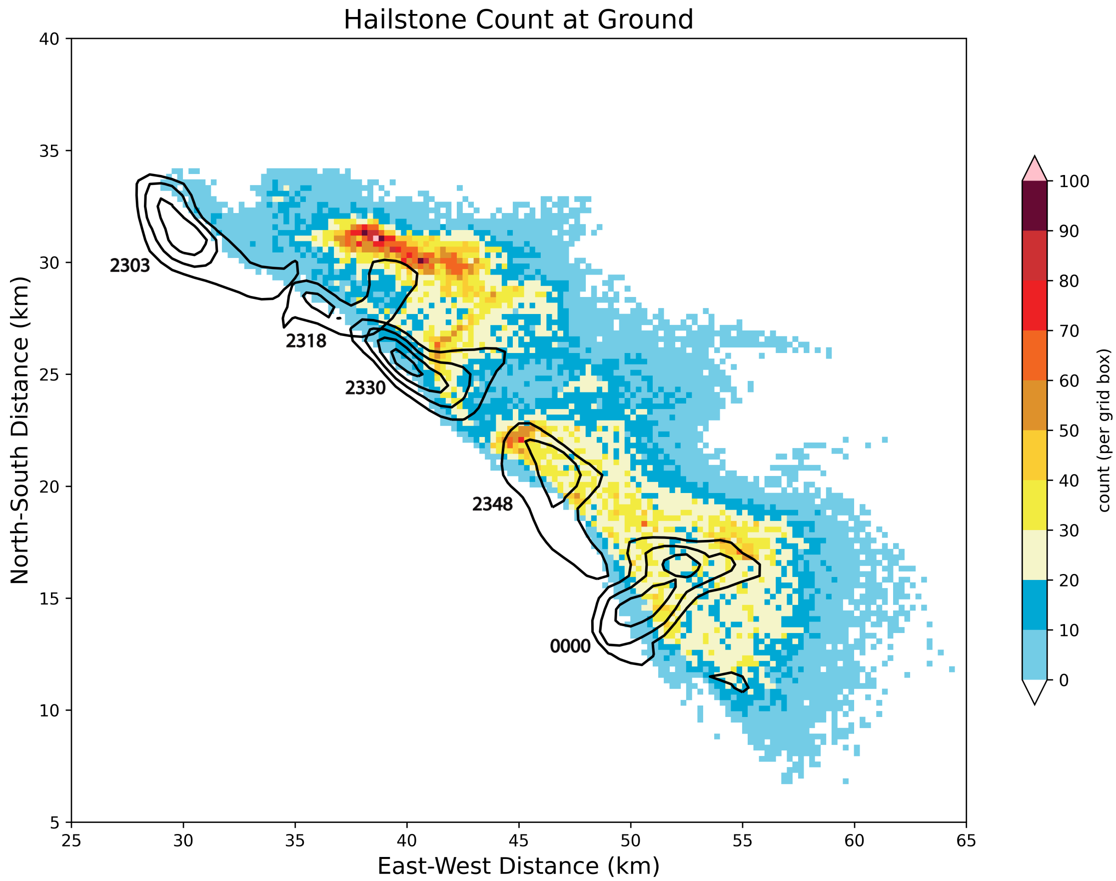


**Figure 37.** Simulated hail swath produced by all trajectories that results in a hailstone at the ground, regardless of final diameter showing hailstone count at ground in a 250 m × 250 m grid cell. Overlaid are vertical velocity contours at 7.075 km starting at 30 m $s^{-1}$ incremented by 10 m $s^{-1}$ at 2303, 2318, 2330, 2348, and 0000 UTC.

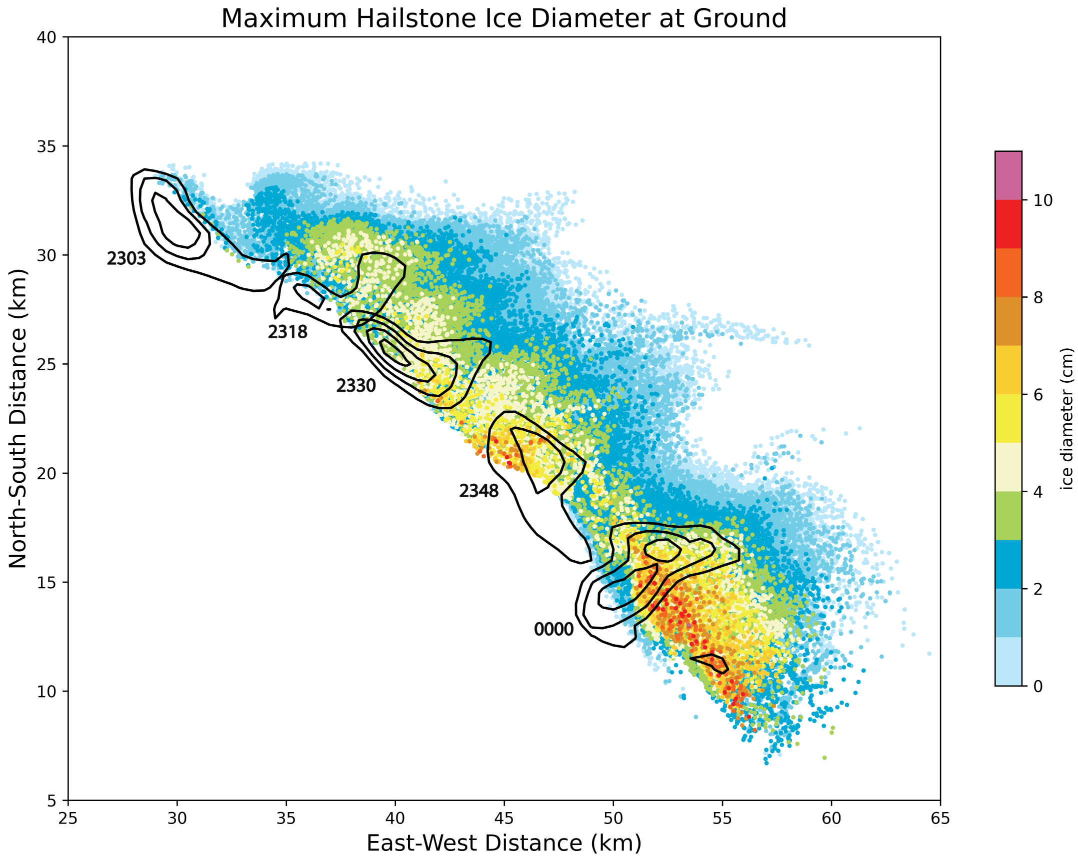


**Figure 38.** Simulated hail swath produced by all trajectories that results in a hailstone at the surface, regardless of final diameter, showing the largest hailstone in ice diameter at the surface. Overlaid are vertical velocity contours at 7.075 km starting at 30 m $s^{-1}$ incremented by 10 m $s^{-1}$ at 2303, 2318, 2330, 2348, and 0000 UTC.

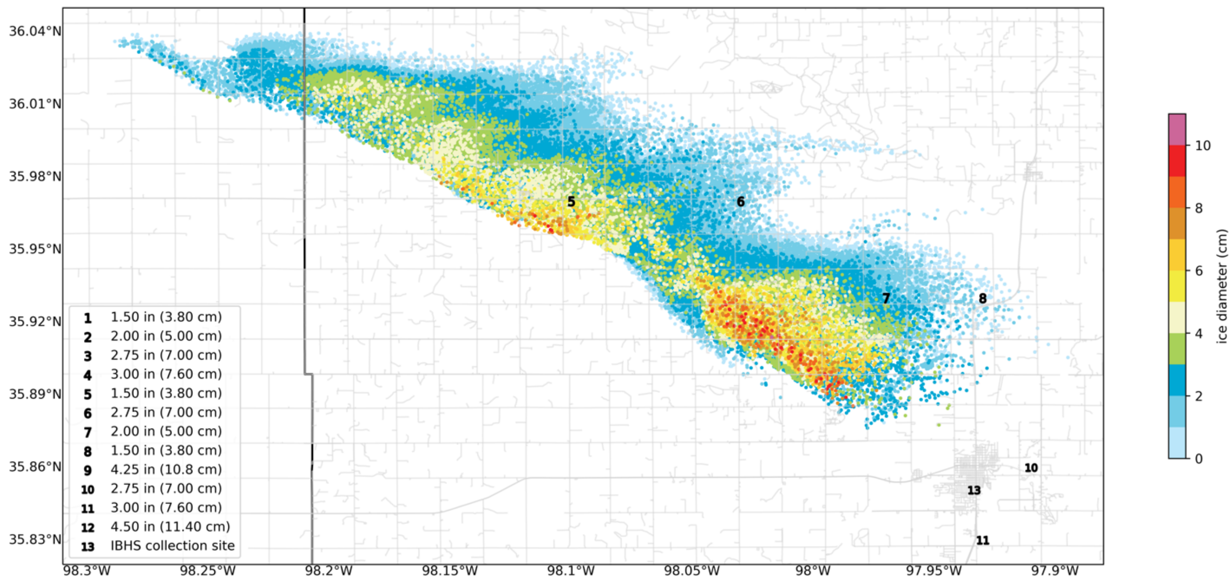


**Figure 39.** Simulated hail swath produced by all trajectories that results in a hailstone at the surface, regardless of final diameter, showing the largest hailstone in ice diameter at the surface. County boarders and roads are overlaid. LSRs associated with the Kingfisher, OK supercell reported during the analysis period are labeled by number (additional details on LSRs can be found in Table _).

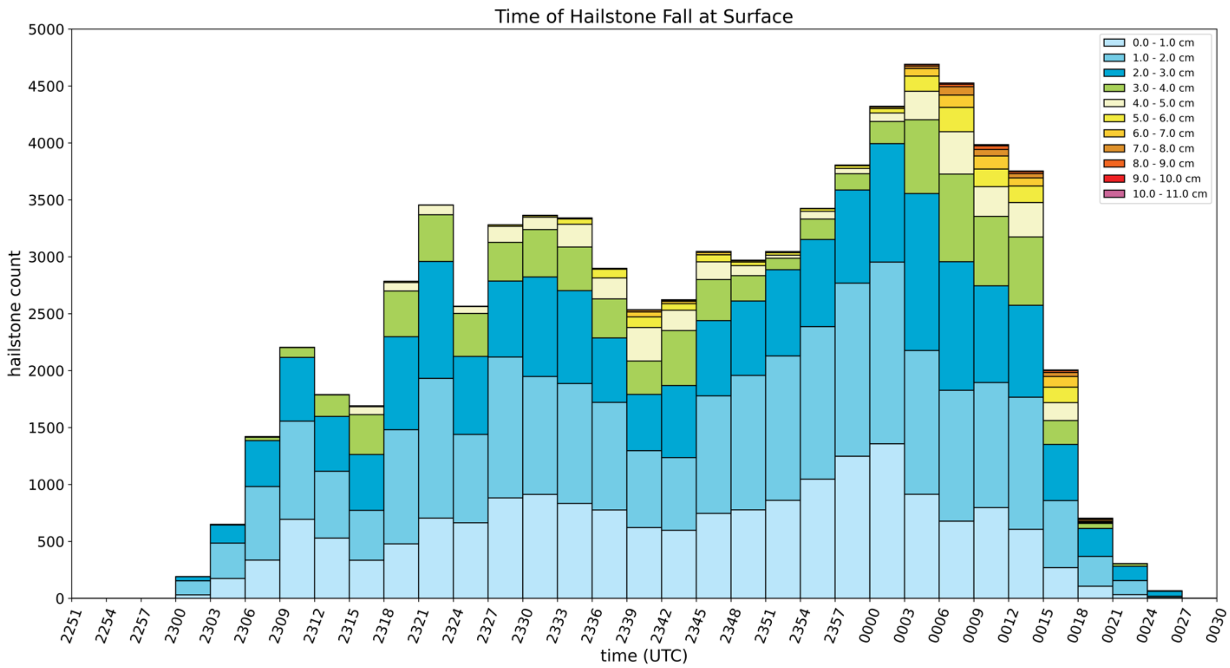


**Figure 40.** Histogram of 3-minutes time bins of when hailstones from all 24 analysis times reached the surface categorized by 1 cm size bins.

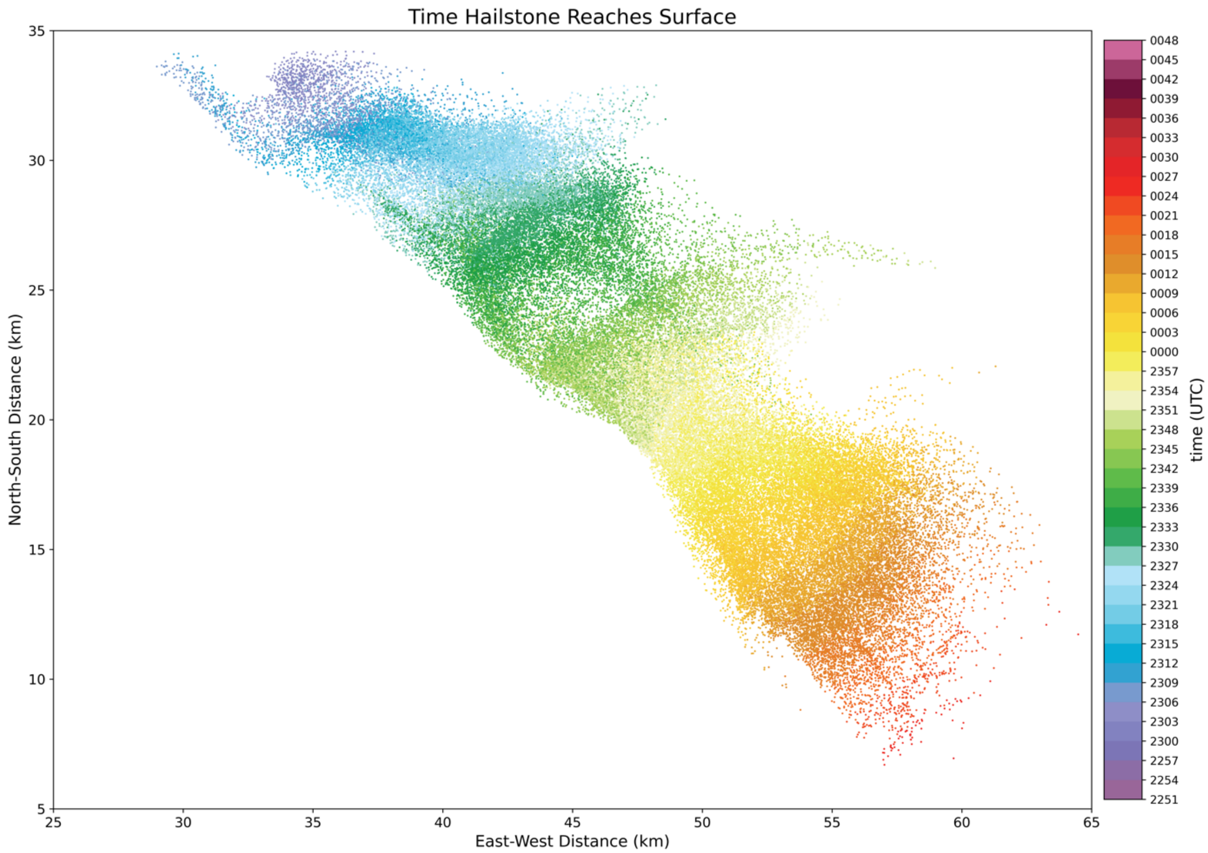


**Figure 41.** Simulated hail swath produced by all trajectories that results in a hailstone at the surface, regardless of final diameter, showing the time each hailstone fell to the surface in 3-minute interval time bins.

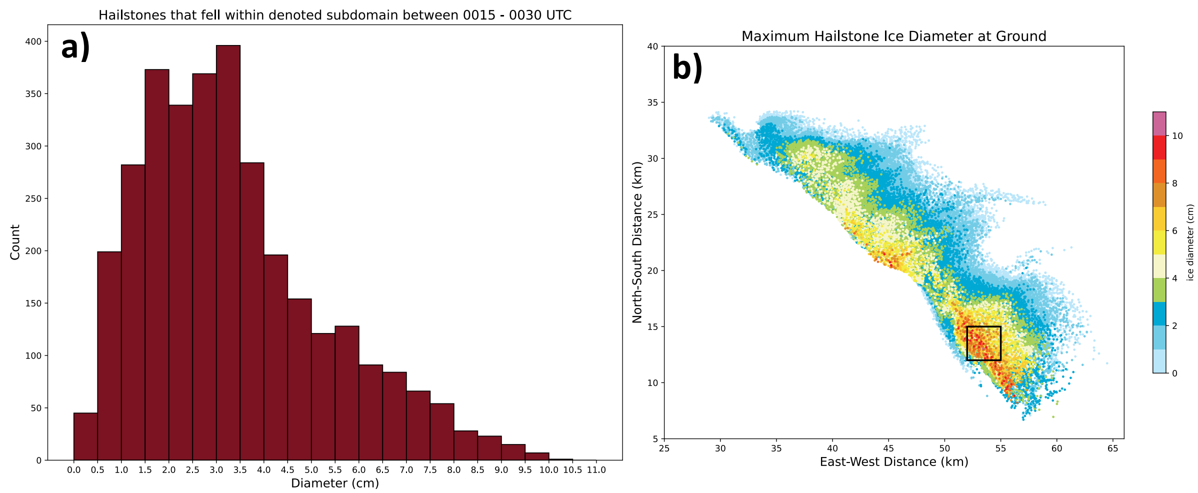


**Figure 42.** a) Histogram of hailstones in 0.5 cm bins that fell from 0015 UTC – 0030 UTC on 30 May 2012 within the subdomain denoted in b). Panel b) is the same as Figure 38, with an inset black box denoting the 3 km × 3 km subdomain.

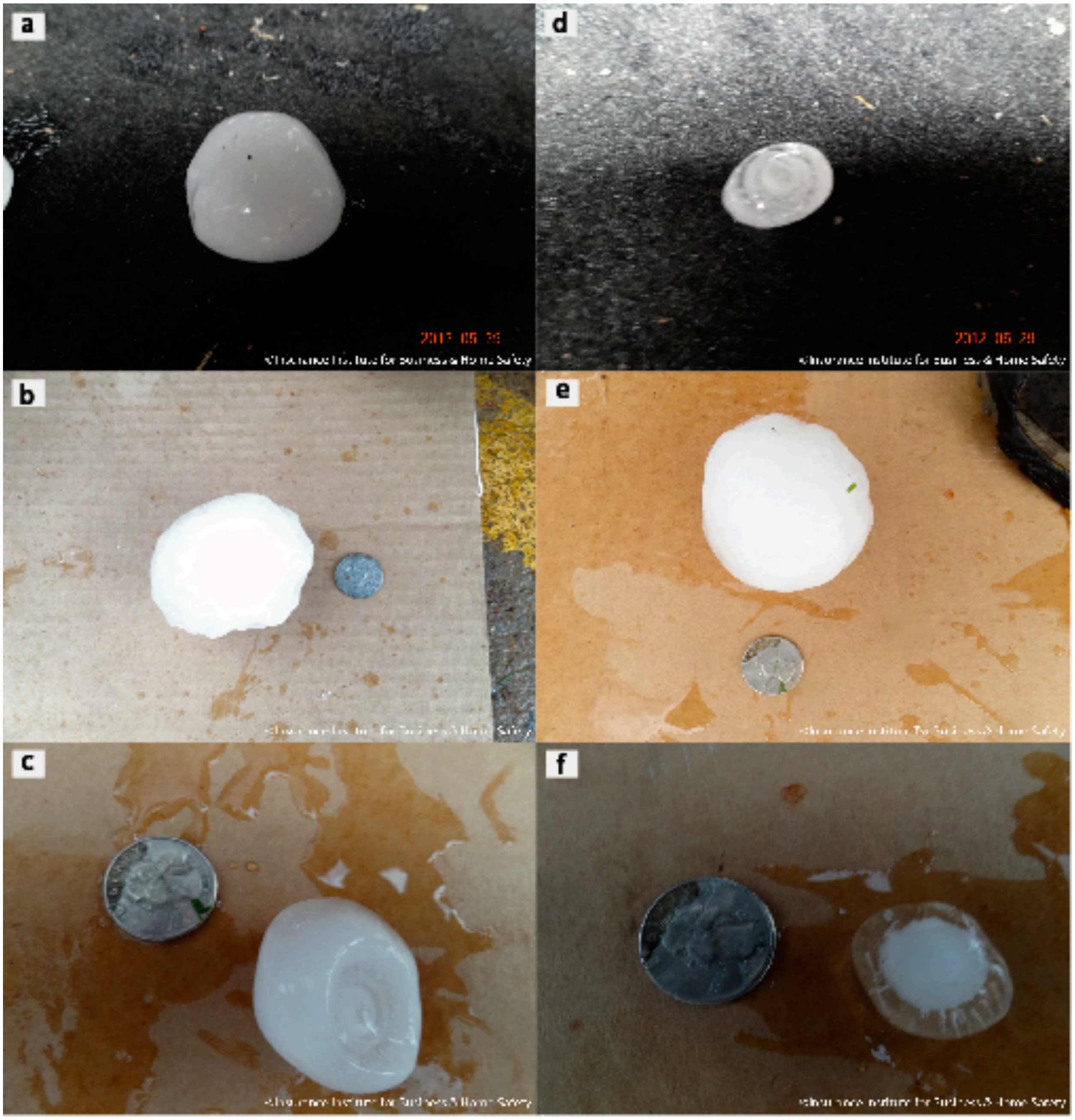


**Figure 43.** Sub-sample of hailstone observations collected by the Insurance Institute for Business and Home Safety (IBHS) ground teams in Kingfisher, OK on 29 May 2012. Hail photos and data courtesy of John Manobianco (IBHS).

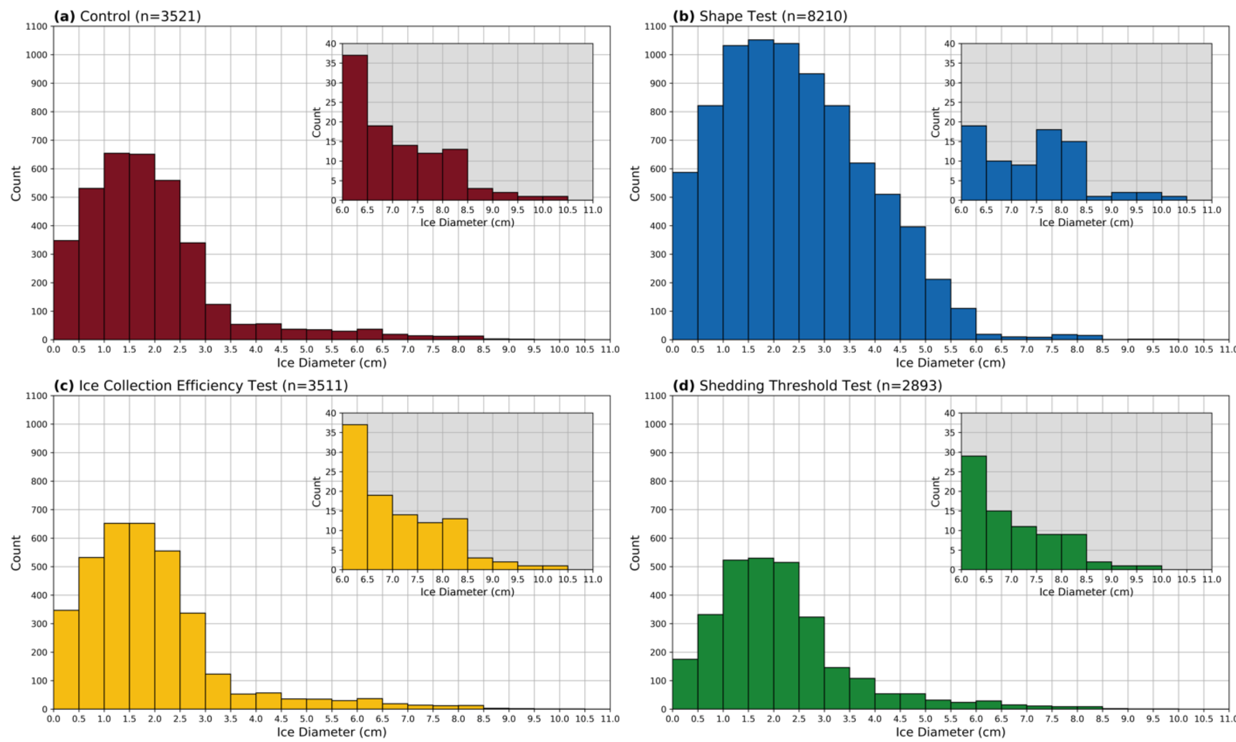


**Figure 44.** Histograms all hailstones initialized at 2339 UTC that made it to the surface from the a) control (red), b) shape test (blue), c) ice collection efficiency test (yellow), and d) shedding threshold test (green). The inset plots are zoomed in histograms of the upper tail (6 cm – 11 cm).

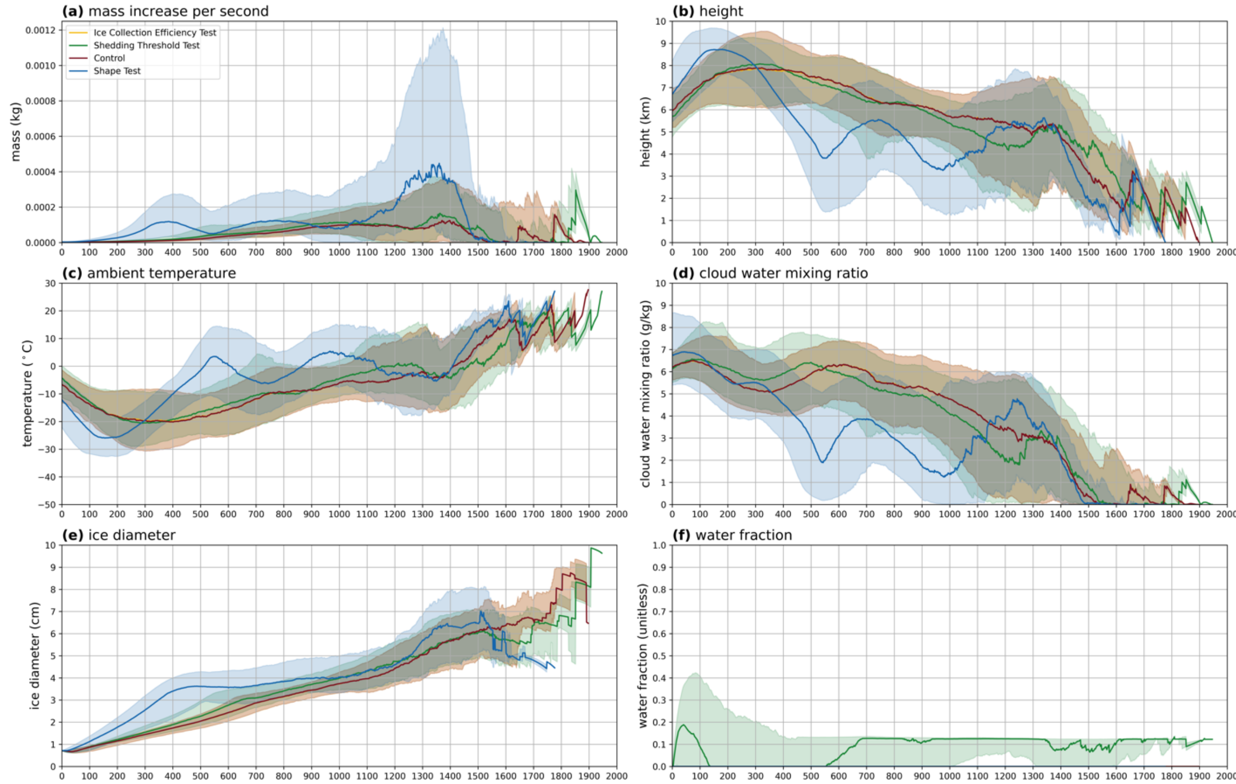


**Figure 45.** Environmental and hailstone characteristics time series of severe hailstones from 2339 UTC for all sensitivity tests including: control (red), ice collection efficiency test (yellow), shape test (blue), and shedding threshold test (green). The solid lines represent the mean of all severe hailstones in the cluster. The shaded region are the values between the 25$^{th}$ and 75$^{th}$ percentiles. Characteristics shown are: a) mass increase due to collection of supercooled water per second (kg), b) height (km), c) ambient temperature (°C) d) cloud water mixing ratio (g kg$^{-1}$), e) ice diameter (cm), and f) water fraction (unitless).

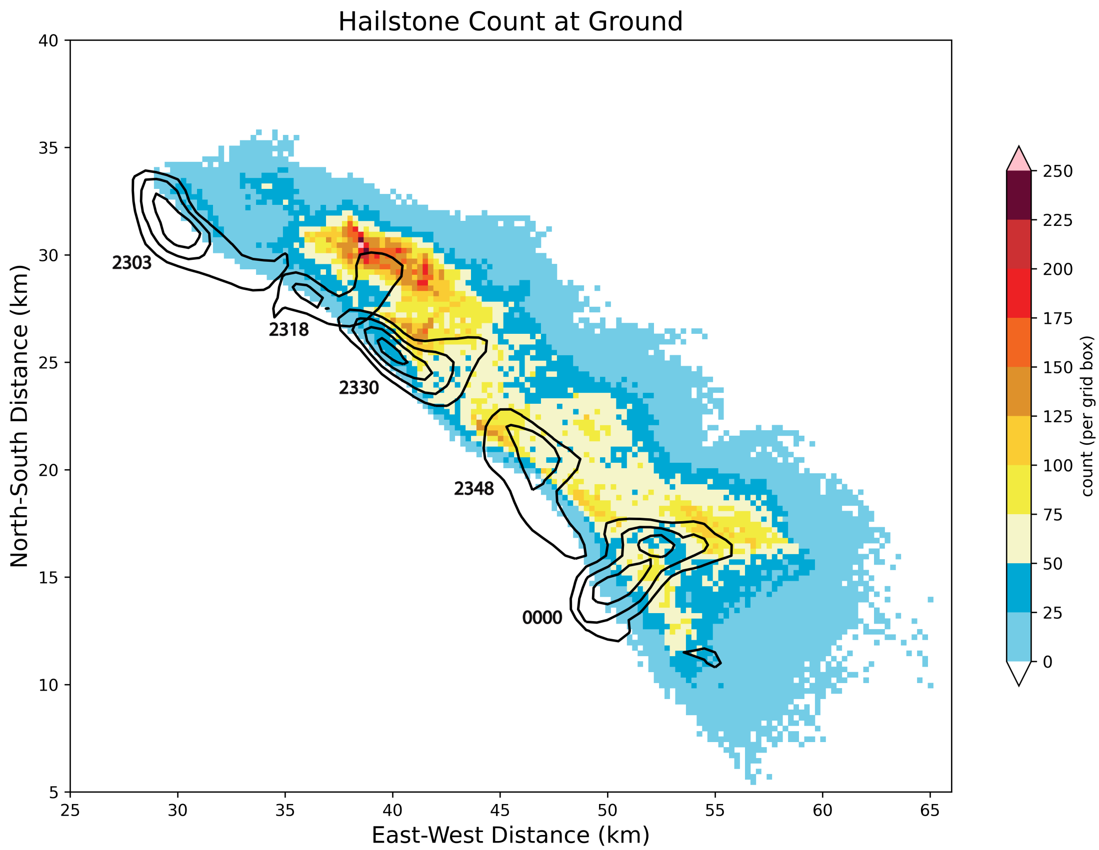


**Figure 46.** Same as Figure 37, but for oblate hailstones.

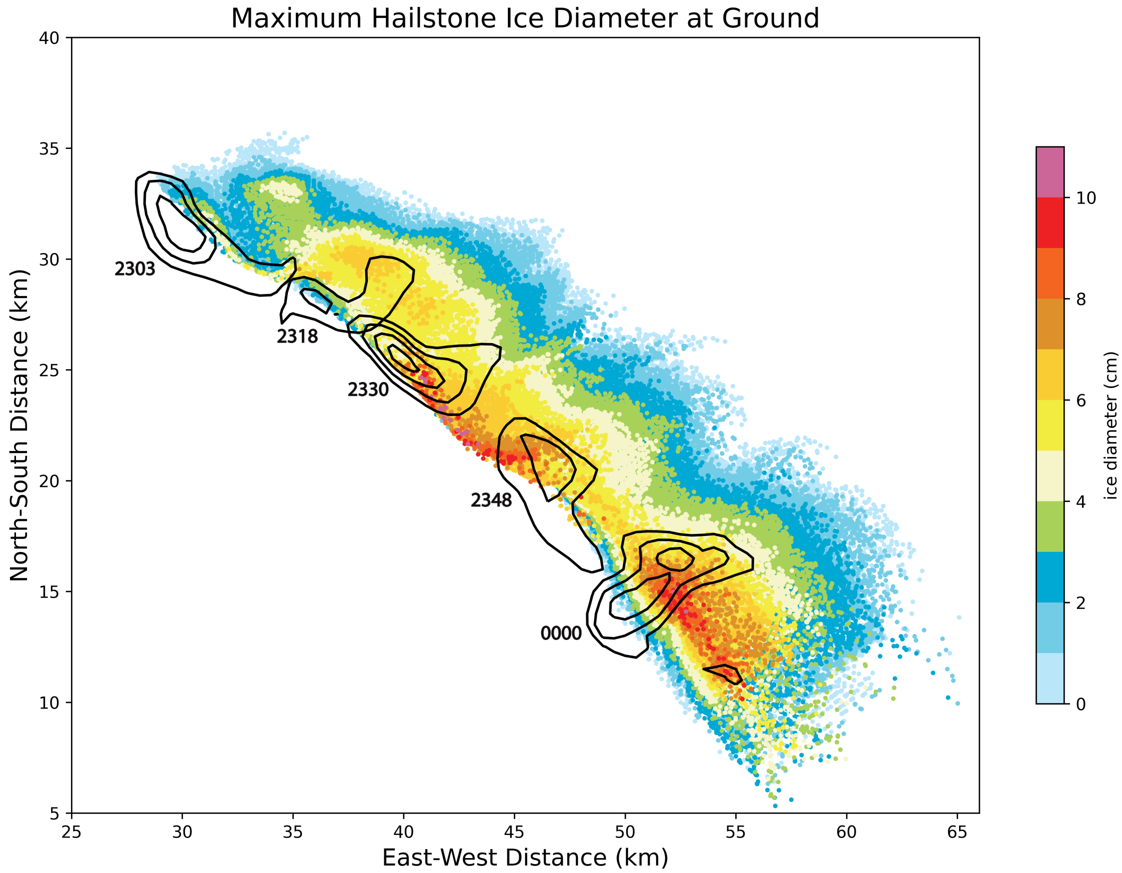


**Figure 47.** Same as Figure 38, but for oblate hailstones.

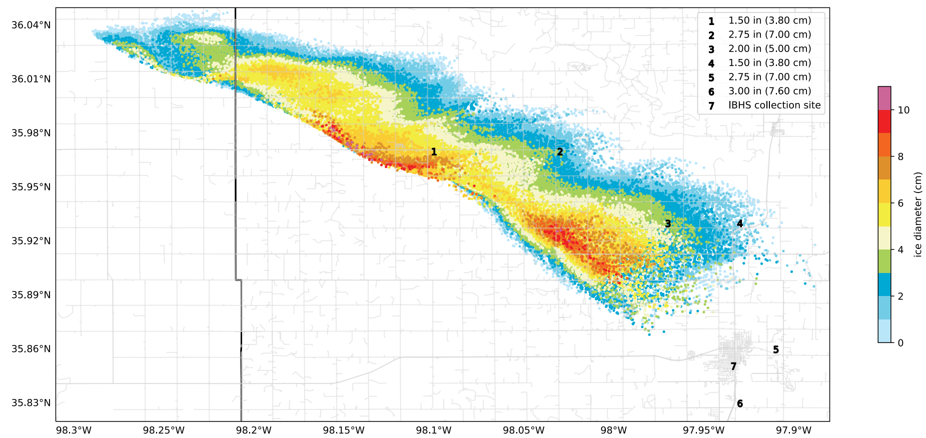


**Figure 48.** Same as Figure 39, but for oblate hailstones.

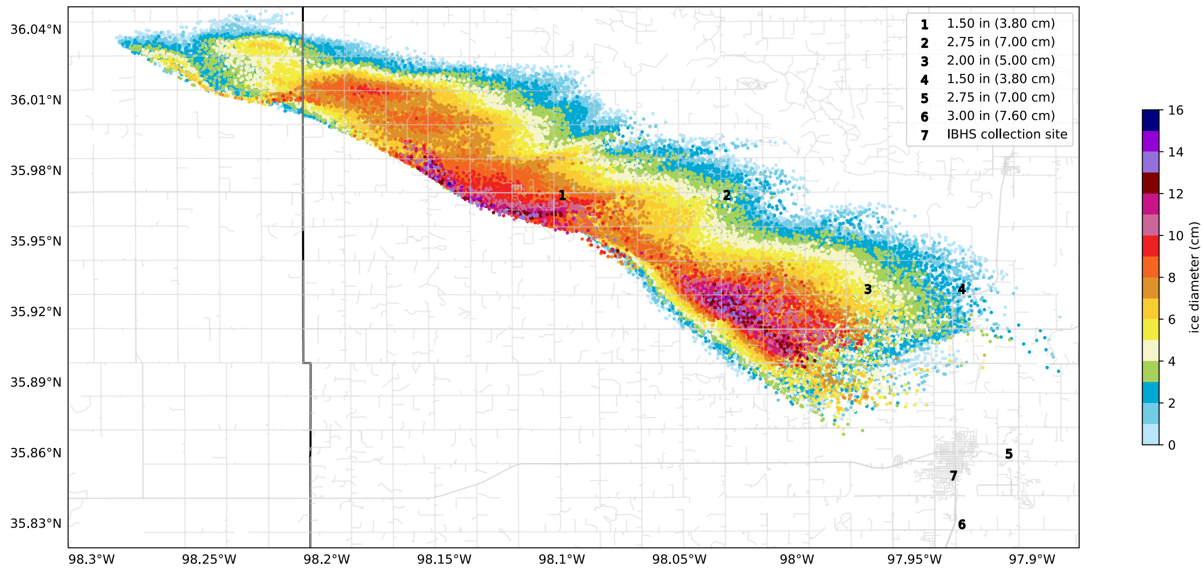


**Figure 49.** Same as Figure 48, but using $D_{max}$ rather than $D_{eq}$.

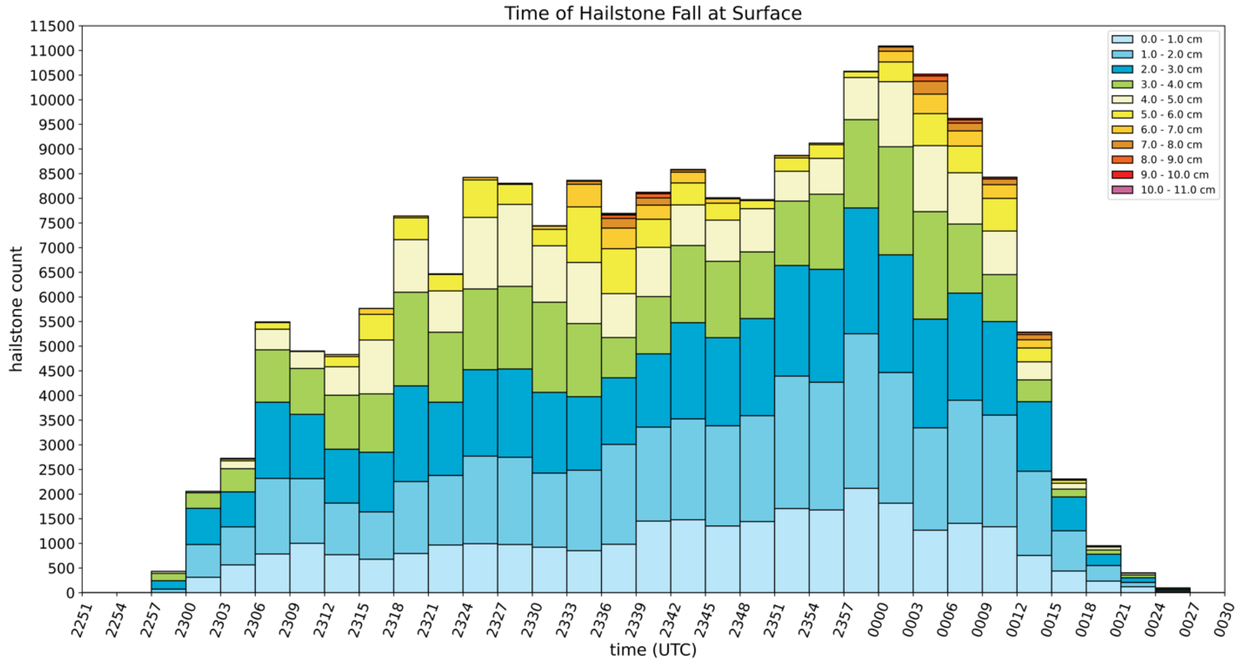


**Figure 50.** Same as Figure 40, but for oblate hailstones.

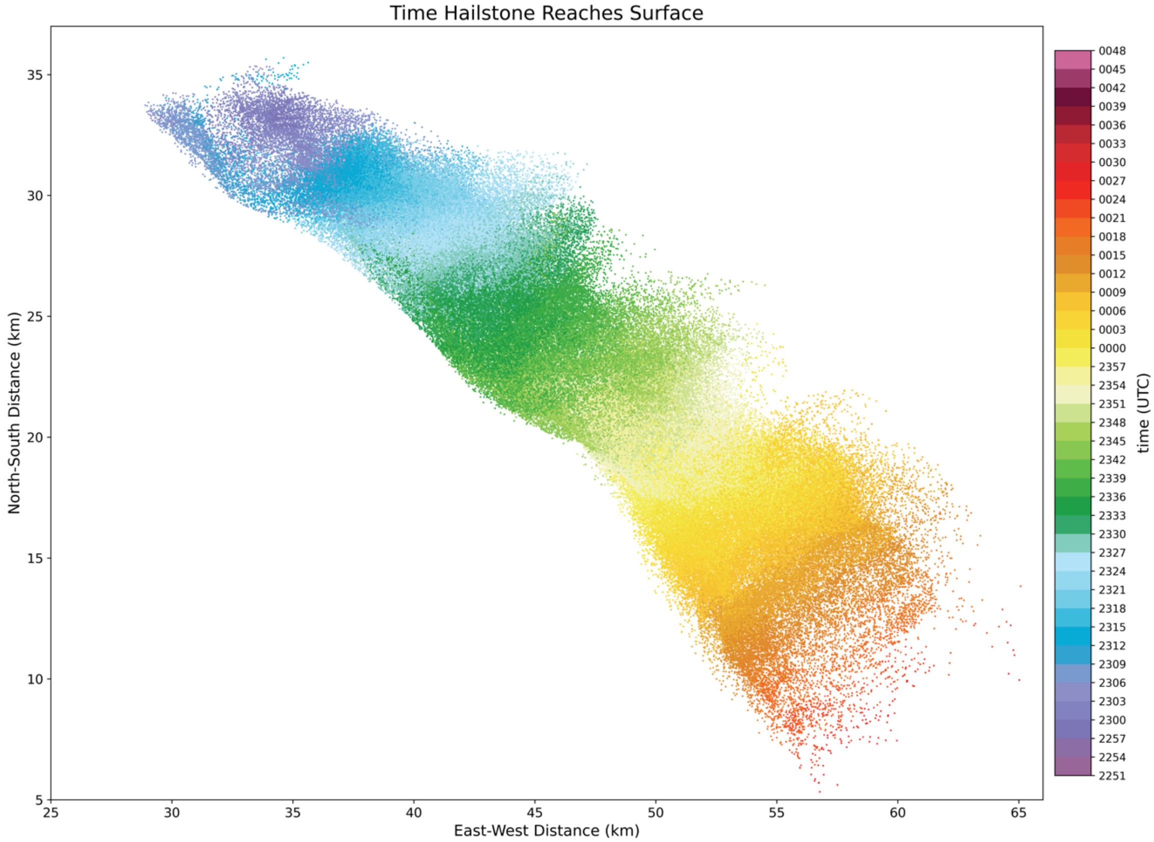


**Figure 51.** Same as Figure 41, but for oblate hailstones.